NASA Technical Paper 3579

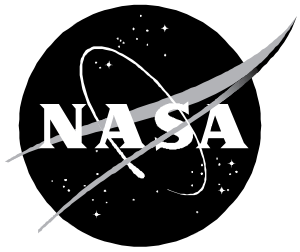

Assessment of Dual-Point Drag Reduction for an Executive-Jet Modified Airfoil Section

Dennis O. Allison and Raymond E. Mineck
Langley Research Center • Hampton, Virginia

National Aeronautics and Space Administration
Langley Research Center • Hampton, Virginia 23681-0001

July 1996

Available electronically at the following URL address: http://techreports.larc.nasa.gov/ltrs/ltrs.html

Printed copies available from the following:

NASA Center for AeroSpace Information
800 Elkridge Landing Road
Linthicum Heights, MD 21090-2934
(301) 621-0390

National Technical Information Service (NTIS)
5285 Port Royal Road
Springfield, VA 22161-2171
(703) 487-4650

Contents

Summary

This paper presents aerodynamic characteristics and pressure distributions for an executive-jet modified airfoil and discusses drag reduction relative to a baseline airfoil for two cruise design points. A modified airfoil was tested in the adaptive-wall test section of the NASA Langley 0.3-Meter Transonic Cryogenic Tunnel (0.3-m TCT) for Mach numbers from ranging 0.250 to 0.780 and chord Reynolds numbers ranging from 3.0×10^6 to 18.0×10^6. The angle of attack was varied from −2° to almost 10°. Boundary-layer transition was fixed at 5 percent of chord on both the upper and lower surfaces of the model for most of the test. The two design Mach numbers were 0.654 and 0.735, chord Reynolds numbers were 4.5×10^6 and 8.9×10^6, and normal-force coefficients were 0.98 and 0.51.

Test data are presented graphically as integrated force and moment coefficients and chordwise pressure distributions. The maximum normal-force coefficient decreases with increasing Mach number. At a constant normal-force coefficient in the linear region, as Mach number increases an increase occurs in the slope of normal-force coefficient versus angle of attack, negative pitching-moment coefficient, and drag coefficient. With increasing Reynolds number at a constant normal-force coefficient, the pitching-moment coefficient becomes more negative and the drag coefficient decreases. The pressure distributions reveal that when present, separation begins at the trailing edge as angle of attack is increased. The modified airfoil, which is designed with pitching moment and geometric constraints relative to the baseline airfoil, achieved drag reductions for both design points (12 and 22 counts). The drag reductions are associated with stronger suction pressures in the first 10 percent of the upper surface and weakened shock waves.

Introduction

The Langley Research Center was involved in a cooperative program with the Cessna Aircraft Company to design and test a modified airfoil for a proposed executive-jet configuration. The objective of this program was to improve aerodynamic performance at two design points by redesigning a baseline executive-jet airfoil using Langley-developed advanced computational fluid dynamics (CFD) design methods and experimental investigations. The Cessna Aircraft Company proposed two operating conditions for a business jet, one for long range cruise and the other for high speed cruise. The configuration was analyzed at both proposed cruise points, and the two-dimensional equivalent flow conditions were extracted at the mid-span location. The two design points consisted of the following combinations of Mach number, chord Reynolds number, and normal-force coefficient: 0.654, 4.5×10^6, and 0.98, respectively; and 0.735, 8.9×10^6, and 0.51, respectively.

Reference 1 presents wind tunnel aerodynamic characteristics and pressure distributions for the baseline airfoil. A dual-point design procedure (ref. 2) using the Constrained Direct Iterative Surface Curvature (CDISC) design method (ref. 3) is used in the redesign process. Geometric constraints were imposed to keep the following nearly constant: leading edge radius, maximum thickness ratio, and thickness ratio at 85 percent of chord. A redesigned airfoil (ref. 2) was produced that has a lower predicted wave drag for both design points, with a constraint of no increase in the negative pitching moment coefficient. The modified airfoil was developed from minor refinements of the redesigned airfoil that more accurately match the baseline airfoil maximum thickness and thickness at 85 percent of chord.

The two purposes of this paper are to present wind tunnel aerodynamic characteristics and pressure distributions for the modified airfoil over a wide range of flow conditions and to discuss drag reduction achieved for the baseline airfoil at the two design points. To compare baseline and modified airfoil data that are closely related to comparisons at a given flight condition, modified airfoil data were acquired with normal force coefficients matching those of the baseline airfoil. This match was achieved at the two design points and at two intermediate points where the flow conditions are between the design conditions. The test was conducted in the Langley 0.3-m TCT at Mach numbers ranging from 0.250 to 0.780 and chord Reynolds numbers ranging from 3.0×10^6 to 18.0×10^6. The angle of attack ranged from −2° to almost 10°. The upper limit on angle of attack was usually determined by model stall, and sometimes by physical limits on the displacement of the adaptive walls. Boundary-layer transition was fixed at 5 percent of chord on both the upper and lower surfaces of the airfoil model for most of the test. The 6-in-chord model spanned the width of the test section and was instrumented for chordwise pressure distribution measurements. A wake rake was used to measure pressure losses for drag determination.

Symbols

The measurements and calculations are made in the U.S. Customary Units. The symbols used in this report are defined as follows:

b model span (b = 13 in.)

C_p local pressure coefficient, $\dfrac{p - p_\infty}{q_\infty}$

C_p^* pressure coefficient for sonic condition

$C_{p,te}$ pressure coefficient at trailing edge

c model chord (c = 6 in.)

c_d section drag coefficient, measured on tunnel centerline, $\frac{\text{drag}}{q_\infty c}$

c_m section pitching-moment coefficient, resolved about $x = 0.25c$, $\frac{\text{pitching moment}}{q_\infty c^2}$

c_n section normal-force coefficient, $\frac{\text{normal force}}{q_\infty c}$

D diameter

M_∞ free-stream Mach number

p local static pressure, lbf/in^2

p_∞ free-stream static pressure, lbf/in^2

q_∞ free-stream dynamic pressure, $\frac{\rho_\infty V_\infty^2}{2}$, lbf/in^2

R_c free-stream Reynolds number based on model chord, $\frac{\rho_\infty V_\infty c}{\mu_\infty}$

t local thickness, in.

V_∞ free-stream velocity, in/sec

x chordwise position, measured aft from model leading edge, in.

y vertical position, measured up from model chord plane, in.

z spanwise position, measured to right from tunnel centerline, in.

α angle of attack, deg

η nondimensional spanwise position, $2z/b$

μ_∞ free-stream viscosity, slugs/in-sec

ρ_∞ free-stream density, slugs/in^3

Subscripts:

diff Mod minus Base

max maximum

Abbreviations:

Base baseline airfoil

Mod modified airfoil

Wind Tunnel

Testing was conducted in the 13- by 13-in. two-dimensional adaptive-wall test section of the Langley 0.3-m TCT. Figure 1 presents a sketch of the tunnel, and figure 2 presents a photograph of the upper leg of the tunnel circuit. The 0.3-m TCT is a fan-driven, cryogenic pressure tunnel that uses gaseous nitrogen as a test medium. It is capable of operating at stagnation temperatures from just above the boiling point of liquid nitrogen (approximately 144°R (80 K)) to 589°R (327 K) and at stagnation pressures from 1.2 to 6.0 atm. The fan speed is variable so that the empty test section Mach number can be varied continuously from about 0.20 to 0.95. This combination of test conditions provides a test envelope of chord Reynolds numbers up to about 50×10^6 based on a model chord of 6 in. Reference 4 gives additional details of the 0.3-m TCT.

Wind tunnels with adaptive walls attempt to eliminate the wall-induced interference at its source. This is accomplished by modifying the flow field near the test section boundaries so that the flow field in the vicinity of the model duplicates “free air” conditions. The adaptive walls are reset for each model and each test condition. Reference 5 gives specific details of the adaptive-wall method.

Test Section

Figure 3 presents sketches of the adaptive-wall test section with the plenum sidewall removed, and figures 4 and 5 present photographs of the test section flow region. The model mounting system is designed for two-dimensional models with chords up to 13 in. A model is supported between two turntables centered 30.7 in. downstream of the test section entrance. The turntables are driven by an electric stepper motor that is connected through a yoke to the perimeter of both turntables. This arrangement drives both turntables to eliminate possible model twisting. The angular position of the turntables, and therefore the geometric angle of attack of the model, is measured using a digital shaft encoder geared to the left turntable.

The test section is 13 in. by 13 in. at the entrance, and all four walls are solid. The sidewalls are rigid whereas the top and bottom walls are flexible and movable. The flexible walls are 71.7 in. long and are anchored at the upstream end. The rear 15.9-in. portion diverges 4.1° to form a transition between the test section and the high-speed diffuser. The test section is therefore considered to be 55.8 in. long. The shape of each wall is determined by 21 independent jacks. Table 1 presents the jack locations relative to the center of the model-mounting turntable. Each wall-positioning jack is driven by a stepper motor located outside the test section

plenum. The jacks have a design displacement range of 3 in. up and 1 in. down. However, the available displacement for each jack varies because of limits on allowable wall stress due to curvature. Pressure orifices are located on the top and bottom wall centerlines at the jack positions and 1.0 in. upstream of the wall anchor point. The jack at −1.75 in. (upstream of the turntable) on the bottom wall was inoperative during this test. Because the connection between this jack and the flexible wall was removed, the wall displacement could not be determined at this station. The wall was free to "float" to a position determined by the jack just upstream and the jack just downstream of the inoperative jack.

Wake Rake

A horizontal rake supported by a vertical traversing mechanism is used to survey the wake pressure field. The vertical traversing mechanism moves the rake within the limits of 3 in. below to 5 in. above the centerline. The traversing mechanism is driven by a stepper motor mounted externally to the tunnel, and the number of steps used to traverse the wake in this test is 50. The vertical position of the traversing mechanism is measured by a digital shaft encoder geared to the stepper motor. The rake has three static and six total pressure probes (tubes), as shown in figure 6. This arrangement allows the total pressure variation in the model wake to be determined at six spanwise locations. The wake rake can be installed at one of three streamwise stations: the forward, center, and rear stations, which are located at 12.5, 17.5, and 22.5 in., respectively, downstream of the center of the turntable. (See fig. 3(b).) Based on previous test experience, the wake rake should be at least 1 chord downstream of the model trailing edge to avoid aerodynamic interference with the model. For this test, the wake rake is located at the center station (fig. 7), which is 2.17 model chords downstream of the model trailing edge.

Model

The model used in this test was supported by mounting blocks (fig. 8) and the blocks were bolted to the turntables. The model chord was aligned with the center of the turntable for $\alpha = 0°$ and α was changed by rotation about $x = 0.513c$. The model had a 6-in. chord, a 13-in. span, and a modified airfoil section with a maximum thickness of $0.115c$ at $x = 0.37c$. The leading-edge radius was $0.017c$. Tables 2 and 3 present the design and measured model coordinates, respectively, for the modified airfoil. The maximum difference between the measured profile and the design profile is $0.0004c$. Figure 9 presents a sketch of the airfoil section showing pressure orifice locations.

The model was equipped with 47 pressure orifices: 21 on the lower surface in a chordwise row at the spanwise center and 26 on the upper surface in an offset chordwise row. For ease of fabrication, the upper surface row of orifices was offset 0.5 in. to the right from the spanwise center and the upper and lower surface orifices in the nose region (for $x < 0.2$ in.) were staggered to within ±0.10 in. in the spanwise direction from their respective rows. Table 4 lists the orifice locations, which are shown in the airfoil sketch in figure 9. All the orifices were 0.010 in. in diameter.

Test Instrumentation

Reference 6 provides a detailed discussion of the instrumentation and procedures for the calibration and control of the 0.3-m TCT. For two-dimensional airfoil tests, the 0.3-m TCT is equipped to obtain static pressure measurements on the airfoil model surface, total and static pressure measurements in the model wake, and static pressure measurements on the test section sidewalls, top wall, and bottom wall. The following sections describe instrumentation for tunnel flow conditions, airfoil model pressures, wall pressures, and wake pressures.

Test Condition

Three primary measurements determine the tunnel test condition: total pressure, static pressure, and total temperature. The total pressure and static pressure are measured by individual quartz differential pressure transducers referenced to a vacuum to function as absolute pressure devices. Each transducer has a range of ±100 psid and an accuracy of ±0.006 psid plus ±0.012 percent of the pressure reading. The stagnation temperature is measured by a platinum resistance thermometer. Individual digital voltmeters are used to convert analog output from each of these devices to digital form for display and recording.

Airfoil Model Pressures

The pressures on the airfoil model are measured by individual transducers connected by tubing to each orifice on the model. The transducers are a high-precision variable-capacitance type. The maximum range of these differential transducers is ±100 psid with an accuracy of ±0.25 percent of the reading from −25 psid to 100 psid. They are located outside the high-pressure cryogenic environment of the tunnel, but as close as possible to the test section to minimize the tubing length and reduce the response time. To provide increased accuracy, the transducers are mounted on thermostatically controlled heater bases to maintain a constant temperature and on "shock" mounts to reduce possible vibration effects. The electrical signals from the transducers are processed by

individual signal conditioners located in the tunnel control room. The signal conditioners are autoranging and have seven ranges available. As a result of the autoranging capability, the analog output to the data acquisition system is kept at a high level even though the pressure transducer may be operating at the low end of its range.

Wall and Wake Pressures

The top and bottom flexible-wall pressures are measured using a pressure scanning system operating two 48-port valves. Because of the large changes in the pressure of the tunnel over its operational range, the same type of variable-capacitance pressure transducers and autoranging signal conditioners described previously are used with the pressure scanning system instead of the more typical strain gauge transducer.

The total pressure loss in the model wake is measured with the rake described previously. The pressure in each of the six total pressure tubes is measured with the same type of variable-capacitance pressure transducer described previously but with a maximum range of ±20 psi. The static pressure in the model wake is the average of measured pressures on the right sidewall at eight vertical positions at the tunnel station of the wake rake (which is on the left sidewall). The static pressure probes on the rake were not used because they have not provided reliable data in the past.

Procedures

Test conditions were chosen to cover a wide range of Mach numbers and Reynolds numbers that encompass the two design points ($M_\infty = 0.654$, $R_C = 4.5 \times 10^6$, $c_n = 0.98$; and $M_\infty = 0.735$, $R_c = 8.9 \times 10^6$, $c_n = 0.51$). Table 5 shows the combinations of M_∞ and R_c (written herein as M_∞–R_c) in the test program, and dashed underlines indicate the combinations for the two design points. Figure numbers are listed in table 5 for each M_∞–R_c combination in the program as an aid to locating pressure data for given test conditions. (The Mach numbers in the text, in table 5, and in the figure titles are nominal values, whereas the Mach numbers in the figure keys are slightly different because they are measured values.)

Most of the test was conducted with transition strips placed at the 5-percent-chord location on both surfaces of the model to match the boundary-layer transition locations that were used in the airfoil design calculations. (See ref. 2.) The grit size of 0.0016 in. was determined (ref. 7) for a Reynolds number of $R_c = 4.5 \times 10^6$. (For $R_c = 9.0 \times 10^6$, where the appropriate size would be 0.0010 in., the boundary-layer thickness is expected to exceed the chosen size of 0.0016 in.) The glass compound transition grit used for this test consisted of class 5 close-sized unispheres of 0.0016 in. nominal diameter, and the strips were approximately 1/16 in. wide. The transition strips were removed near the end of the test and some free-transition data were taken.

The following procedure was used to set each test condition. The tunnel total pressure, total temperature, and fan speed were set for the desired Mach number and Reynolds number, and the model turntable was adjusted to the desired angle of attack. When the test condition became stable, the wall-adaptation process in reference 5 was initiated, and after completion, the flexible-wall position and static pressures associated with the adapted walls were recorded on the data tape. Twenty samples of the airfoil static pressures, the test conditions, the wake rake total pressures, and the wake static pressures were then recorded during a 1-sec interval. Each sample consisted of simultaneous static pressure readings from all orifices on the model. The wake rake was moved to the next vertical location and another 20 samples of wake data were recorded. Wake data were obtained at 50 vertical locations of the model wake rake. The adapted walls were held fixed as the wake rake was moved.

Data Reduction

Because the tunnel operating envelope includes high pressures and low temperatures, real-gas effects are included in the data reduction for the tunnel test conditions by using the thermodynamic properties of nitrogen gas calculated from the Beattie-Bridgeman equation of state. Reference 8 shows that this equation gives essentially the same thermodynamic properties and flow calculation results given by the more complicated Jacobsen equation of state for the temperature-pressure realm of the 0.3-m TCT. References 9 and 10 give detailed discussions of real-gas effects when testing in cryogenic nitrogen.

Most wind tunnels have rigid test section walls, and wall interference corrections can be made to bring data close to data for free air flow. The present twofold approach to wall interference brings the data for each test condition closer to data for free air flow. First, wall interference is physically minimized for each test condition by appropriate movement of the adaptive walls. (See ref. 5.) Since a finite number of wall jacks are used and the test section has a finite length, some residual wall interference is expected. Second, the data is corrected for any residual top and bottom wall interference by the method in reference 11. Thus, the data is as close as possible to data for free air flow by using available tunnel hardware, wall adaptation software, and wall correction software. The same twofold approach was used for the baseline airfoil data. (See ref. 1.)

Integrated Coefficients

Section normal-force and pitching-moment coefficients were calculated using integration of measured surface pressures. A polynomial curve fit (ref. 12) of the measured pressure coefficients was used to enrich the distribution of points by a factor of 10, followed by the trapezoidal method of integration.

The section drag coefficient was calculated from the wake survey pressures (ref. 13) by first computing an incremental or point drag coefficient for each rake tube total pressure at each rake location. These point drag coefficients were then numerically integrated across the model wake in the vertical direction using the trapezoidal method. The results of this integration are total section drag coefficients at each of the six spanwise locations of the wake rake total pressure tubes. All drag data presented in this report are for the total pressure tube on the tunnel centerline.

Two-Dimensional Flow

The pressure data for each of the six total pressure tubes were examined to ensure that the wake survey covered the entire vertical extent of the wake and to determine when two-dimensional flow was not present across the model. The data from the tube that was 1 in. from the sidewall (fig. 6) were not consistent with the data from the other five total pressure tubes probably because this tube is immersed in the combined sidewall boundary layer and model wake. Therefore, this tube was not included in the final data reduction. An examination of the spanwise distributions of section drag coefficient showed that as the normal-force coefficient increased above a certain level, the section drag coefficient began to vary across the span, an indication that two-dimensional flow was beginning to break down. This c_n level decreased with increasing Mach number. Figure 10 illustrates typical spanwise variations of section drag coefficient. The flow was considered two-dimensional when the section drag coefficient was within ±10 percent of the section drag coefficient at the centerline of the tunnel. This criterion was met for the centerline and two adjacent total pressure tubes (at least one-third of the model span) for normal-force coefficients up to 0.1 below the maximum normal-force coefficient for all runs. Caution should be exercised when using data in which the normal-force coefficient is close to the maximum (within 0.1 of $c_{n,\max}$) for a given Mach number, especially for $M_\infty > 0.700$.

Presentation of Data

The data from this test are presented graphically and were taken with fixed transition except where noted. Figures 11 and 12 present data repeatability. Figures 13 and 14 present the effects of M_∞ and R_c on integrated force and moment coefficients. Figures 15–24 present the effect of R_c and α on chordwise pressure distributions at all 26 flow conditions. Finally, figures 25 and 26 present the limited amount of data available for free transition.

Data Repeatability

Data repeatability for the wind tunnel test was examined by repeating an angle-of-attack variation at a given subsonic condition and by repeating one angle of attack at a given transonic condition several times during the test. An angle-of-attack variation at $M_\infty = 0.500$ and $R_c = 4.5 \times 10^6$, measured on the first day of the test (run A in fig. 11), was repeated (run B in fig. 11) on the third day. For those two runs, force and moment data were compared (figs. 11(a) and 11(b)) and pressure distributions for angles of attack of 0° and 5° were compared (fig. 11(c)). Subsequently during the test, a case at $\alpha = 4°$ from an early transonic run (run A in fig. 12) was repeated four times (runs B, C, D, and E in fig. 12). Force and moment data were compared (figs. 12(a) and 12(b)), and pressure distributions were compared from the earliest and latest runs (runs A and E in fig. 12(c)).

Some small differences were evident in the repeated data. An angle-of-attack disagreement of about 0.1° occurred in figure 11(a) at $c_n = 0.01$ and in figure 12(a) for $c_n = 0.91$ (see the diamond symbol for run C). This uncertainty may relate to some play in the mechanism that measures the angle of attack. Repeatability of c_m is very good (fig. 11(a) and fig. 12(a)). Repeatability of c_d, based on data fairing curves, is approximately 0.0002 for the subsonic condition (fig. 11(b)) and 0.0003 for the transonic condition (fig. 12(b)). The pressure distribution comparison for $\alpha = 4°$ in figure 12(c) shows a small shift in the upper surface C_p level between $x/c = 0.1$ and 0.3, which is explained by a small difference in c_n between the two data points. The data from run B in figure 11 and from run A in figure 12 are included in the following data without the designation of run A or run B.

Force and Moment Coefficients

Figure 13 presents the effect of free-stream Mach number on integrated force and moment coefficients for the modified airfoil for the following Reynolds numbers: 3.0×10^6, 4.5×10^6, 6.5×10^6, 9.0×10^6, and 13.5×10^6. For the data at constant Reynolds number, the general trends with increasing Mach number are described as follows: the maximum normal-force coefficient decreases; and for a constant c_n in the linear c_n–α range, the c_n–α slope increases, the pitching moment becomes more negative, and the drag coefficient increases. There is a drag coefficient trend reversal for $R_c = 4.5 \times 10^6$ between $M_\infty = 0.670$ and $M_\infty = 0.700$ at $c_n = 0.6$. (See fig. 13(d).)

The reason for the trend reversal appears to be elevated wave drag at $M_\infty = 0.655$ and $M_\infty = 0.670$ caused by the influence of the upper surface transition grit strip at $x/c = 0.05$ on the shock wave just downstream of the strip. Compare the $\alpha = 2.0°$ ($M_\infty = 0.655$, $R_c = 4.5 \times 10^6$) pressure distribution for fixed transition in figure 19(b) with that for free transition in figure 26(a). There is a stronger upper surface expansion between $x/c = 0.04$ and $x/c = 0.08$ followed by a stronger shock wave for fixed transition than for free transition. A similar expansion at the grit strip location just ahead of a shock wave is present for $M_\infty = 0.670$, $R_c = 4.5 \times 10^6$ in figure 20(a).

Figure 14 presents the effect of free-stream Reynolds number at a constant Mach number on integrated force and moment coefficients for Mach numbers of 0.250, 0.500, 0.600, 0.655, 0.670, 0.700, 0.735, and 0.760. The normal-force coefficient increases with Reynolds number at a given α, which is expected, because the aft camber in the airfoil can be effectively reduced by the boundary layer. As Reynolds number increases, the boundary layer becomes thinner and less effective at reducing aft camber. The negative pitching moment becomes more negative with increasing Reynolds numbers, which is also expected, because a thinner boundary layer is less effective at decambering over the rear part of the airfoil.

For low drag levels ($c_d < 0.012$), drag coefficient at a constant c_n decreases with increasing Reynolds number for Mach numbers up to 0.735. (See, for example, fig. 14(h) and fig. 14(n).) This trend is expected because skin-friction drag decreases as Reynolds number increases. This general trend is not seen at $M_\infty = 0.760$. (See fig. 14(p).) This can be explained by looking at the effects of Reynolds number on chordwise pressure distributions which are presented at $c_n \approx 0$, 0.2, and 0.4 in figure 15 for $M_\infty = 0.760$. (Note that the level of the sonic pressure coefficient, C_p^*, is indicated.) As Reynolds number is increased, increases in wave drag can overcome decreases in friction drag. At $c_n \approx 0$, the drag coefficient does not decrease as Reynolds number increases (fig. 14(p)) because the lower surface shock waves become stronger. (See fig. 15(a).) However, for $c_n \approx 0.2$, the drag coefficient decreases as R_c increases (fig. 14(p)) because the shock waves are weak and there is a smaller difference in wave drag between the Reynolds number cases. (See fig. 15(b).) At $c_n \approx 0.4$, the drag coefficient increases as Reynolds number increases (fig. 14(p)) because the upper surface shock wave (and associated suction pressure in the rearward-facing region) becomes stronger. (See fig. 15(c).)

Chordwise Pressure Distributions

Figures 16–24 present the effect of angle of attack on chordwise pressure distributions for the program of M_∞–R_c test conditions in table 5. In figures 17–24 the level of the sonic pressure coefficient (C_p^*) is included as an aid to understanding which areas on the model have local supersonic or near-supersonic flow. The C_p scale increment per grid division is changed from –0.4 to –0.2 for figures 22–24 to more clearly display the features of the pressure distributions at high Mach numbers.

The plotted pressure distributions for each M_∞–R_c combination include a representative set of four or five angles of attack which is sufficient for covering the available range of data and illustrating the onset of separation (when present). The following comments concerning boundary-layer separation apply to figures 17–24. (See, for example, fig. 17(a).) Trailing-edge separation is indicated by the trailing-edge pressure coefficient becoming more negative at the highest angles of attack. Leading-edge separation is not indicated as the upper surface suction peak near the leading edge remains intact at the highest angles of attack. The data in figures 18–24 (see, for example, fig. 18(a)) show that as angle of attack increases, the upper surface shock wave reaches a maximum rearward location, and then moves forward as trailing-edge separation begins. This trend generally becomes more pronounced for higher M_∞ and higher R_c. The shock wave location and trailing-edge pressure coefficient are probably interrelated by a separation bubble created by shock-wave boundary-layer interaction.

Free Transition

Free-transition data were obtained at the end of the test at the following five combinations of M_∞–R_c: 0.655 and 4.5×10^6; 0.735 and 4.5×10^6; 0.700 and 6.5×10^6; 0.655 and 9.0×10^6; 0.735 and 9.0×10^6. Figure 25 presents the effect of free transition on force and moment coefficients and figure 26 presents the effect of angle of attack on pressure distributions with free transition. Free transition is associated with a longer run of laminar flow on the upper and/or lower surface, which delays transition to a turbulent boundary layer. This delay results in a thinner turbulent boundary layer with less effective decambering of the rear of the airfoil and more rear loading. The extra rear loading caused generally increased c_n and more negative c_m in the linear c_n–α range. (See fig. 25.) The generally decreased c_d in the linear c_n–α range results from the extended laminar boundary layer, which has lower drag than the turbulent boundary layer that it replaces.

Dual-Point Drag Reduction

The purpose of this section is to discuss dual-point drag reduction of the modified airfoil relative to the baseline airfoil. Figure 27 compares the baseline and modified airfoils. The leading-edge radii are nearly identical at 0.017c for the modified airfoil and 0.016c for the baseline airfoil. Both airfoils have a thickness of 0.028c at $x = 0.85c$ and a maximum thickness of 0.115c. The maximum thickness location is farther aft at $x = 0.37c$ for the modified airfoil compared with $x = 0.31c$ for the baseline airfoil. The upper surface is slightly flatter, the lower forward region is undercut, and the lower aft concavity is more pronounced for the modified airfoil. Baseline airfoil coordinates (table 6) and data (figs. 28–31) are taken from reference 1.

Figures 28–31 compare force and pressure data at the design and two intermediate points for the baseline and modified airfoils. To compare pressure distributions, modified-airfoil data were taken for each of the design and intermediate points at additional angles of attack in an attempt to match the baseline normal-force coefficient (for example, $c_n = 0.939$ in fig. 28). The comparisons in part (c) of each figure are matched for normal-force coefficient and the maximum $c_{n,\mathrm{diff}}$ is 0.004. The pitching-moment design constraint (ref. 2) resulted in little difference in the pitching-moment coefficients between the baseline and modified airfoils in part (c) of each figure. Table 7 summarizes flow conditions, drag coefficients, and drag coefficient reductions.

Pressure distribution comparisons at a given flow condition can be used to make judgements concerning amounts of pressure drag, wave drag, and friction drag for the modified airfoil relative to the baseline airfoil (figs. 28(c)–31(c)). The drag coefficient for the modified airfoil was lower than that for the baseline airfoil at all four points.

Three factors are associated with the drag reduction at each point. First, the higher suction pressures in the first 10 percent of the upper surface indicate less pressure drag because that part of the surface has a forward slope. Second, the lower suction pressure (lower local Mach number) just ahead of the shock wave indicates that the modified airfoil should have less wave drag. Third, the weaker shock wave probably results in a thinner boundary layer with less friction drag. The progression from figure 28(c) to figure 31(c) indicates less benefit in the first 10 percent of chord on the upper surface, and more benefit associated with a weaker shock wave. The shock wave is shifted forward by about 3–6 percent of chord for figures 28(c)–30(c) but does not shift forward in figure 31(c). The largest drag reduction occurs in figure 31(c), which appears to have the greatest reduction in the strength of the shock wave.

Boundary-layer separation from the trailing edge can have a significant influence on pressure drag, wave drag, and friction drag. Trailing-edge pressure coefficients provide an indication of the onset of this type of separation as angle of attack is increased. For the first design point, figure 28(d) is a plot of trailing-edge pressure coefficient as a function of angle of attack for both airfoils. Each $C_{p,te}$ curve has a relatively low-gradient region at lower angles of attack. At higher angles of attack, each curve has a significantly stronger gradient (toward increasingly negative pressure coefficients). The onset of trailing-edge separation is indicated by the beginning of the stronger gradient. Separation from the trailing edge does not appear to occur for the baseline or modified airfoil at $\alpha = 4.1°$. For the baseline airfoil, trailing-edge separation begins above $\alpha = 4.1°$ where the slope begins to increase. (See fig. 28(d).) The onset of separation for the modified airfoil occurs at about a 1°-higher angle of attack ($\alpha \approx 5°$) than for the baseline airfoil ($\alpha = 4.1°$). The same conclusions were drawn for both intermediate points and the other design point (figs. 29(d)–31(d)).

Concluding Remarks

A wind tunnel test of a modified executive-jet airfoil model was conducted in the two-dimensional adaptive-wall test section of the Langley 0.3-Meter Transonic Cryogenic Tunnel to measure aerodynamic characteristics for a wide range of flow conditions. For increasing Mach number, the maximum normal-force coefficient decreased. With increasing Mach number at a constant normal-force coefficient in the linear range of normal-force coefficient (c_n) versus angle of attack (α), increases occurred in the c_n–α slope, the negative pitching-moment coefficient, and the drag coefficient. With increasing Reynolds number at a constant normal-force coefficient, the negative pitching-moment coefficient became more negative and the drag coefficient decreased. The pressure distributions revealed that separation began at the trailing edge. The modified airfoil was designed with pitching moment and geometric constraints for lower wave drag at two design points. The dual-point design conditions were established to achieve long-range cruise and high-speed cruise. The modified airfoil drag coefficients were 5 to 22 counts lower than for the baseline airfoil, with little difference in pitching moment coefficients for the two design points and two intermediate points. Drag reductions were associated with weaker shock waves and with higher suction levels on the forward part of the upper surface. Trailing-edge

separation did not appear to occur for either airfoil at the design or intermediate points.

NASA Langley Research Center
Hampton, VA 23681-0001
March 7, 1996

References

1. Allison, Dennis O.; and Mineck, Raymond E.: *Aerodynamic Characteristics and Pressure Distributions for an Executive-Jet Baseline Airfoil Section.* NASA TM-4529, 1993.

2. Mineck, Raymond E.; Campbell, Richard L.; and Allison, Dennis O.: *Application of Two Procedures for Dual-Point Design of Transonic Airfoils*. NASA TP-3466, 1994.

3. Campbell, Richard L.: *An Approach to Constrained Aerodynamic Design With Application to Airfoils.* NASA TP-3260, 1992.

4. Ray, E. J.; Ladson, C. L.; Adcock, J. B.; Lawing, P. L.; and Hall, R. M.: *Review of Design and Operational Characteristics of the 0.3-Meter Transonic Cryogenic Tunnel*. NASA TM-80123, 1979.

5. Judd, M.; Wolf, S. W. D.; and Goodyer, M. J.: *Analytical Work in Support of the Design and Operation of Two Dimensional Self Streamlining Test Sections*. NASA CR-145019, 1976.

6. Ladson, Charles L.; and Kilgore, Robert A.: *Instrumentation for Calibration and Control of a Continuous-Flow Cryogenic Tunnel.* NASA TM-81825, 1980.

7. Braslow, Albert L.; and Knox, Eugene C.: *Simplified Method for Determination of Critical Height of Distributed Roughness Particles for Boundary-Layer Transition at Mach Numbers From 0 to 5*. NACA TN 4363, 1958.

8. Hall, Robert M.; and Adcock, Jerry B.: *Simulation of Ideal-Gas Flow by Nitrogen and Other Selected Gases at Cryogenic Temperatures*. NASA TP-1901, 1981.

9. Adcock, Jerry B.: *Real-Gas Effects Associated With One-Dimensional Transonic Flow of Cryogenic Nitrogen*. NASA TN D-8274, 1976.

10. Adcock, Jerry B.; and Johnson, Charles B.: *A Theoretical Analysis of Simulated Transonic Boundary Layers in Cryogenic-Nitrogen Wind Tunnels*. NASA TP-1631, 1980.

11. Murthy, A. V.: *Residual Interference Assessment in Adaptive Wall Wind Tunnels.* NASA CR-181896, 1989.

12. Akima, H.: A New Method of Interpolation and Smooth Curve Fitting Based on Local Procedures. *J. Assn. Comput. Mach.*, vol. 17, Oct. 1970, pp. 589–602.

13. Baals, Donald D.; and Mourhess, Mary J.: *Numerical Evaluation of the Wake-Survey Equations for Subsonic Flow Including the Effect of Energy Addition*. NACA WR L-5, 1945.

Table 1. Locations of Jacks for Flexible-Wall Positioning

[Jack station locations are referenced to center of turntable]

Jack	Location, in.	Notes
	–31.25	Pressure orifice near test section entrance
	–30.25	Anchor point
1	–26.00	First test section jack
2	–20.25	
3	–15.25	
4	–11.25	
5	–8.25	
6	–6.25	
7	–4.75	
8	–3.25	
9	–1.75	Lower wall jack at this station not operational
10	–.25	
11	1.25	
12	2.75	
13	4.75	
14	6.75	
15	8.75	
16	11.75	
17	15.75	
18	20.75	Last test section jack
19	25.75	Start of transition section
20	30.75	
21	36.75	

Table 2. Design Coordinates for Modified Airfoil

Upper surface		Lower surface		Upper surface		Lower surface	
x/*c*	*y*/*c*	*x*/*c*	*y*/*c*	*x*/*c*	*y*/*c*	*x*/*c*	*y*/*c*
0.00000	0.00000	0.00000	0.00000	0.44557	0.06434	0.44557	–0.04819
.00099	.00620	.00099	–.00602	.46597	.06391	.46597	–.04692
.00301	.01045	.00301	–.00987	.48646	.06330	.48646	–.04541
.00604	.01431	.00604	–.01314	.50699	.06248	.50699	–.04369
.01005	.01788	.01005	–.01595	.52756	.06143	.52756	–.04178
.01500	.02122	.01500	–.01833	.54812	.06014	.54812	–.03971
.02088	.02438	.02088	–.02033	.56865	.05862	.56865	–.03749
.02764	.02740	.02764	–.02203	.58912	.05686	.58912	–.03514
.03528	.03030	.03528	–.02351	.60950	.05489	.60950	–.03268
.04374	.03308	.04374	–.02485	.62977	.05274	.62977	–.03014
.05302	.03570	.05302	–.02609	.64990	.05043	.64990	–.02754
.06308	.03816	.06308	–.02730	.66986	.04803	.66986	–.02491
.07389	.04048	.07389	–.02853	.68962	.04555	.68962	–.02231
.08543	.04269	.08543	–.02980	.70915	.04304	.70915	–.01976
.09766	.04481	.09766	–.03113	.72843	.04050	.72843	–.01730
.11056	.04685	.11056	–.03253	.74742	.03794	.74742	–.01498
.12411	.04881	.12411	–.03400	.76611	.03538	.76611	–.01284
.13826	.05068	.13826	–.03553	.78445	.03283	.78445	–.01090
.15300	.05247	.15300	–.03713	.80243	.03029	.80243	–.00919
.16830	.05420	.16830	–.03878	.82002	.02775	.82002	–.00773
.18413	.05585	.18413	–.04047	.83718	.02521	.83718	–.00650
.20045	.05743	.20045	–.04215	.85389	.02269	.85389	–.00551
.21725	.05891	.21725	–.04376	.87013	.02019	.87013	–.00475
.23450	.06025	.23450	–.04526	.88585	.01775	.88585	–.00420
.25216	.06143	.25216	–.04662	.90105	.01539	.90105	–.00384
.27021	.06244	.27021	–.04780	.91568	.01312	.91568	–.00365
.28863	.06326	.28863	–.04880	.92972	.01096	.92972	–.00360
.30737	.06390	.30737	–.04960	.94314	.00890	.94314	–.00367
.32642	.06436	.32642	–.05018	.95592	.00694	.95592	–.00383
.34575	.06466	.34575	–.05052	.96802	.00507	.96802	–.00405
.36533	.06481	.36533	–.05060	.97942	.00329	.97942	–.00432
.38513	.06485	.38513	–.05042	.99009	.00160	.99009	–.00460
.40512	.06478	.40512	–.04995	1.00000	.00000	1.00000	–.00489
.42527	.06462	.42527	–.04920				

Table 3. Measured Coordinates for Modified Airfoil

Upper surface		Lower surface		Upper surface		Lower surface	
x/*c*	*y*/*c*	*x*/*c*	*y*/*c*	*x*/*c*	*y*/*c*	*x*/*c*	*y*/*c*
0.00000	–0.00003	0.00000	–0.00003	0.44563	0.06451	0.44559	–0.04795
.00095	.00607	.00106	–.00582	.46604	.06406	.46598	–.04668
.00297	.01044	.00325	–.00976	.48654	.06344	.48652	–.04518
.00603	.01429	.00620	–.01290	.50703	.06262	.50704	–.04347
.00983	.01780	.01000	–.01560	.52761	.06157	.52759	–.04156
.01474	.02120	.01490	–.01796	.54816	.06028	.54814	–.03949
.02070	.02445	.02085	–.01992	.56871	.05873	.56875	–.03726
.02740	.02745	.02753	–.02163	.58919	.05697	.58910	–.03493
.03517	.03042	.03520	–.02319	.60960	.05498	.60953	–.03247
.04353	.03320	.04361	–.02458	.62981	.05283	.62979	–.02992
.05272	.03580	.05289	–.02586	.64996	.05051	.64990	–.02732
.06296	.03831	.06291	–.02709	.66996	.04810	.66983	–.02473
.07365	.04062	.07374	–.02831	.68971	.04562	.68963	–.02213
.08521	.04286	.08525	–.02956	.70919	.04311	.70917	–.01956
.09741	.04498	.09747	–.03088	.72849	.04055	.72847	–.01710
.11037	.04705	.11041	–.03228	.74746	.03798	.74743	–.01480
.12384	.04901	.12394	–.03375	.76617	.03539	.76609	–.01264
.13806	.05090	.13811	–.03529	.78451	.03284	.78448	–.01069
.15279	.05271	.15282	–.03688	.80244	.03030	.80247	–.00901
.16810	.05444	.16814	–.03853	.82011	.02774	.82007	–.00757
.18387	.05607	.18397	–.04020	.83723	.02521	.83723	–.00636
.20025	.05764	.20033	–.04187	.85395	.02267	.85397	–.00538
.21707	.05911	.21712	–.04347	.87026	.02015	.87017	–.00462
.23435	.06044	.23433	–.04495	.88588	.01771	.88591	–.00407
.25197	.06162	.25204	–.04631	.90107	.01533	.90112	–.00371
.27001	.06262	.27005	–.04749	.91569	.01305	.91578	–.00355
.28846	.06344	.28843	–.04848	.92978	.01087	.92971	–.00352
.30718	.06406	.30719	–.04929	.94318	.00880	.94303	–.00363
.32626	.06452	.32624	–.04989	.95591	.00684	.95582	–.00383
.34555	.06482	.34560	–.05027	.96809	.00496	.96792	–.00409
.36527	.06499	.36539	–.05036	.97941	.00318	.97933	–.00443
.38518	.06504	.38519	–.05016	.99015	.00141	.98996	–.00471
.40520	.06497	.40519	–.04970	1.00000	–.00039	1.00000	–.00462
.42532	.06480	.42530	–.04896				

Table 4. Orifice Locations for Modified Airfoil

Upper surface		Lower surface	
x/*c*	*y*/*c*	*x*/*c*	*y*/*c*
0.00000	0.00000	0.00487	–0.01167
.00517	.01333	.00965	–.01540
.02008	.02415	.01950	–.01953
.02997	.02848	.04942	–.02540
.03998	.03207	.07948	–.02893
.08010	.04190	.11968	–.03328
.09962	.04535	.17958	–.03975
.15018	.05240	.23965	–.04538
.20020	.05763	.29978	–.04900
.25017	.06150	.35965	–.05037
.30000	.06383	.41965	–.04918
.34037	.06475	.47997	–.04568
.42037	.06485	.54020	–.04030
.46010	.06422	.60015	–.03360
.50032	.06290	.64987	–.02732
.54023	.06080	.71990	–.01817
.58023	.05777	.76970	–.01223
.62022	.05387	.83970	–.00620
.66028	.04928	.89985	–.00373
.69992	.04430	.94995	–.00373
.75040	.03757	1.00000	–.00245
.80023	.03062		
.85045	.02320		
.90047	.01542		
.94987	.00777		
1.00000	–.00245		

Table 5. Program of Test Conditions

[Dashed underlines indicate M_∞–R_c combinations for two design points]

R_c	Figures for pressure distributions at values of M_∞ of—								
	0.250	0.500	0.600	0.655	0.670	0.700	0.735	0.760	0.780
3.0×10^6				19(a)		21(a)			
4.5	16(a)	17(a)	18(a)	19(b)	20(a)	21(b)	22(a)	23(a)	
5.0					20(b)				
6.5				19(c)		21(c)	22(b)	23(b)	
9.0	16(b)	17(b)	18(b)	19(d)		21(d)	22(c)	23(c)	24
13.5						21(e)	22(d)		
18.0						21(f)			

Table 6. Design Coordinates for Baseline Airfoil

Upper surface		Lower surface		Upper surface		Lower surface	
x/*c*	*y*/*c*	*x*/*c*	*y*/*c*	*x*/*c*	*y*/*c*	*x*/*c*	*y*/*c*
0.00000	0.00000	0.00000	0.00000	0.44557	0.06691	0.44557	–0.04100
.00099	.00635	.00099	–.00489	.46597	.06601	.46597	–.03958
.00301	.01117	.00301	–.00821	.48646	.06488	.48646	–.03808
.00604	.01562	.00604	–.01132	.50699	.06353	.50699	–.03651
.01005	.01974	.01005	–.01431	.52756	.06197	.52756	–.03487
.01500	.02362	.01500	–.01702	.54812	.06020	.54812	–.03317
.02088	.02731	.02088	–.01949	.56865	.05826	.56865	–.03141
.02764	.03076	.02764	–.02183	.58912	.05617	.58912	–.02961
.03528	.03395	.03528	–.02407	.60950	.05397	.60950	–.02777
.04374	.03692	.04374	–.02622	.62977	.05168	.62977	–.02591
.05302	.03969	.05302	–.02830	.64990	.04933	.64990	–.02403
.06308	.04230	.06308	–.03035	.66986	.04692	.66986	–.02214
.07389	.04477	.07389	–.03234	.68962	.04448	.68962	–.02027
.08543	.04713	.08543	–.03428	.70915	.04200	.70915	–.01842
.09766	.04937	.09766	–.03617	.72843	.03948	.72843	–.01662
.11056	.05152	.11056	–.03797	.74742	.03694	.74742	–.01489
.12411	.05358	.12411	–.03968	.76611	.03438	.76611	–.01324
.13826	.05554	.13826	–.04126	.78445	.03181	.78445	–.01170
.15300	.05740	.15300	–.04270	.80243	.02922	.80243	–.01028
.16830	.05915	.16830	–.04400	.82002	.02665	.82002	–.00897
.18413	.06078	.18413	–.04512	.83718	.02409	.83718	–.00781
.20045	.06228	.20045	–.04605	.85389	.02157	.85389	–.00678
.21725	.06364	.21725	–.04680	.87013	.01910	.87013	–.00591
.23450	.06484	.23450	–.04735	.88585	.01670	.88585	–.00520
.25216	.06587	.25216	–.04769	.90105	.01438	.90105	–.00463
.27021	.06674	.27021	–.04783	.91568	.01217	.91568	–.00423
.28863	.06743	.28863	–.04777	.92972	.01006	.92972	–.00397
.30737	.06796	.30737	–.04751	.94314	.00807	.94314	–.00385
.32642	.06831	.32642	–.04705	.95592	.00621	.95592	–.00386
.34575	.06851	.34575	–.04642	.96802	.00447	.96802	–.00398
.36533	.06854	.36533	–.04561	.97942	.00285	.97942	–.00421
.38513	.06840	.38513	–.04465	.99009	.00136	.99009	–.00453
.40512	.06809	.40512	–.04355	1.00000	.00000	1.00000	–.00490
.42527	.06760	.42527	–.04233				

Table 7. Drag Coefficient Reductions at Design and Intermediate Points

Figure	Point	M_∞	R_c	α_{Base}	$c_{n,Base}$	$c_{d,Base}$	$c_{d,Mod}$	$c_{d,diff}$
28(c)	Design	0.655	4.5×10^6	4.1°	0.939	0.0204	0.0192	–0.0012
29(c)	Intermediate	0.670	5.0×10^6	3.2°	0.787	0.0128	0.0118	–0.0010
30(c)	Intermediate	0.700	6.5×10^6	2.1°	0.694	0.0108	0.0103	–0.0005
31(c)	Design	0.735	9.0×10^6	1.0°	0.565	0.0120	0.0098	–0.0022

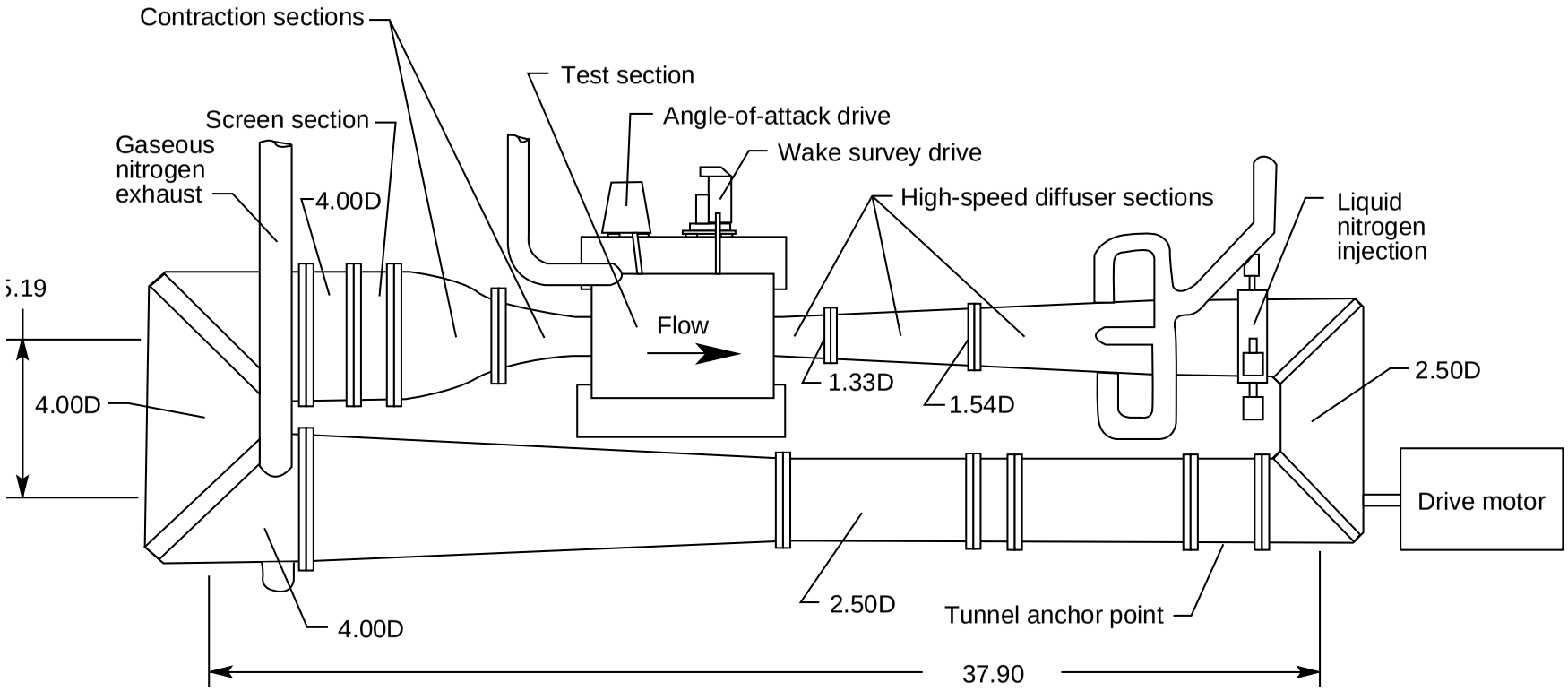

Figure 1. Sketch of Langley 0.3-Meter Transonic Cryogenic Tunnel with 13- by 13-in. adaptive wall test section. All dimensions given in feet. Diameters are for tunnel interior.

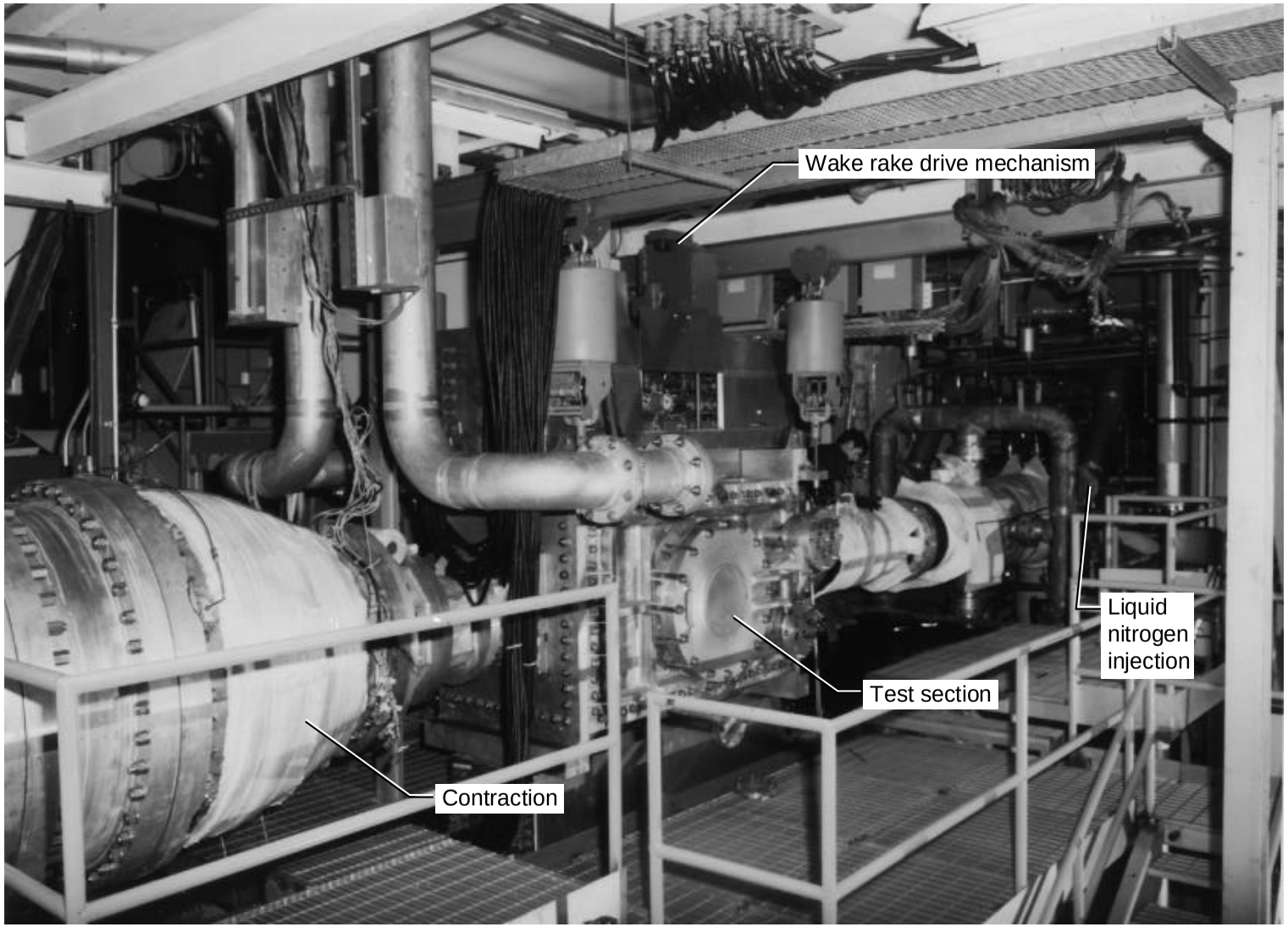

L-85-9893

Figure 2. Photograph of upper leg of Langley 0.3-Meter Transonic Cryogenic Tunnel with 13- by 13-in. adaptive wall test section.

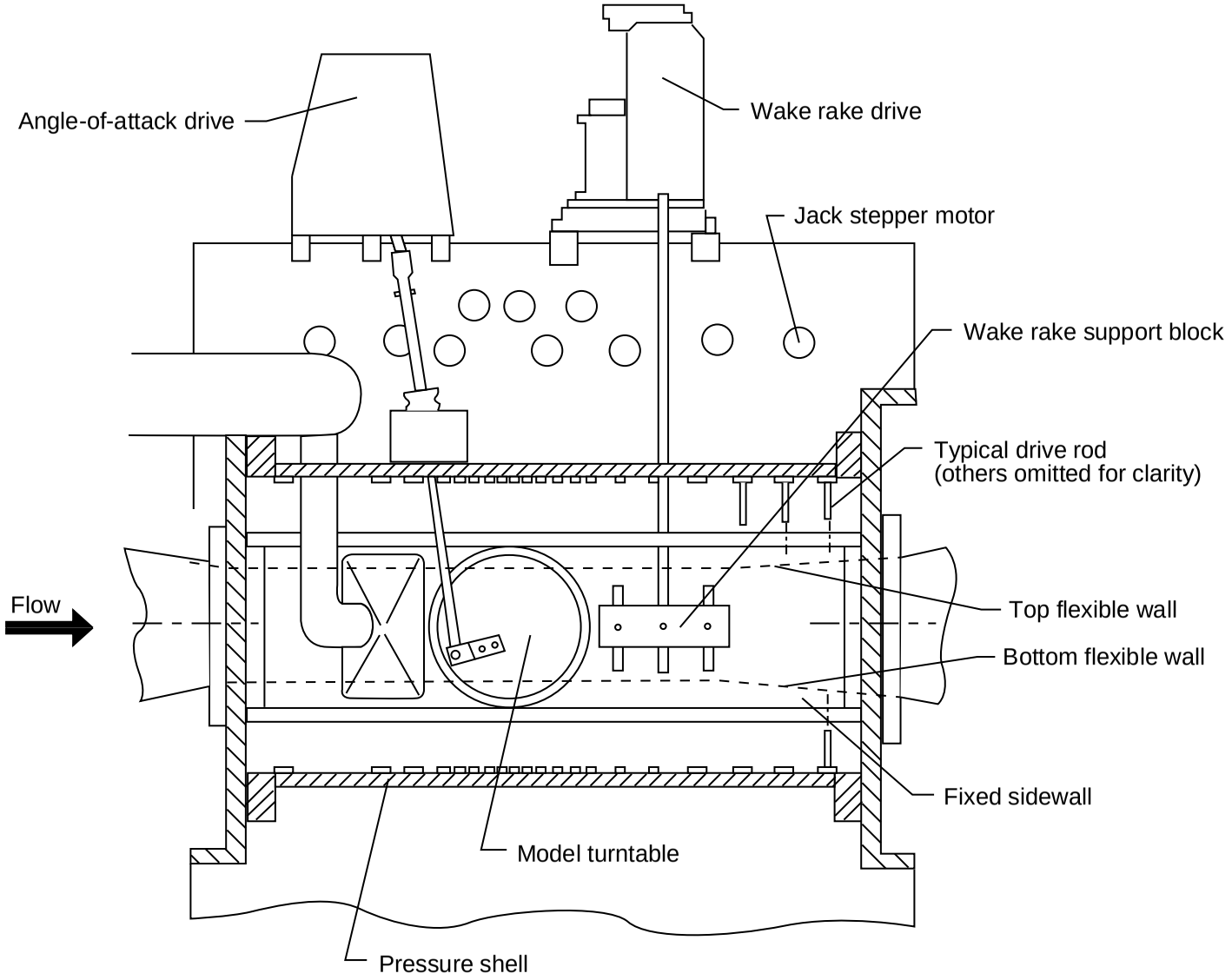

(a) Plenum sidewall removed.

Figure 3. Sketches of 13- by 13-in. adaptive wall test section.

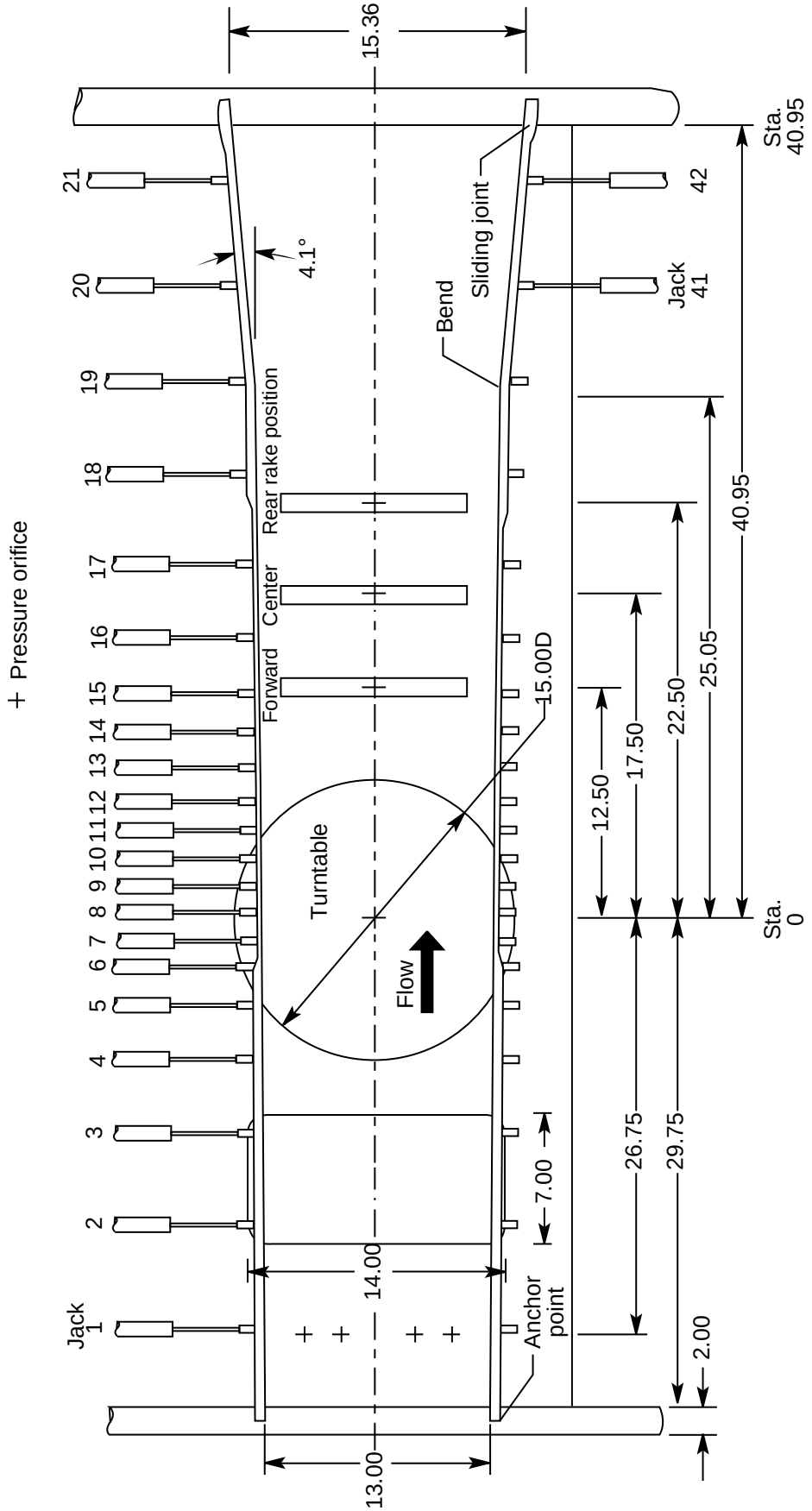

(b) Details of flow region. All dimensions given in inches. Some lower wall jacks omitted for clarity.

Figure 3. Concluded.

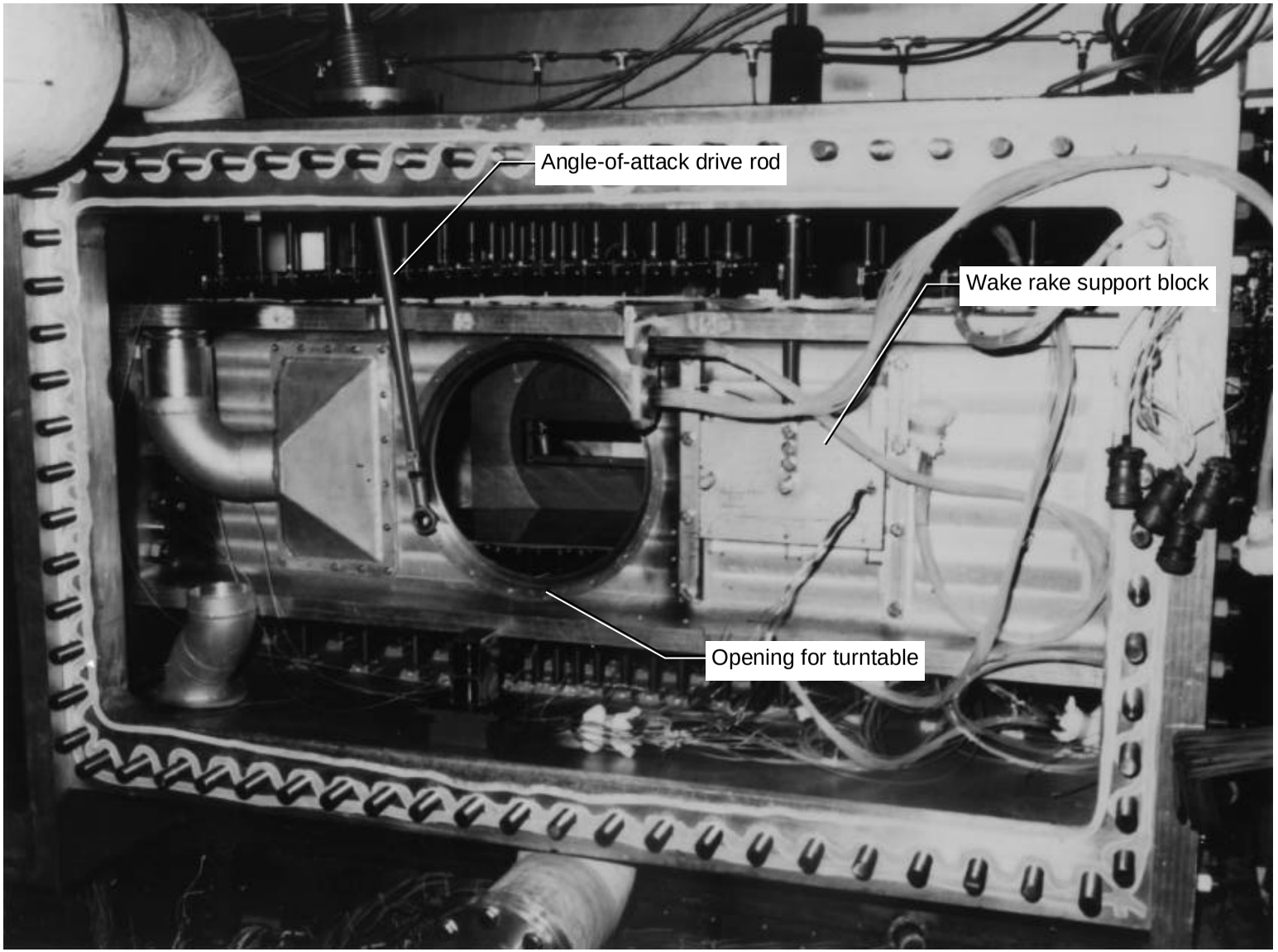

L-87-8385

Figure 4. Photograph of adaptive wall test section with plenum sidewall removed.

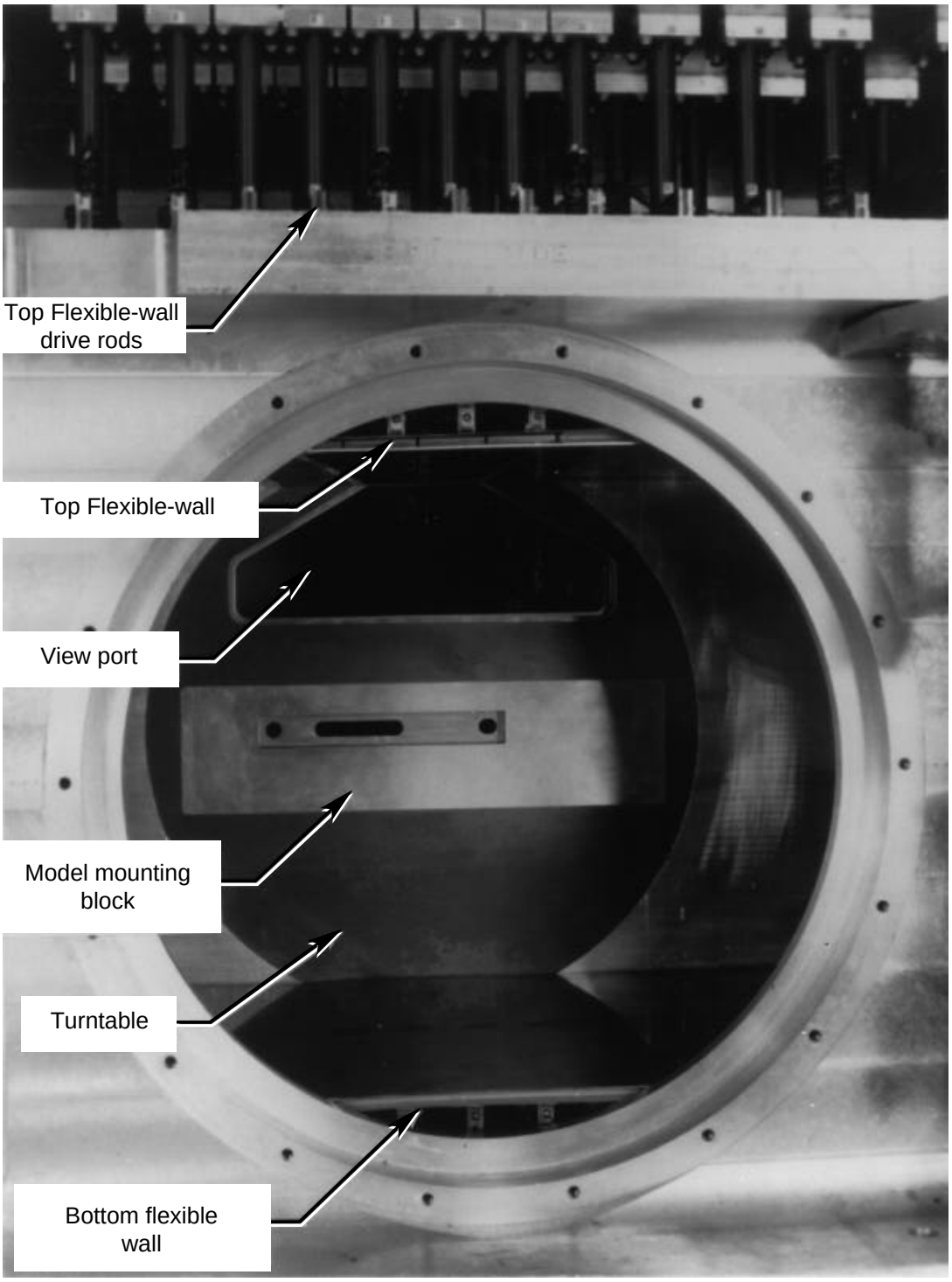

L-87-659

Figure 5. Photograph of region where model installed.

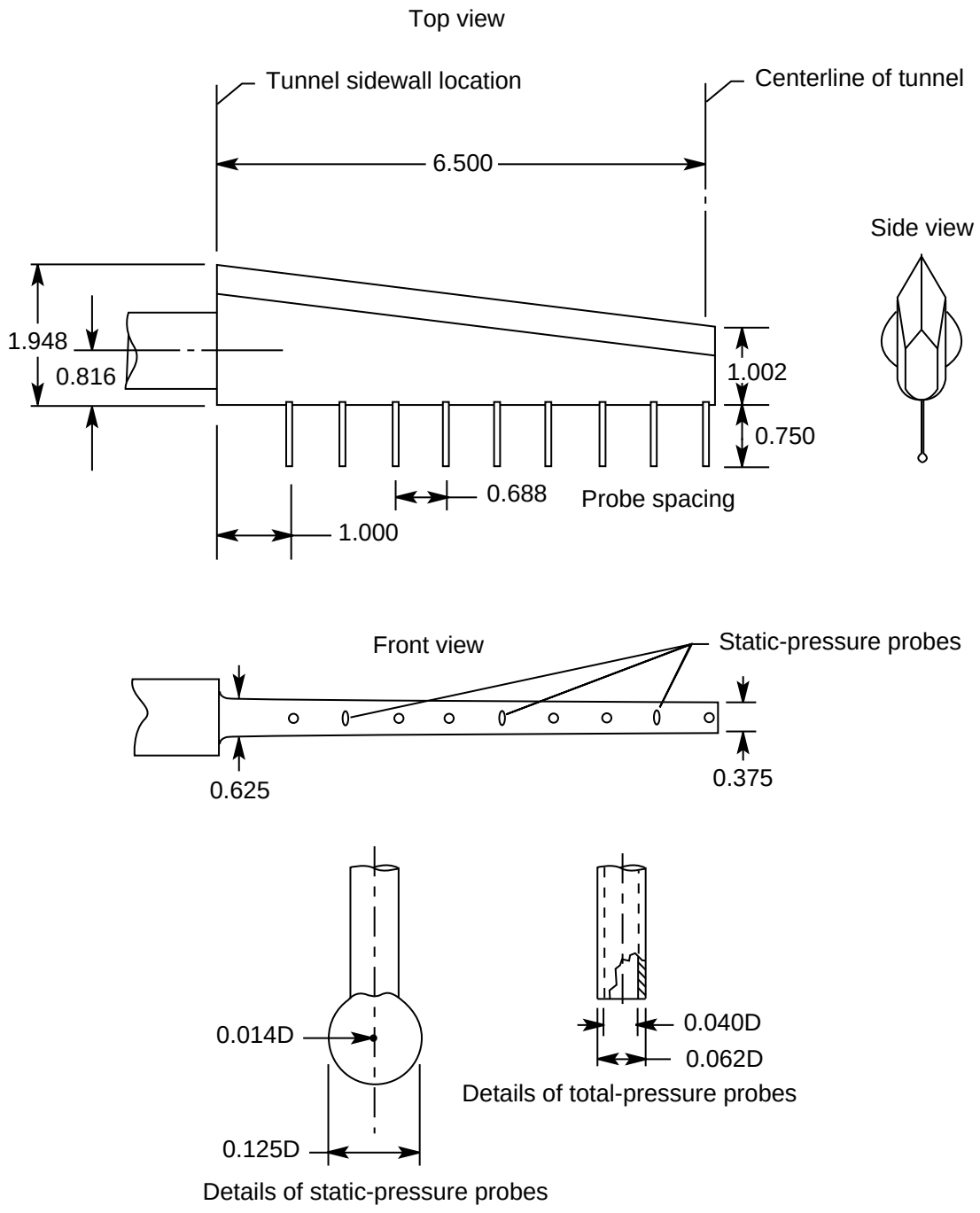

Figure 6. Sketch of wake survey probe. All dimensions given in inches.

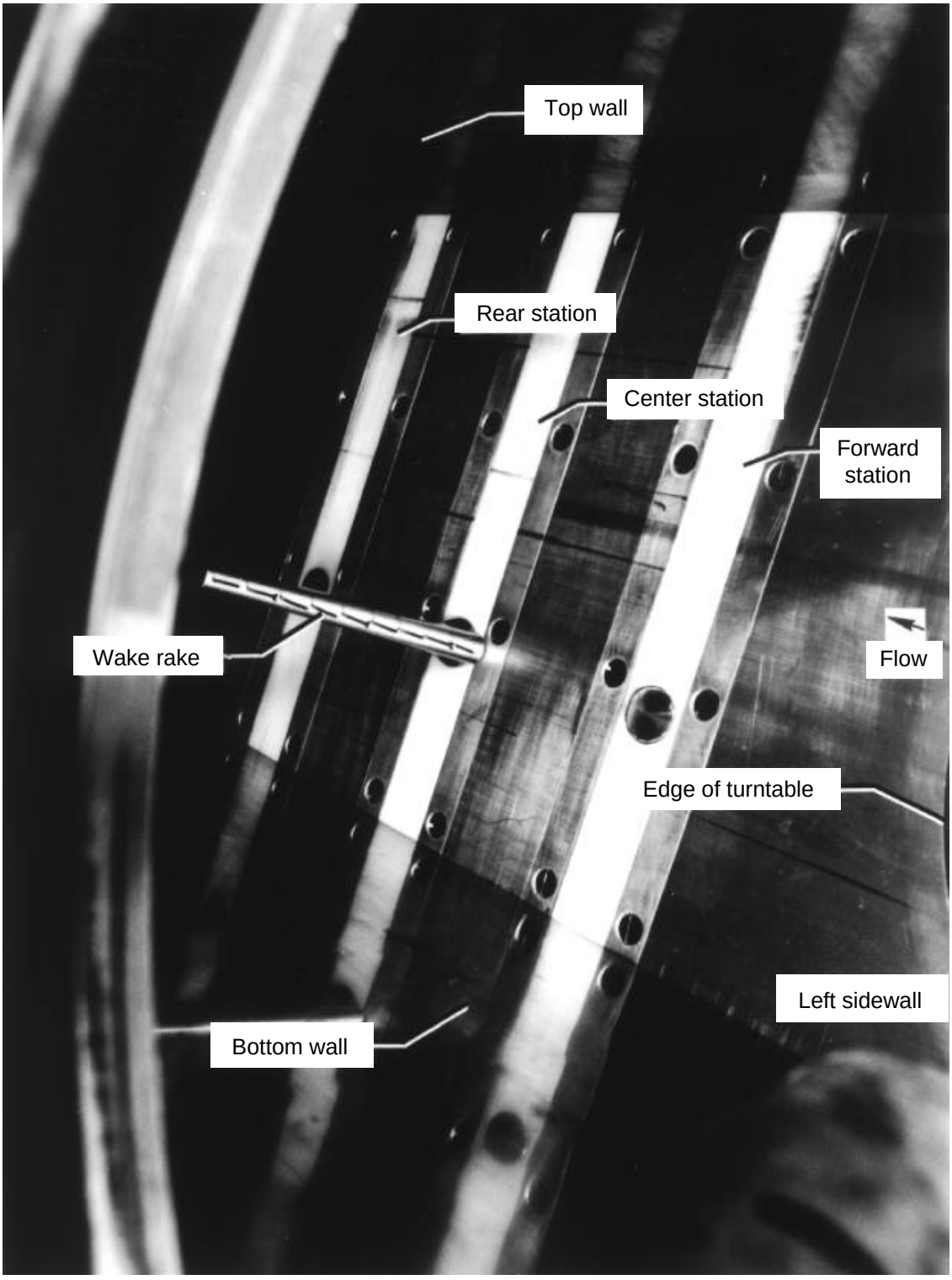

L-89-49

Figure 7. Photograph of wake survey probe mounted in center survey station. Edge of turntable just upstream of photograph.

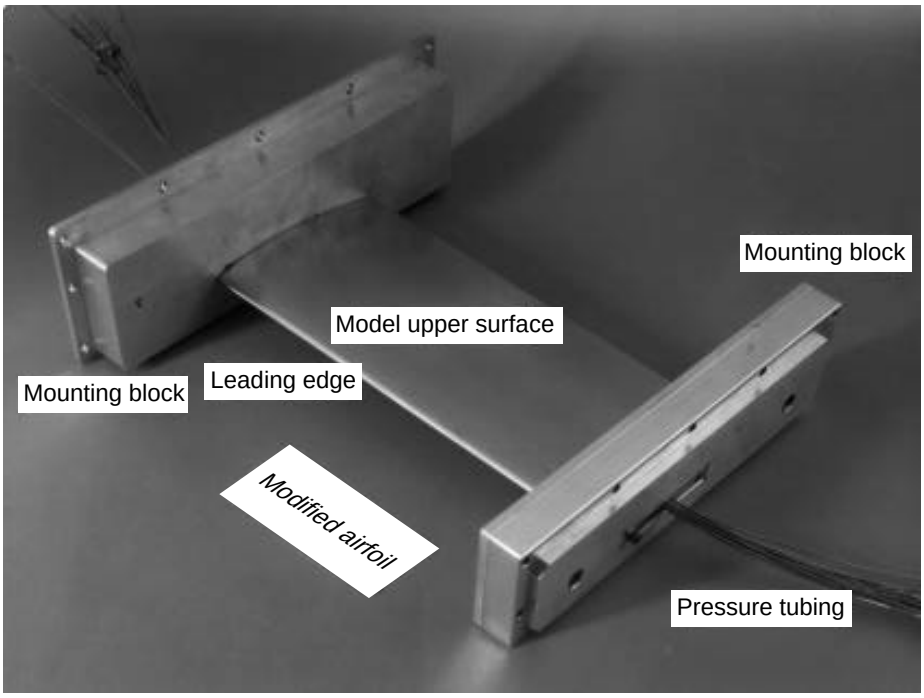

L-92-1778

Figure 8. Modified airfoil model in mounting blocks that fit into turntable.

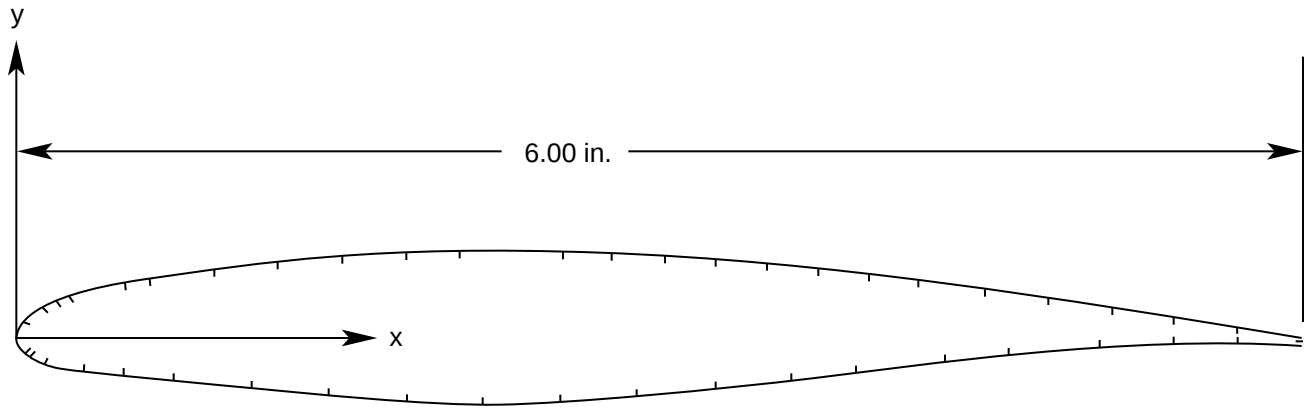

Figure 9. Modified airfoil section showing pressure orifice locations.

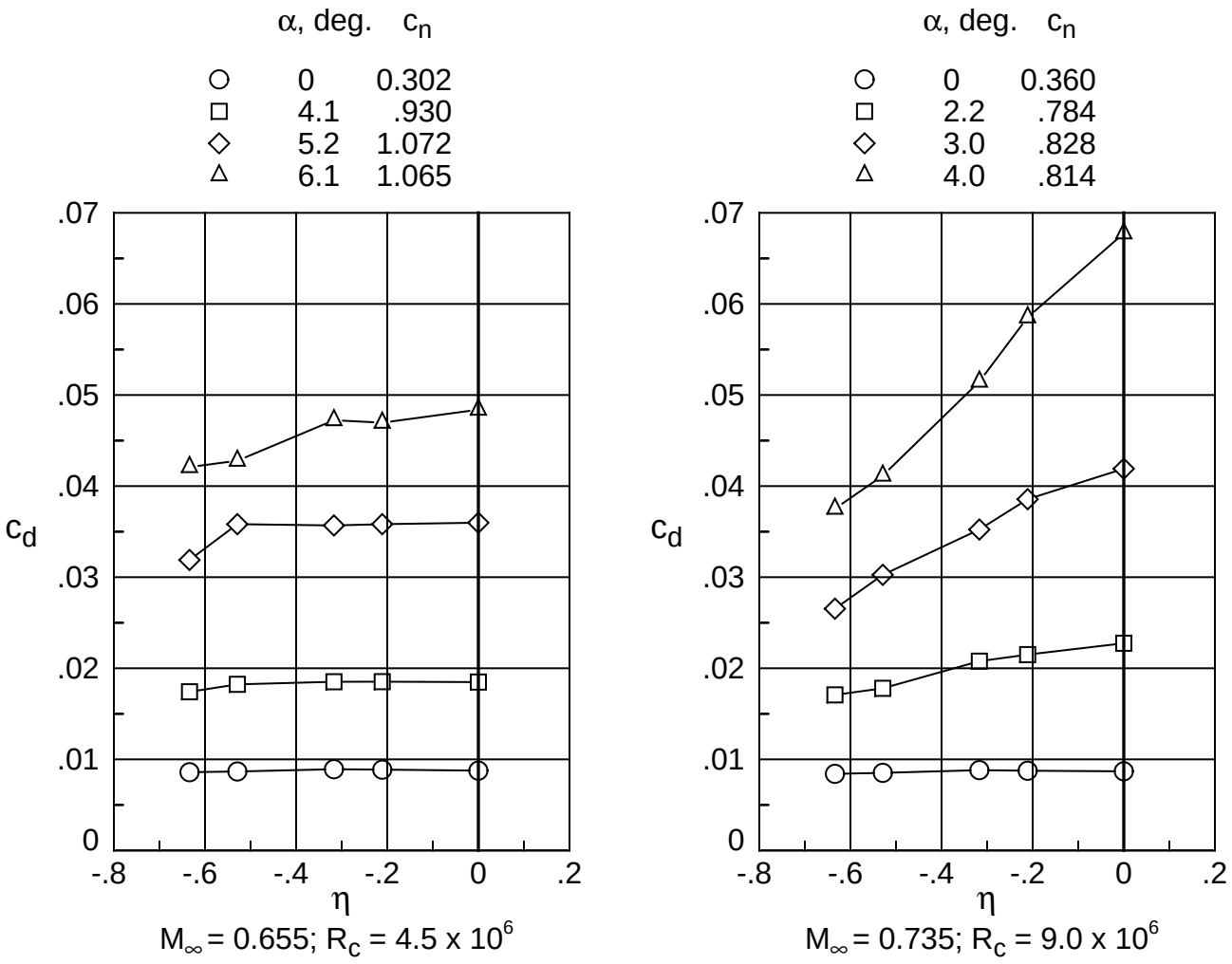

Figure 10. Spanwise section drag coefficient distributions.

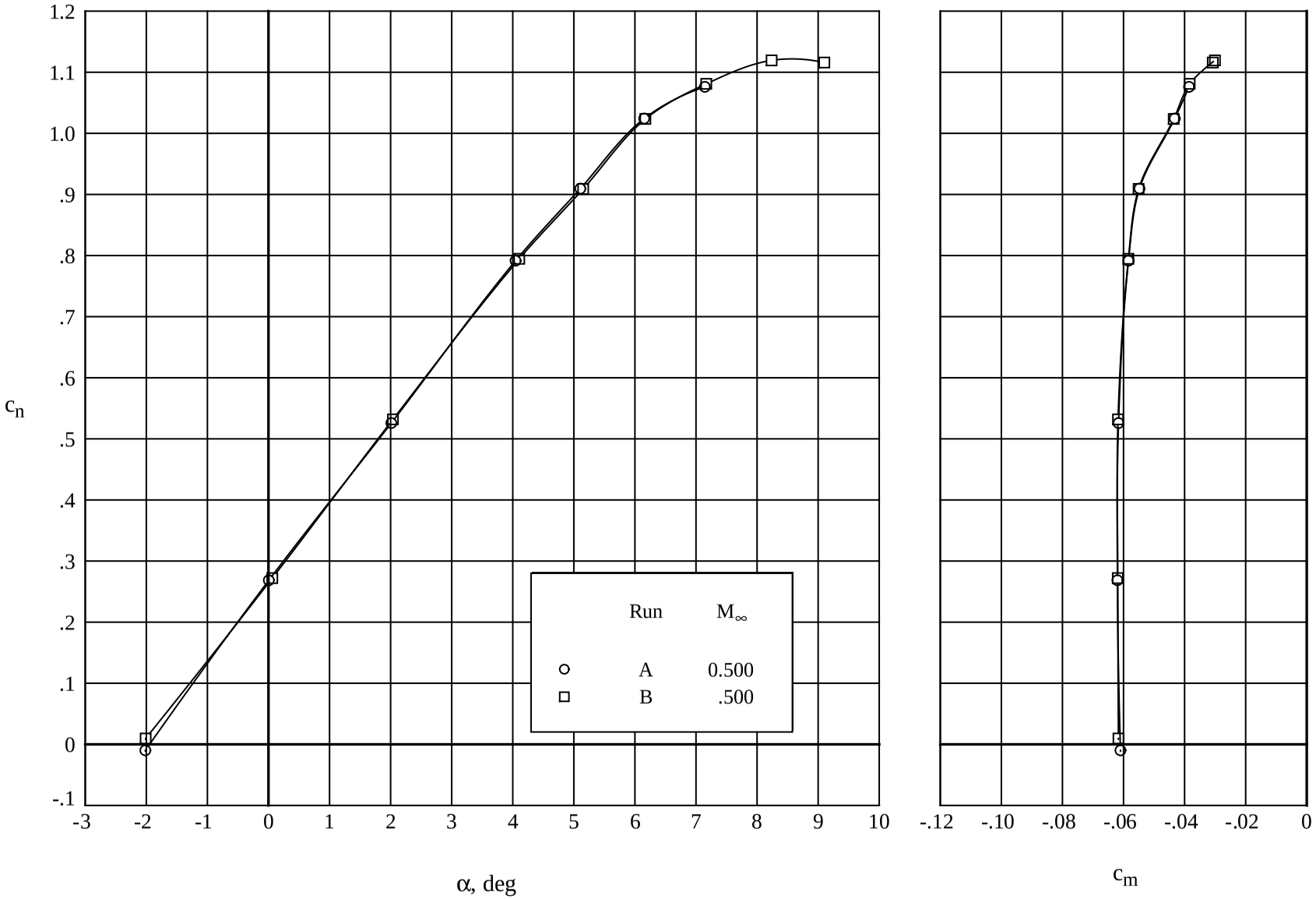

(a) Normal-force and pitching-moment coefficients.

Figure 11. Subsonic repeat runs for modified airfoil. $M_\infty = 0.500$; $R_c = 4.5 \times 10^6$.

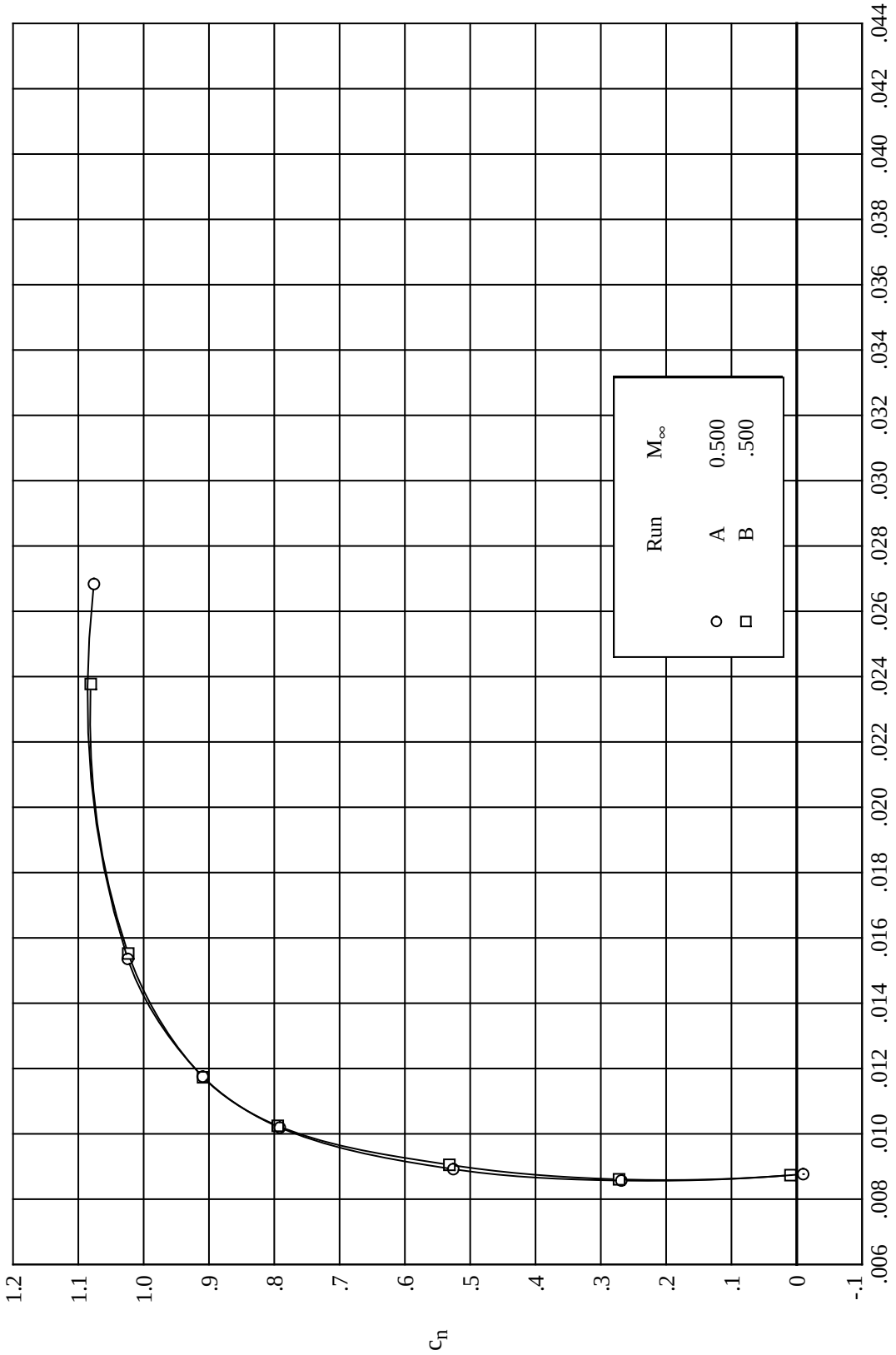

(b) Drag coefficient. $R_c = 4.5 \times 10^6$.

Figure 11. Continued.

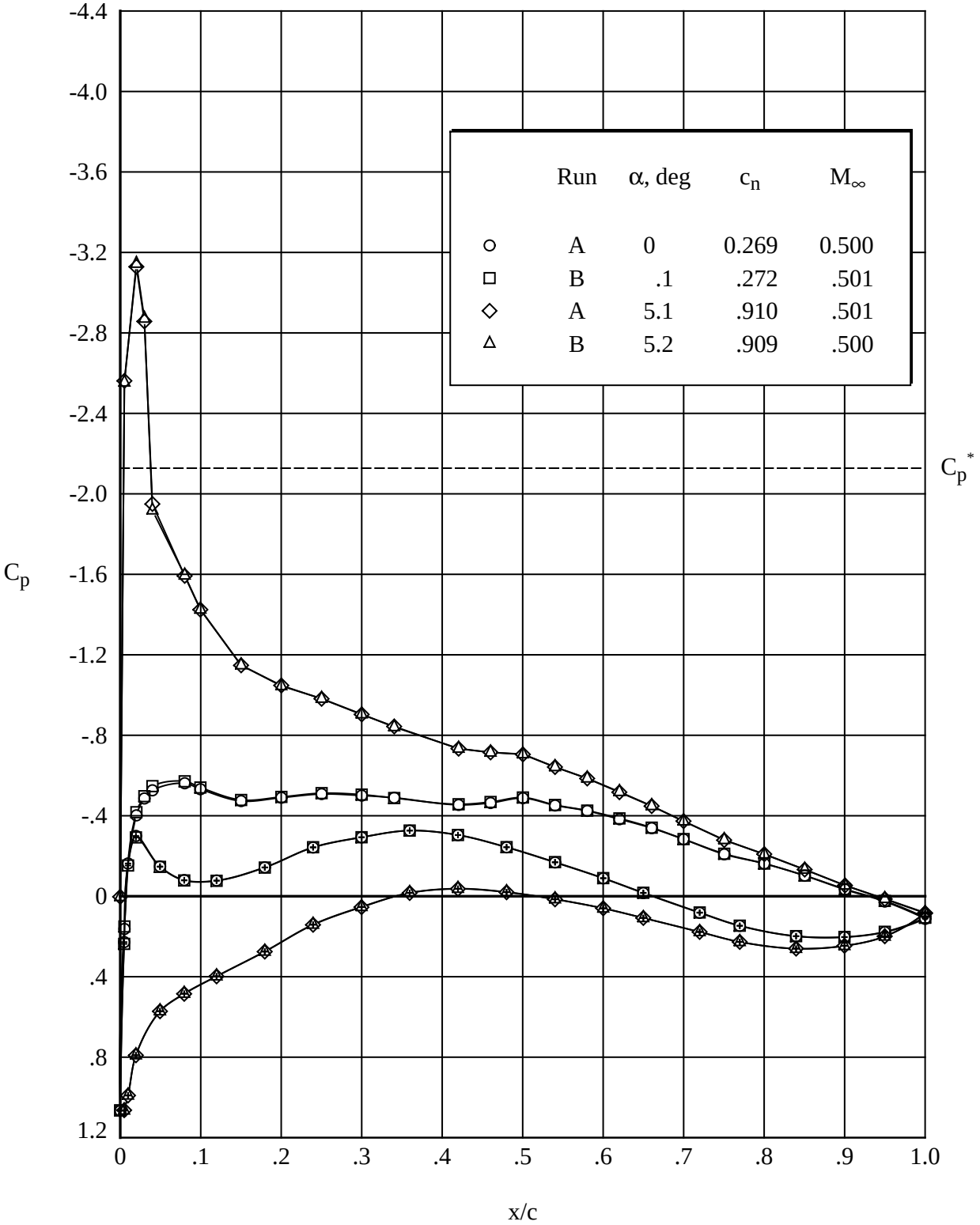

(c) Pressure distributions. Open symbols denote upper surface; "+" within symbol denotes lower surface. $R_c = 4.5 \times 10^6$.

Figure 11. Concluded.

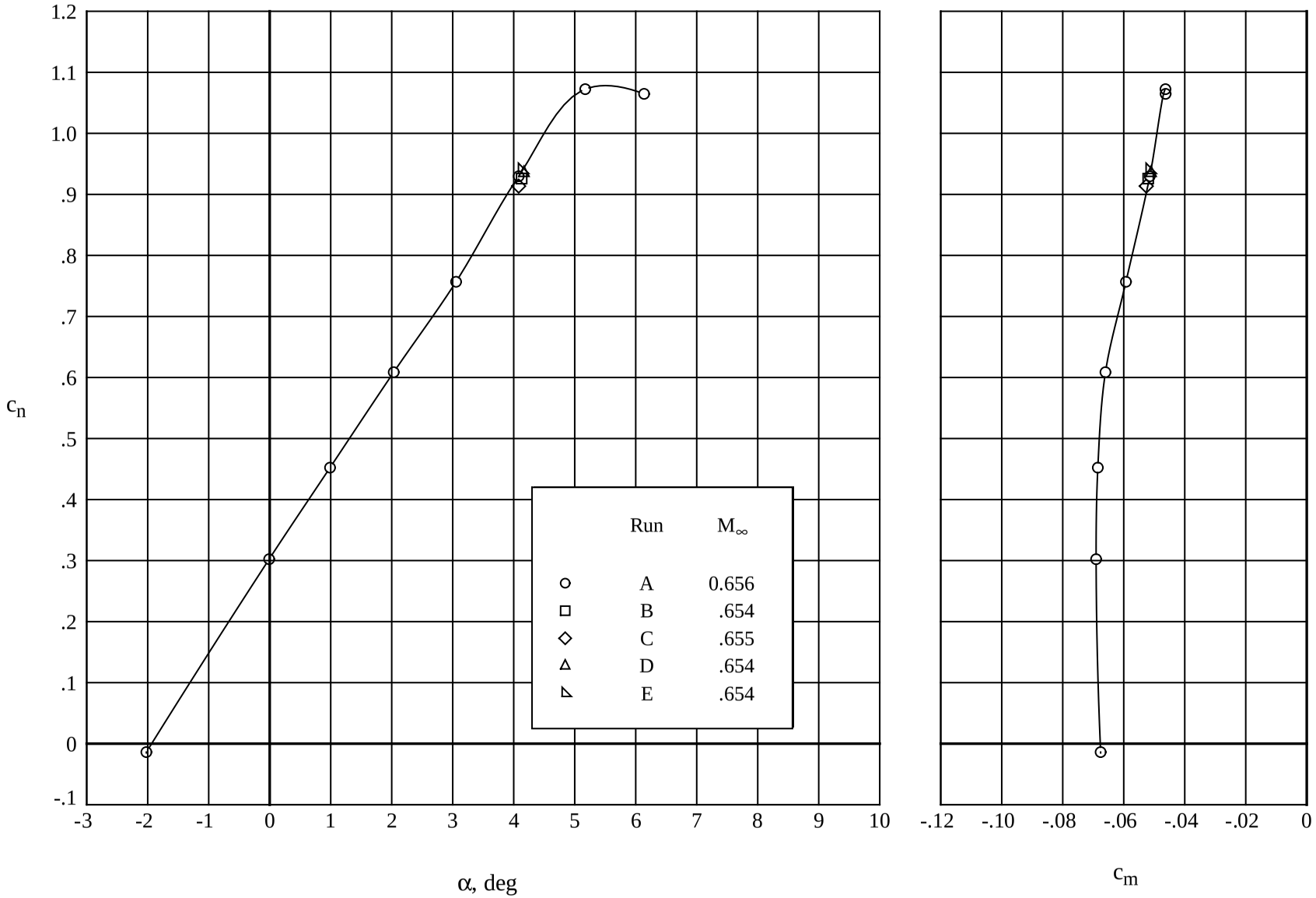

(a) Normal-force and pitching-moment coefficients.

Figure 12. Transonic repeat runs for modified airfoil. $M_\infty = 0.655$; $R_c = 4.5 \times 10^6$.

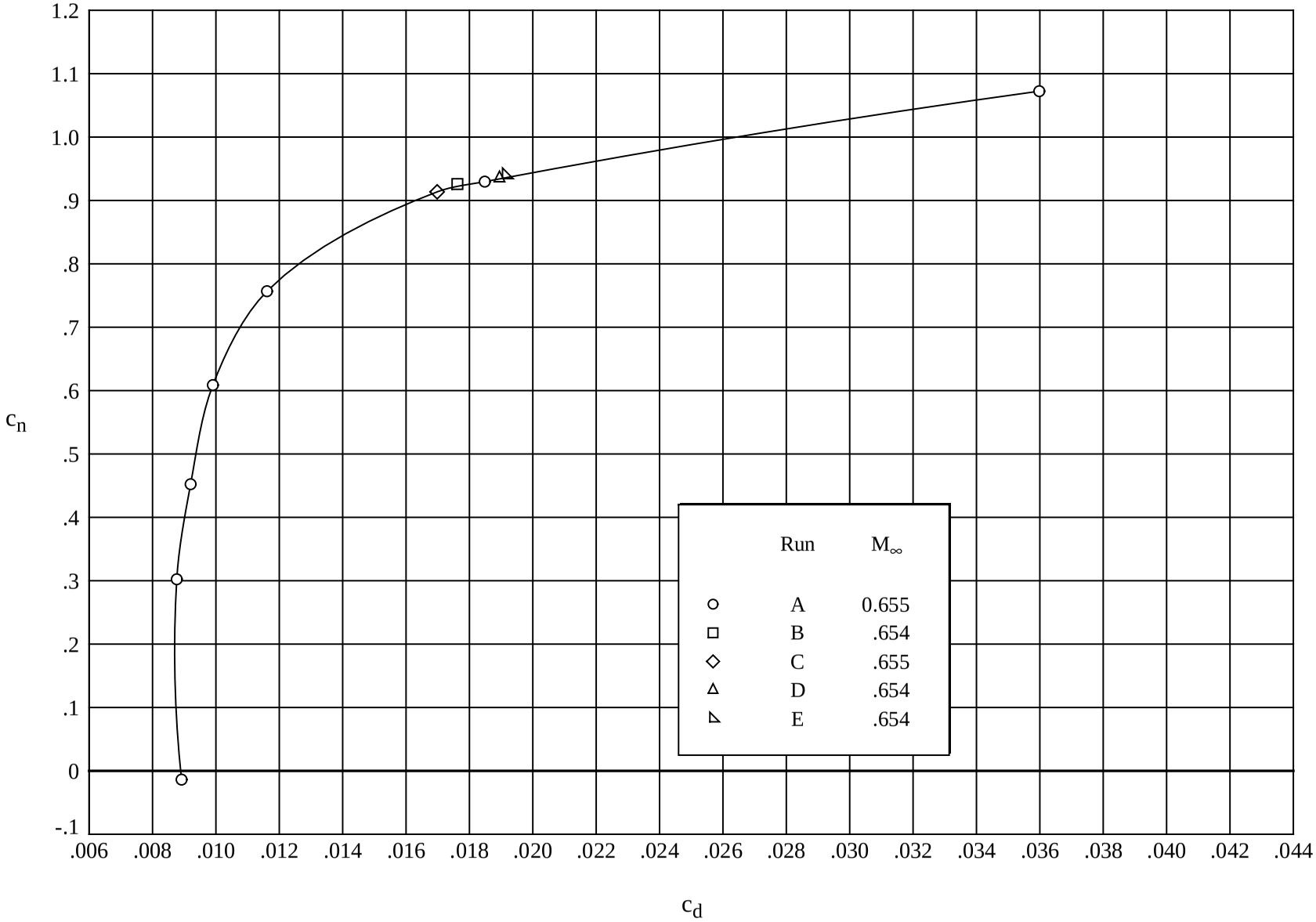

(b) Drag coefficient. $R_c = 4.5 \times 10^6$.

Figure 12. Continued.

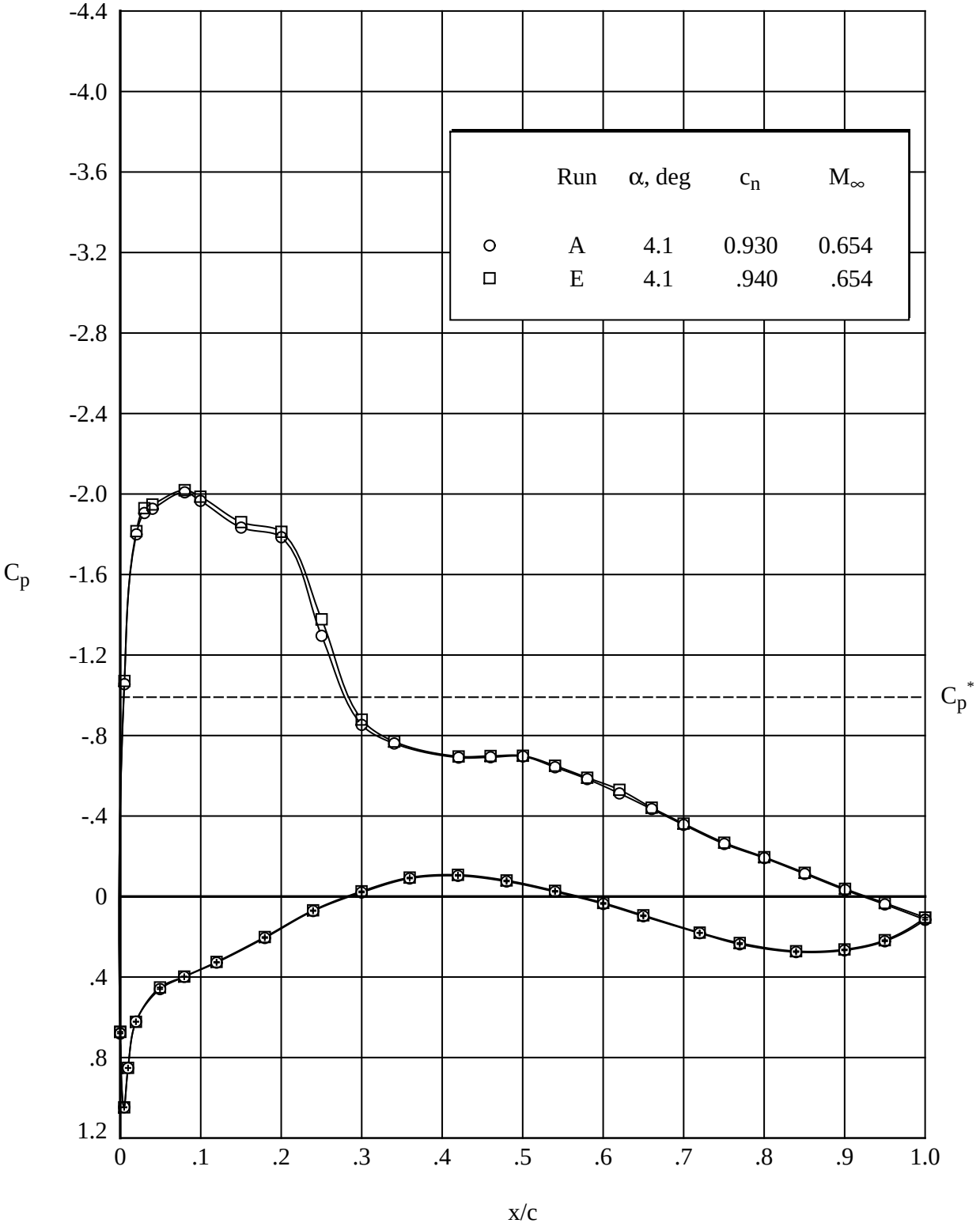

(c) Pressure distributions. Open symbols denote upper surface; "+" within symbol denotes lower surface. $R_c = 4.5 \times 10^6$.

Figure 12. Concluded.

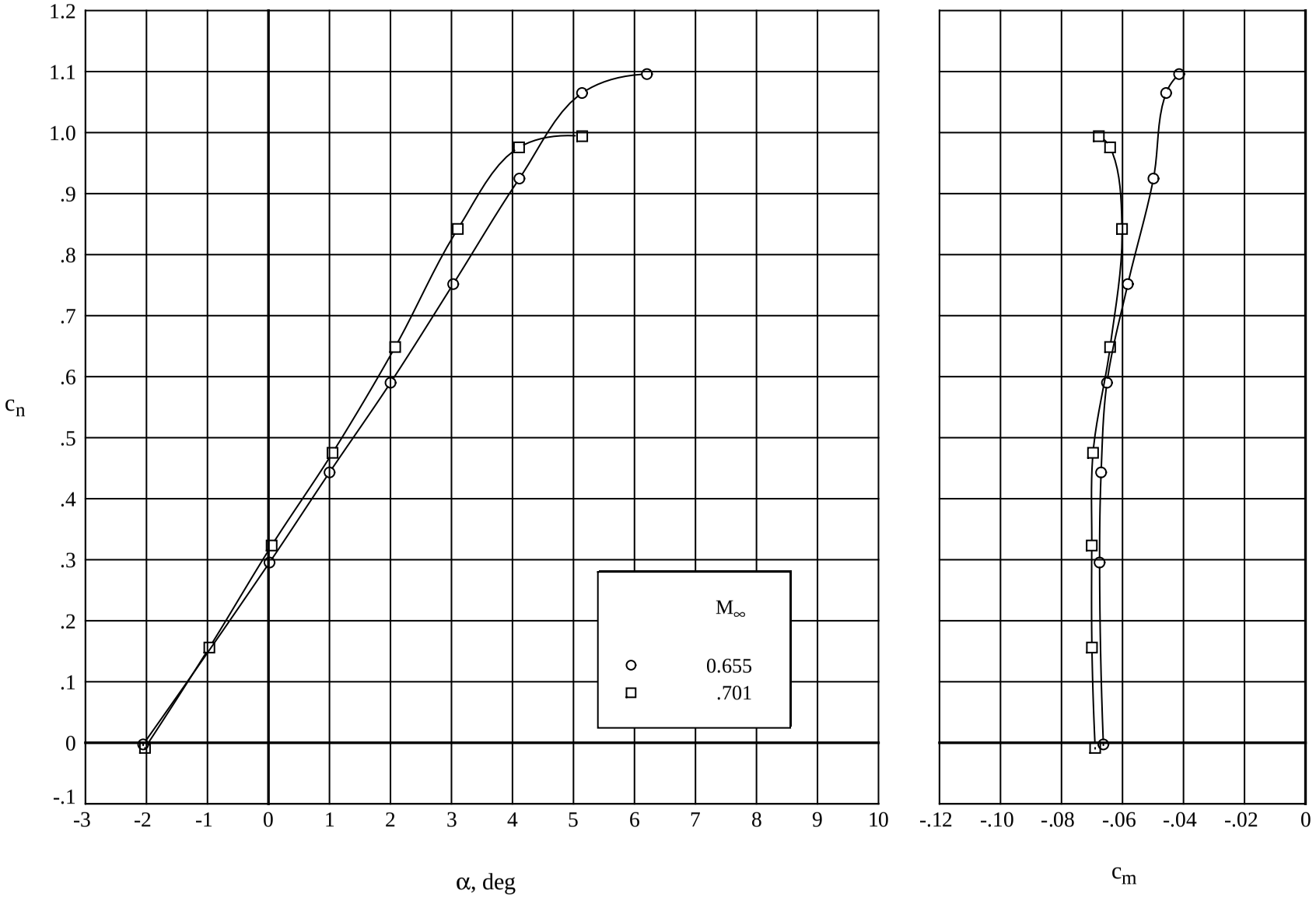

(a) Normal-force and pitching-moment coefficients. $R_c = 3.0 \times 10^6$.

Figure 13. Effect of free-stream Mach number on force and moment coefficients at constant Reynolds number for modified airfoil.

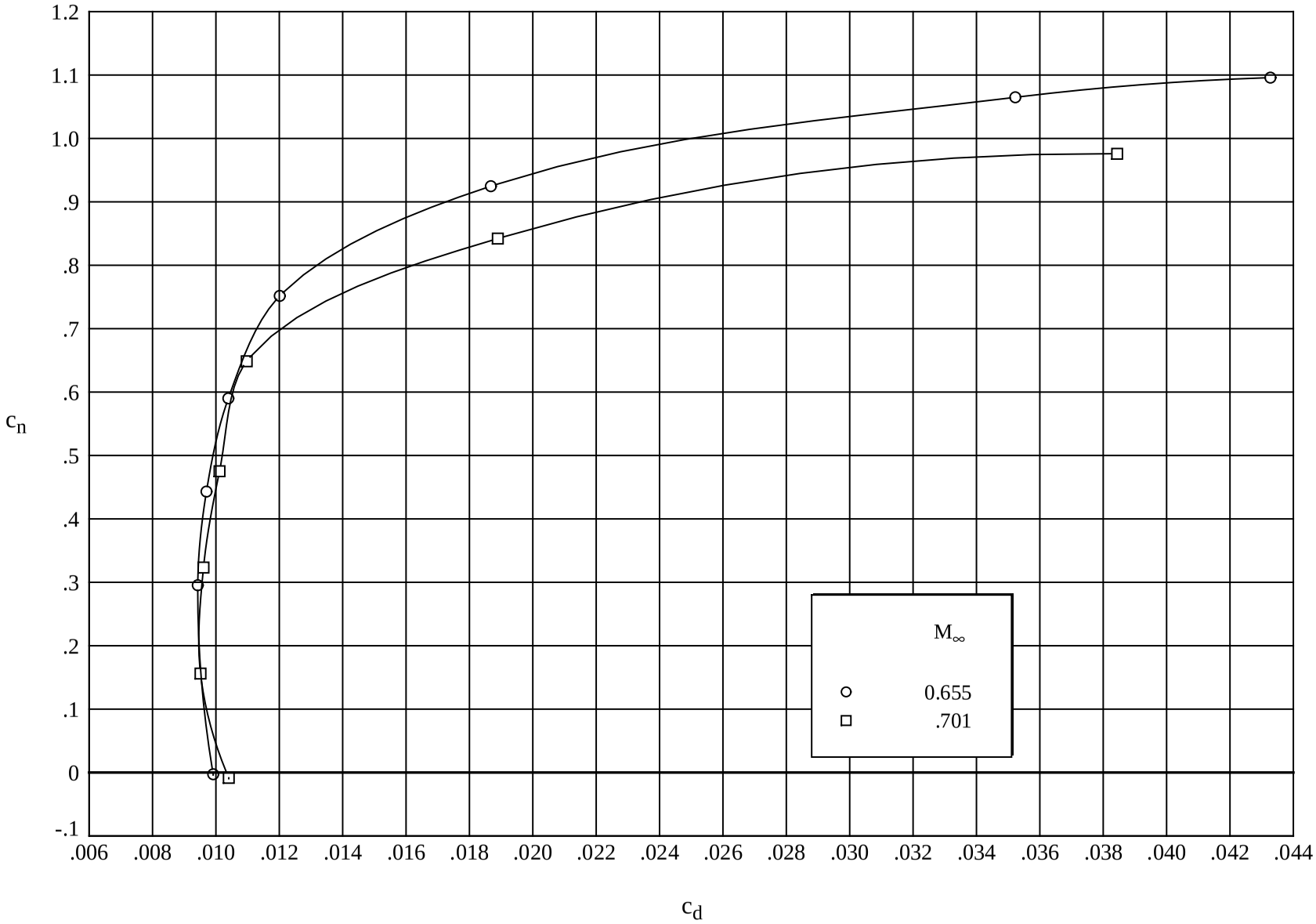

(b) Drag coefficient. $R_c = 3.0 \times 10^6$.

Figure 13. Continued.

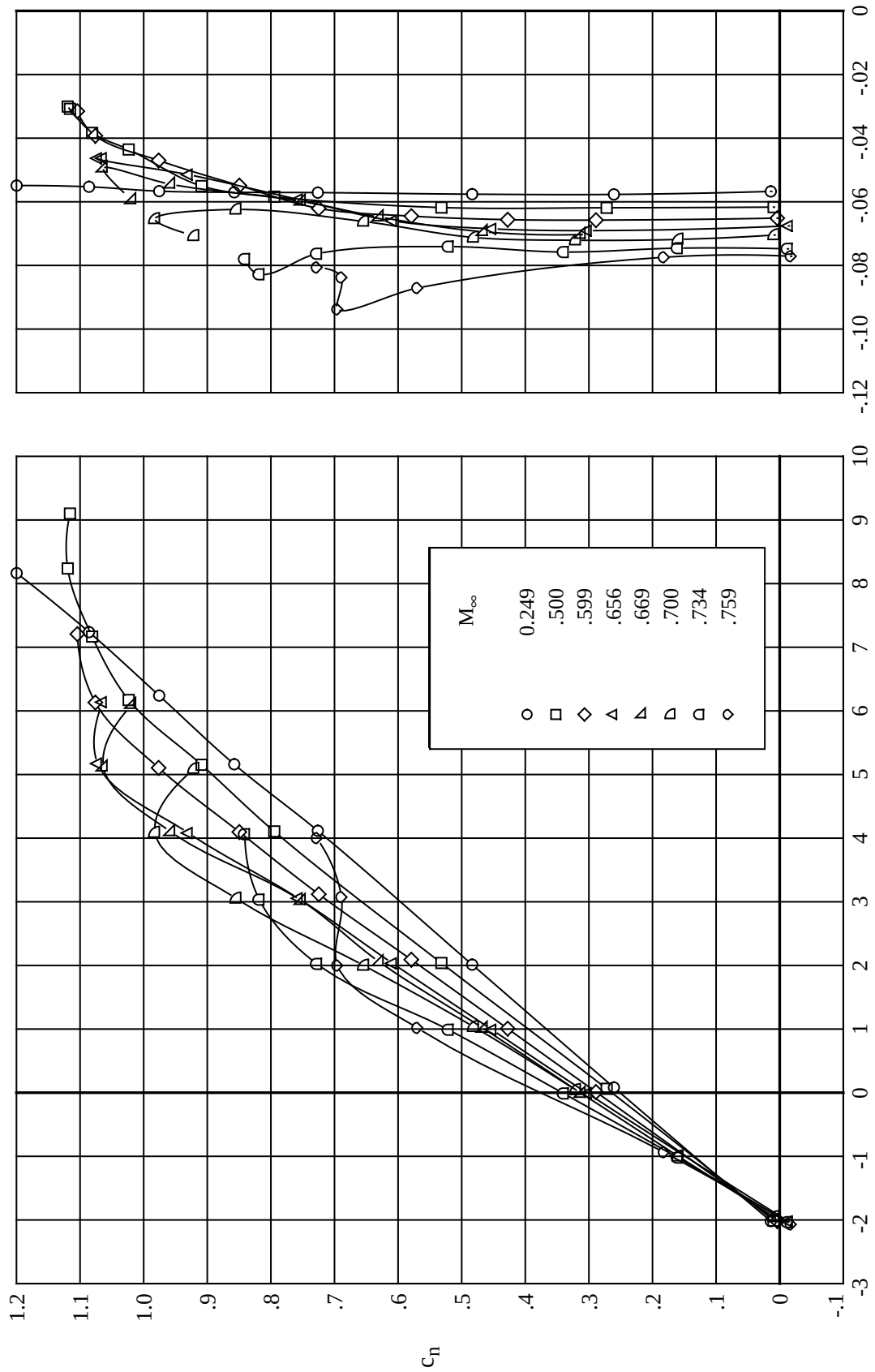

(c) Normal-force and pitching-moment coefficients. $R_c = 4.5 \times 10^6$.

Figure 13. Continued.

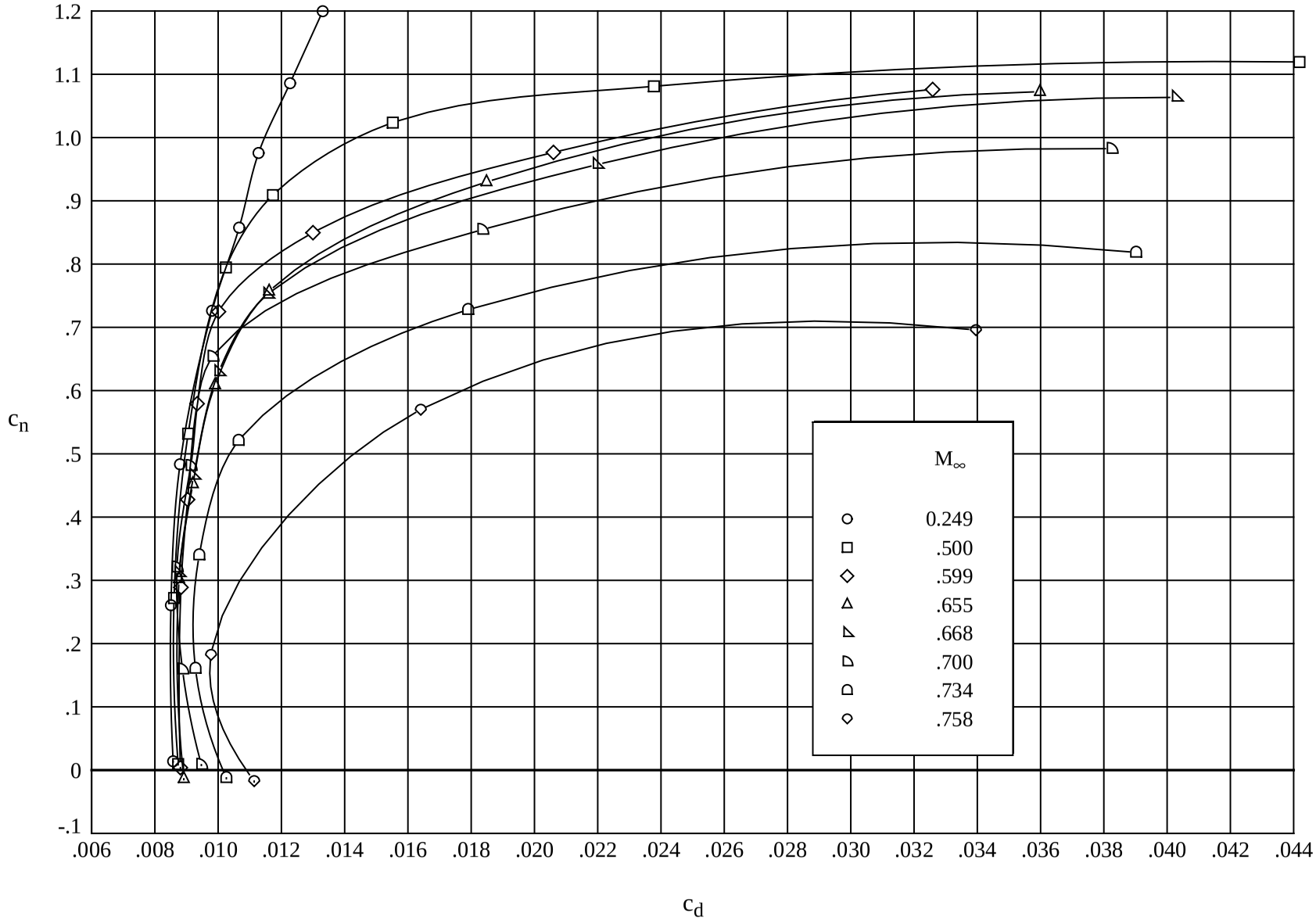

(d) Drag coefficient. $R_c = 4.5 \times 10^6$.

Figure 13. Continued.

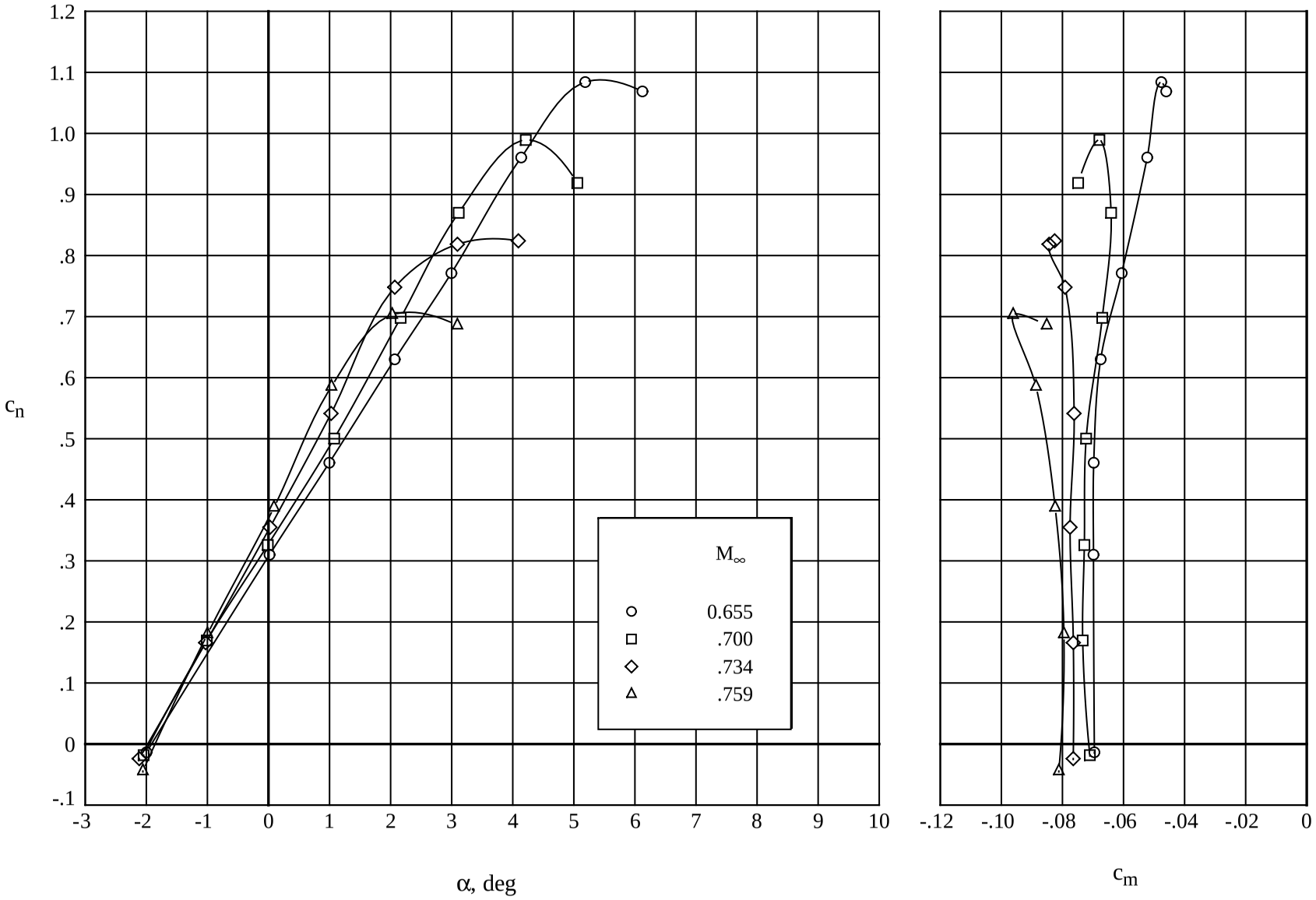

(e) Normal-force and pitching-moment coefficients. $R_c = 6.5 \times 10^6$.

Figure 13. Continued.

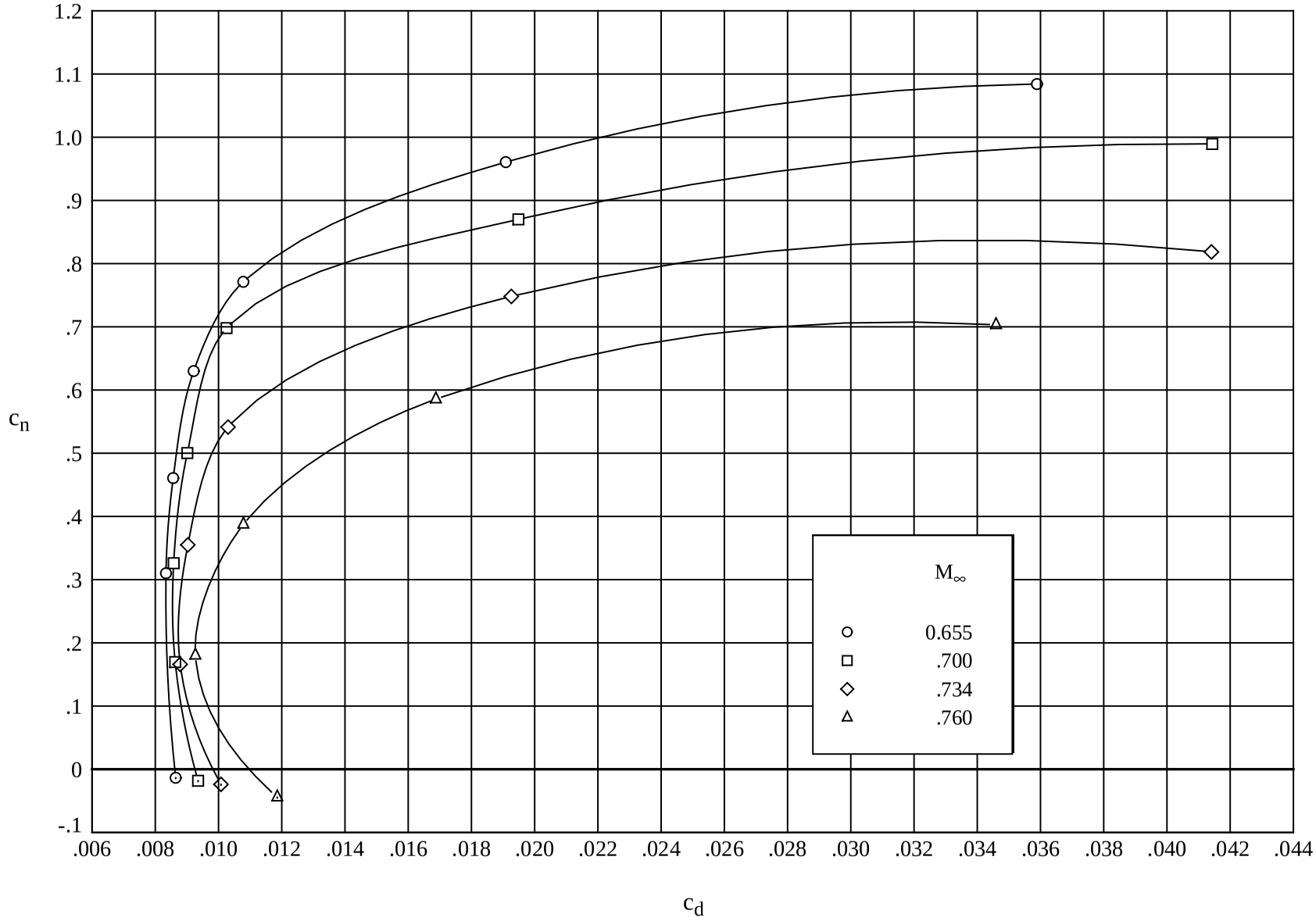

(f) Drag coefficient. $R_c = 6.5 \times 10^6$.

Figure 13. Continued.

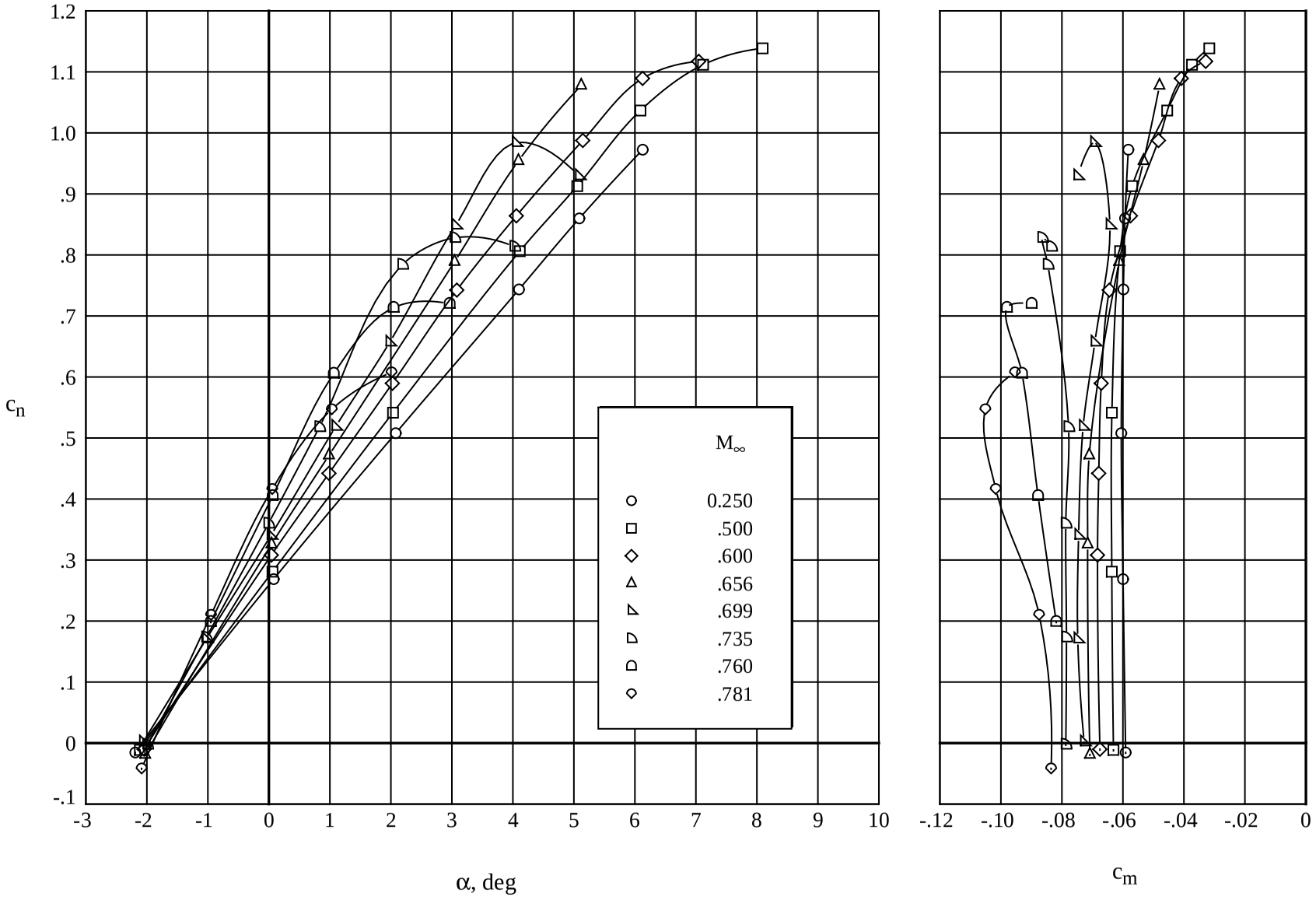

(g) Normal-force and pitching-moment coefficients. $R_c = 9.0 \times 10^6$.

Figure 13. Continued.

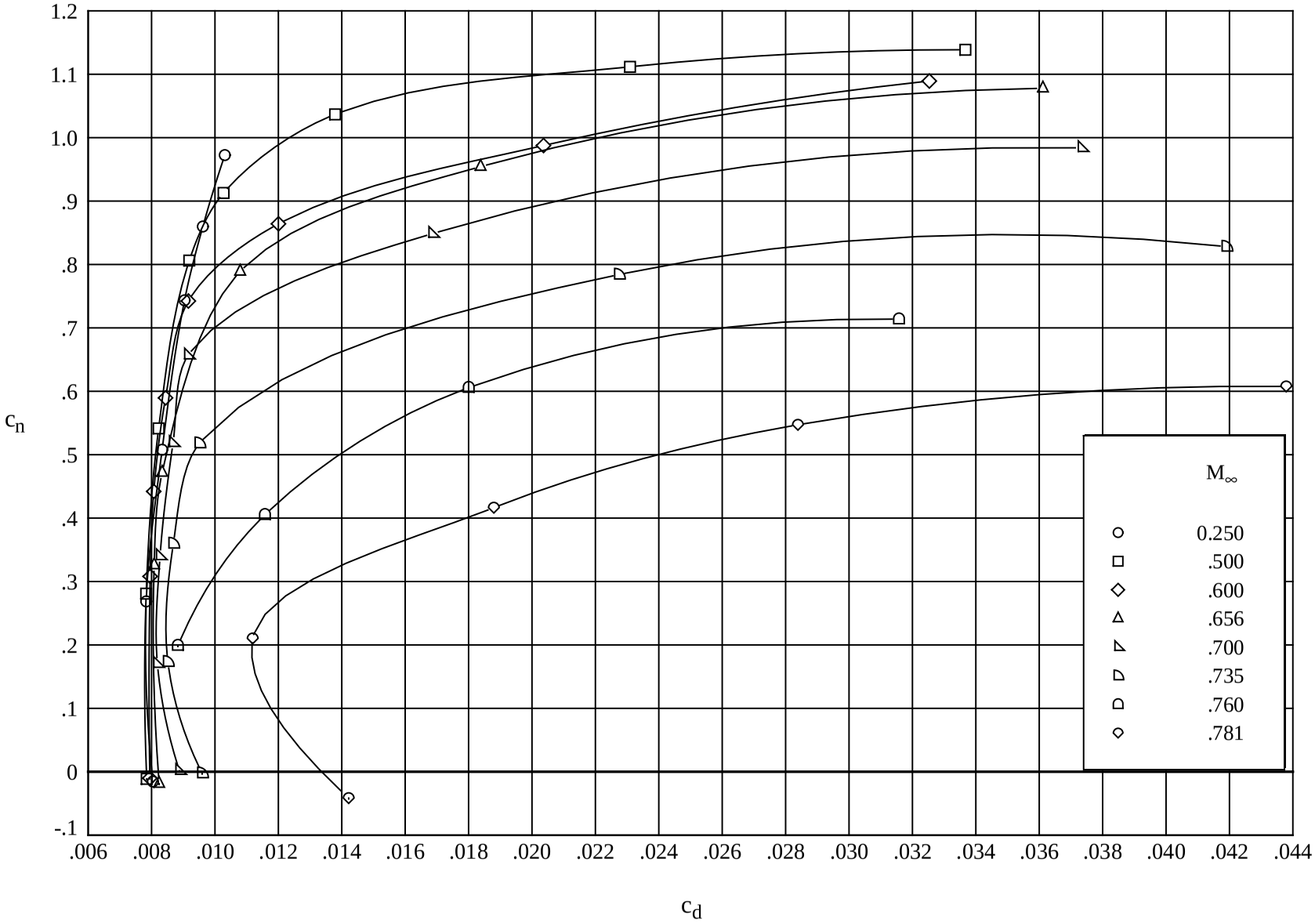

(h) Drag coefficient. $R_c = 9.0 \times 10^6$.

Figure 13. Continued.

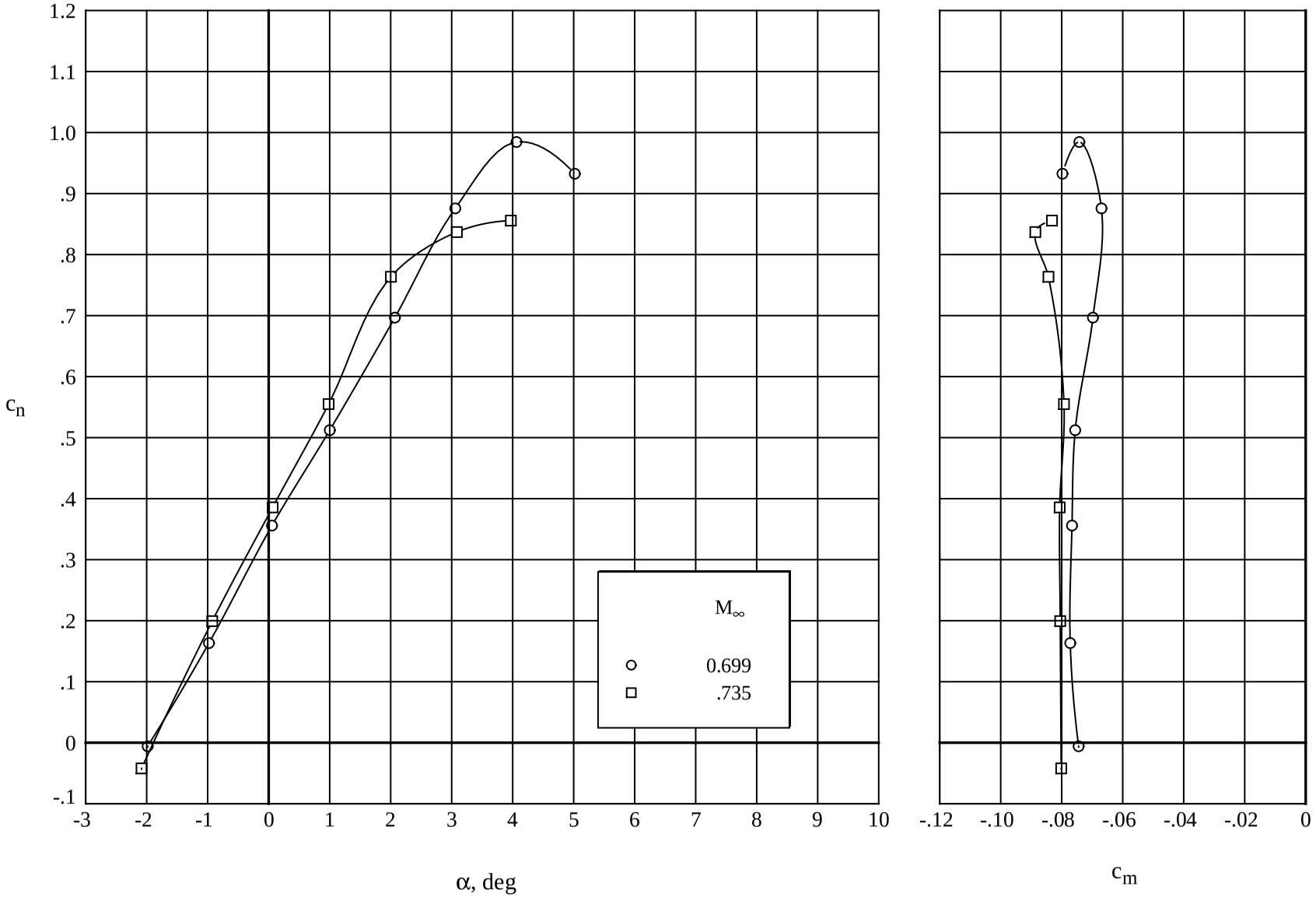

(i) Normal-force and pitching-moment coefficients. $R_c = 13.5 \times 10^6$.

Figure 13. Continued.

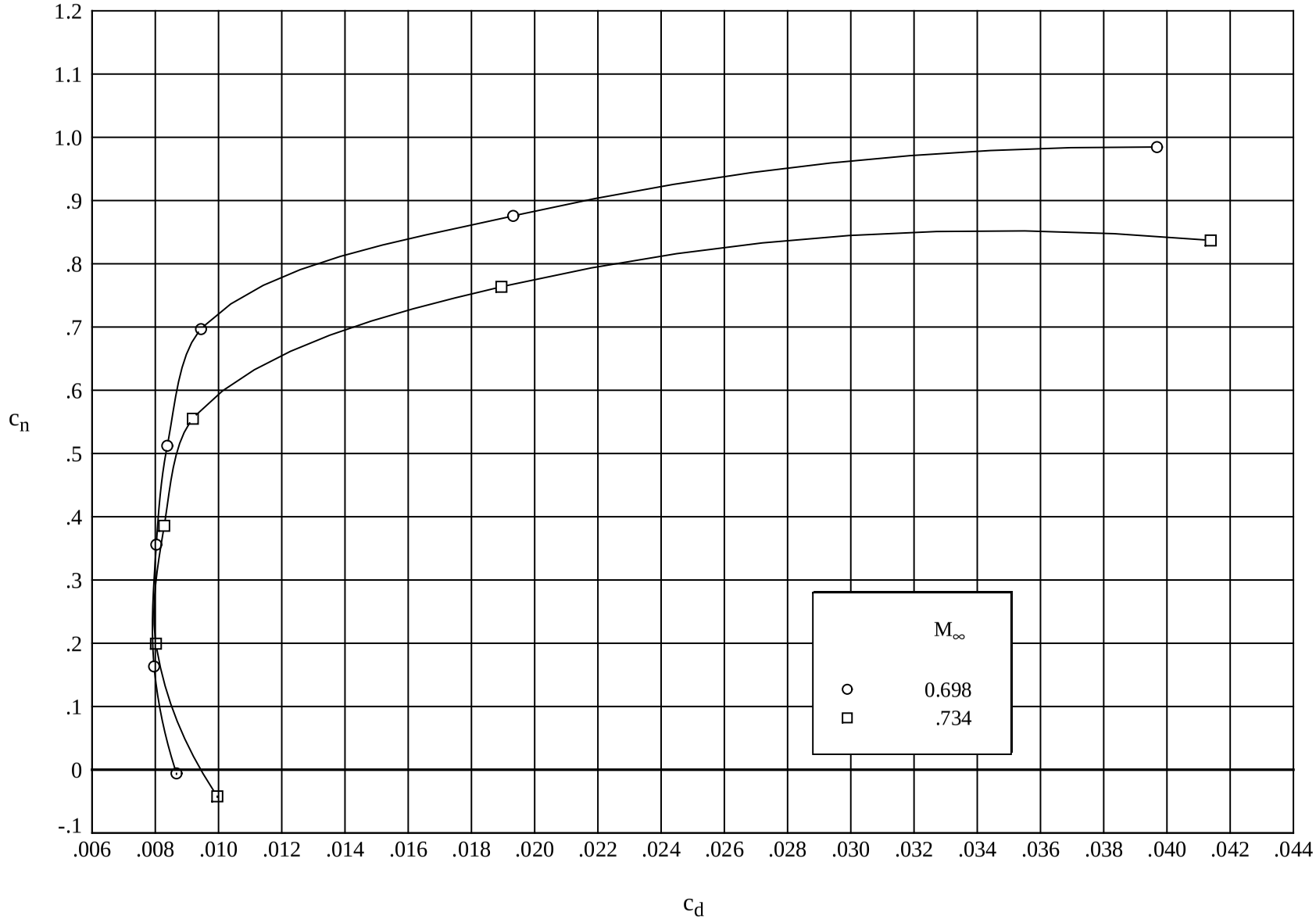

(j) Drag coefficient. $R_c = 13.5 \times 10^6$.

Figure 13. Concluded.

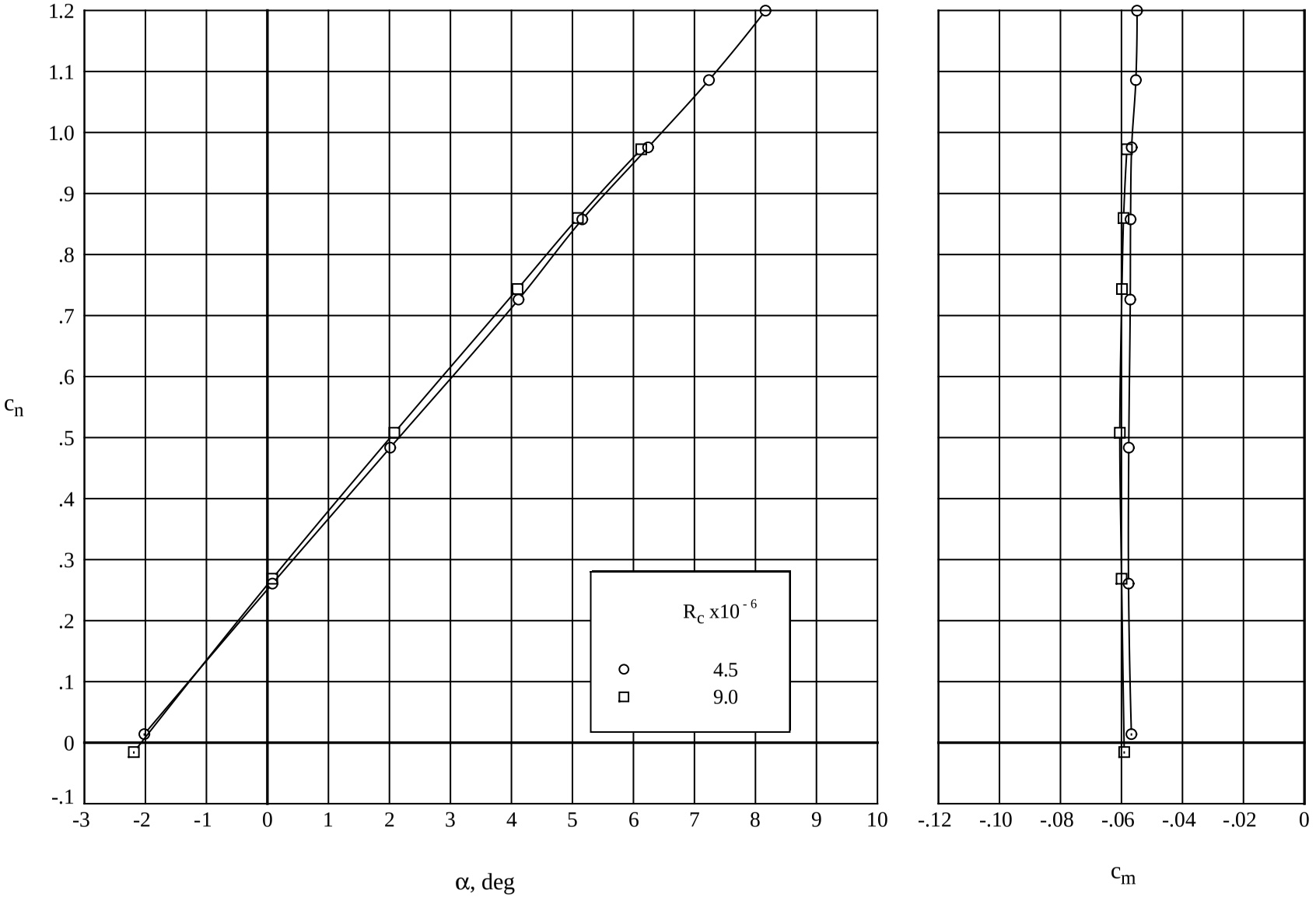

(a) Normal-force and pitching-moment coefficients. M_∞ = 0.250.

Figure 14. Effect of free-stream Reynolds number on force and moment coefficients at constant Mach number for modified airfoil.

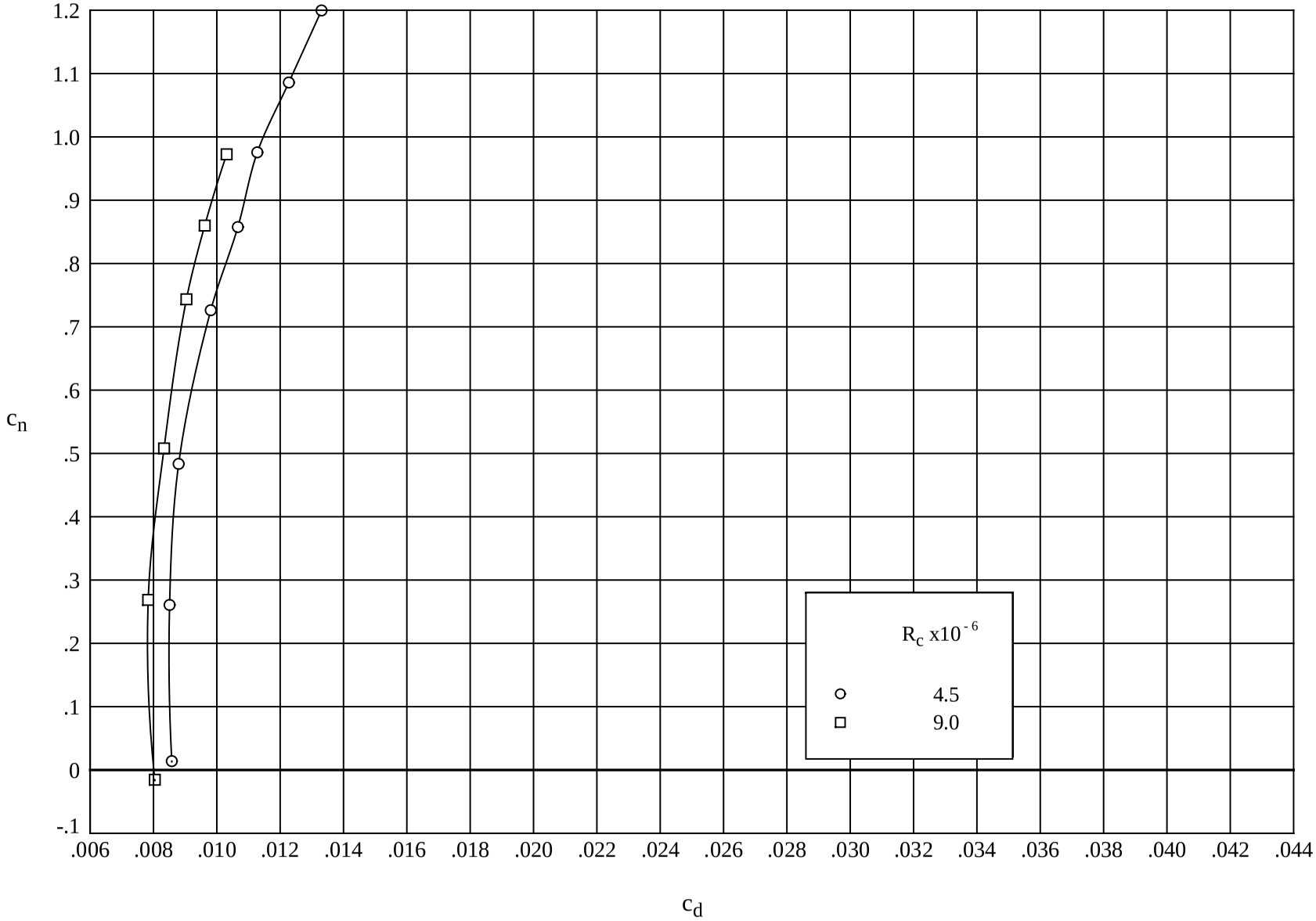

(b) Drag coefficient. M_∞ = 0.250.

Figure 14. Continued.

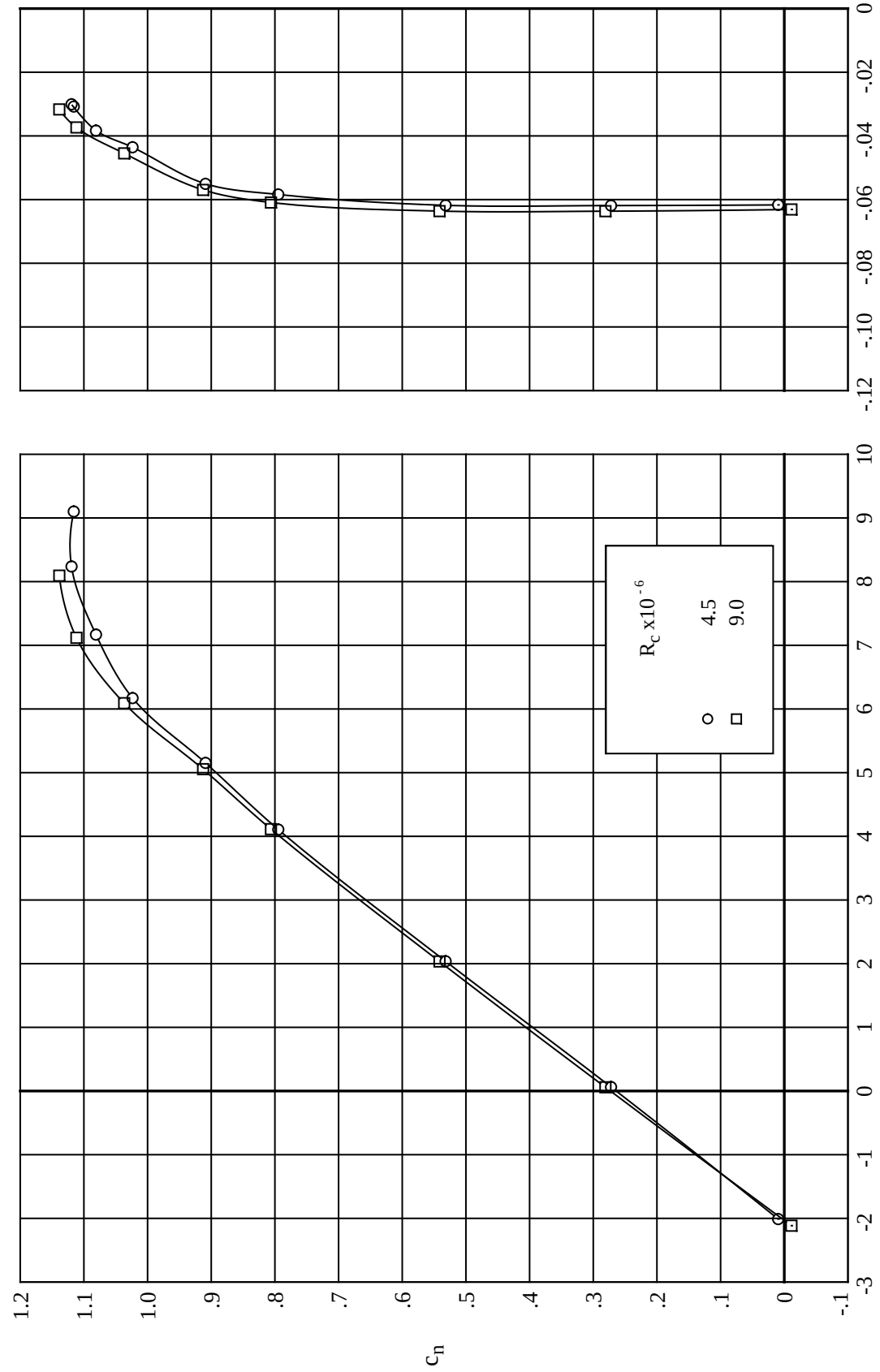

(c) Normal-force and pitching-moment coefficients. $M_\infty = 0.500$.

Figure 14. Continued.

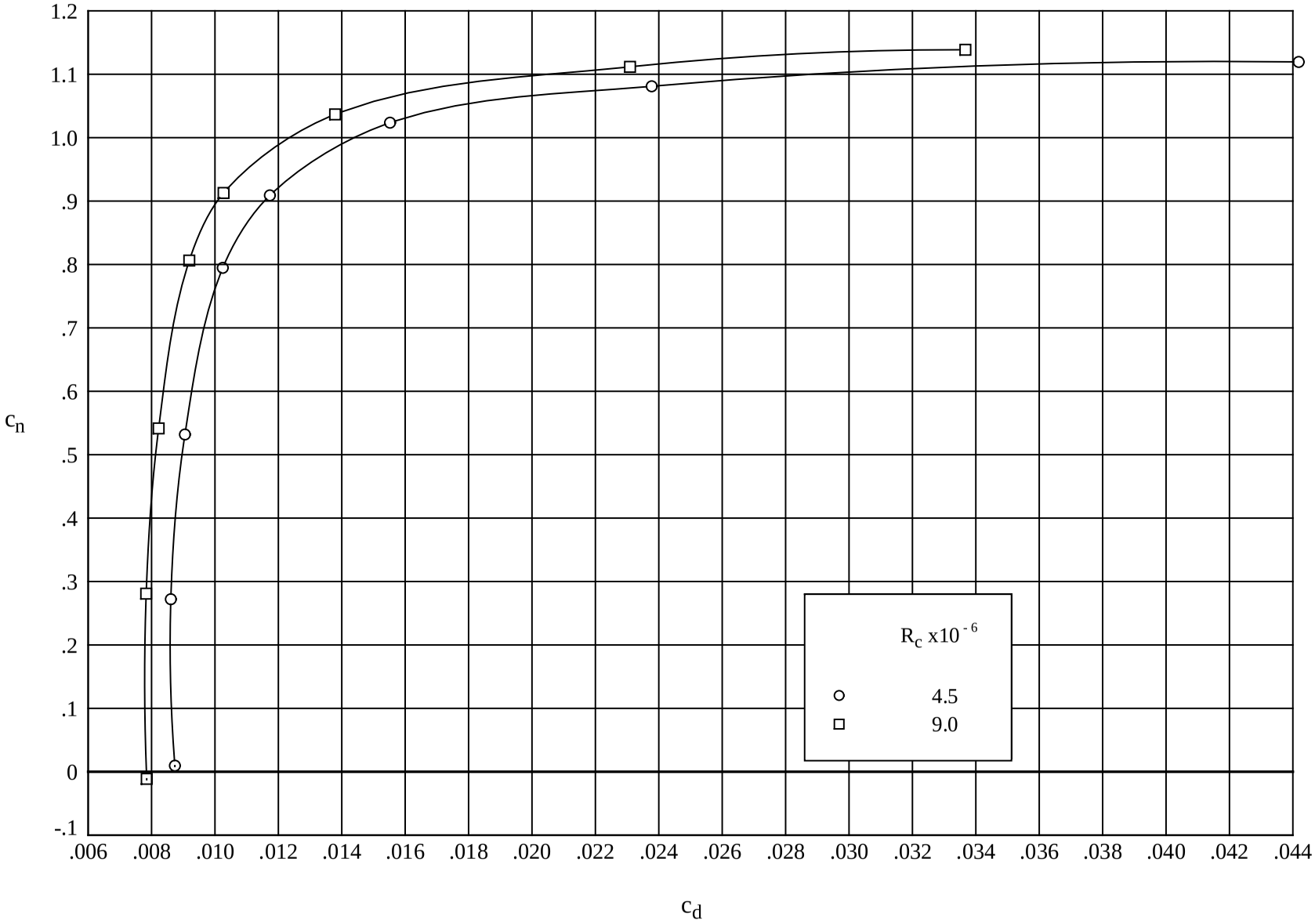

(d) Drag coefficient. M_∞ = 0.500.

Figure 14. Continued.

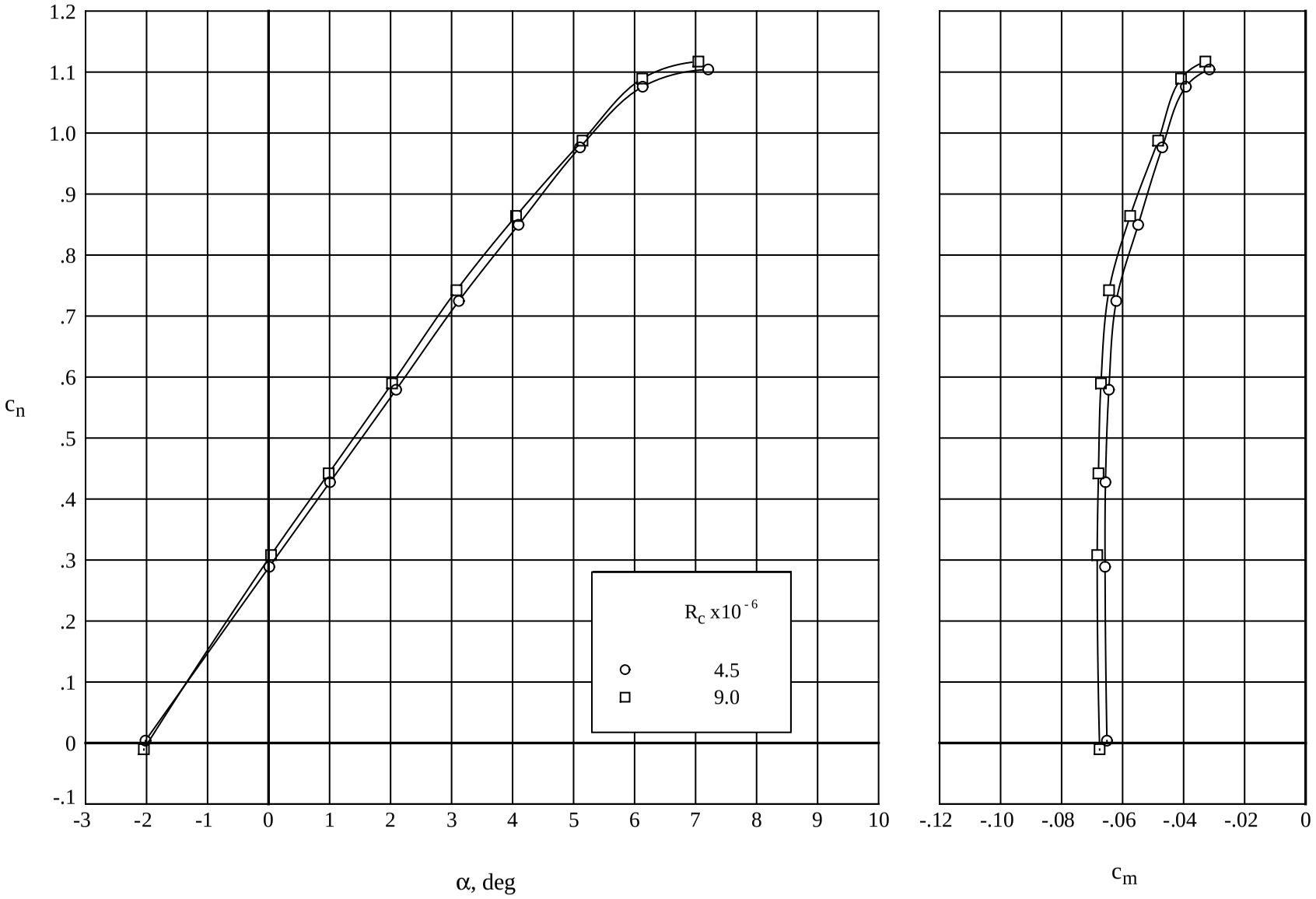

(e) Normal-force and pitching-moment coefficients. M_∞ = 0.600.

Figure 14. Continued.

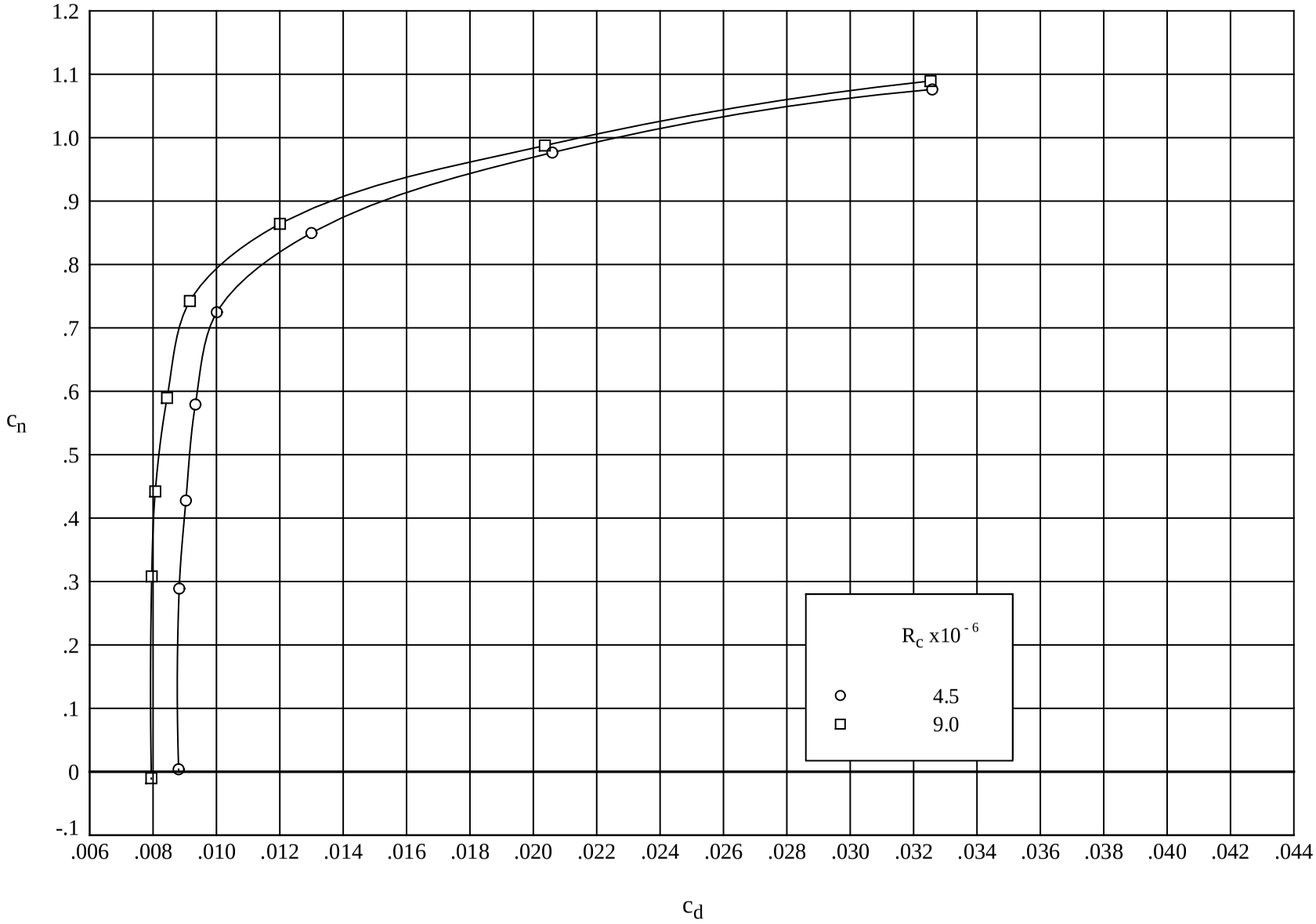

(f) Drag coefficient. M_∞ = 0.600.

Figure 14. Continued.

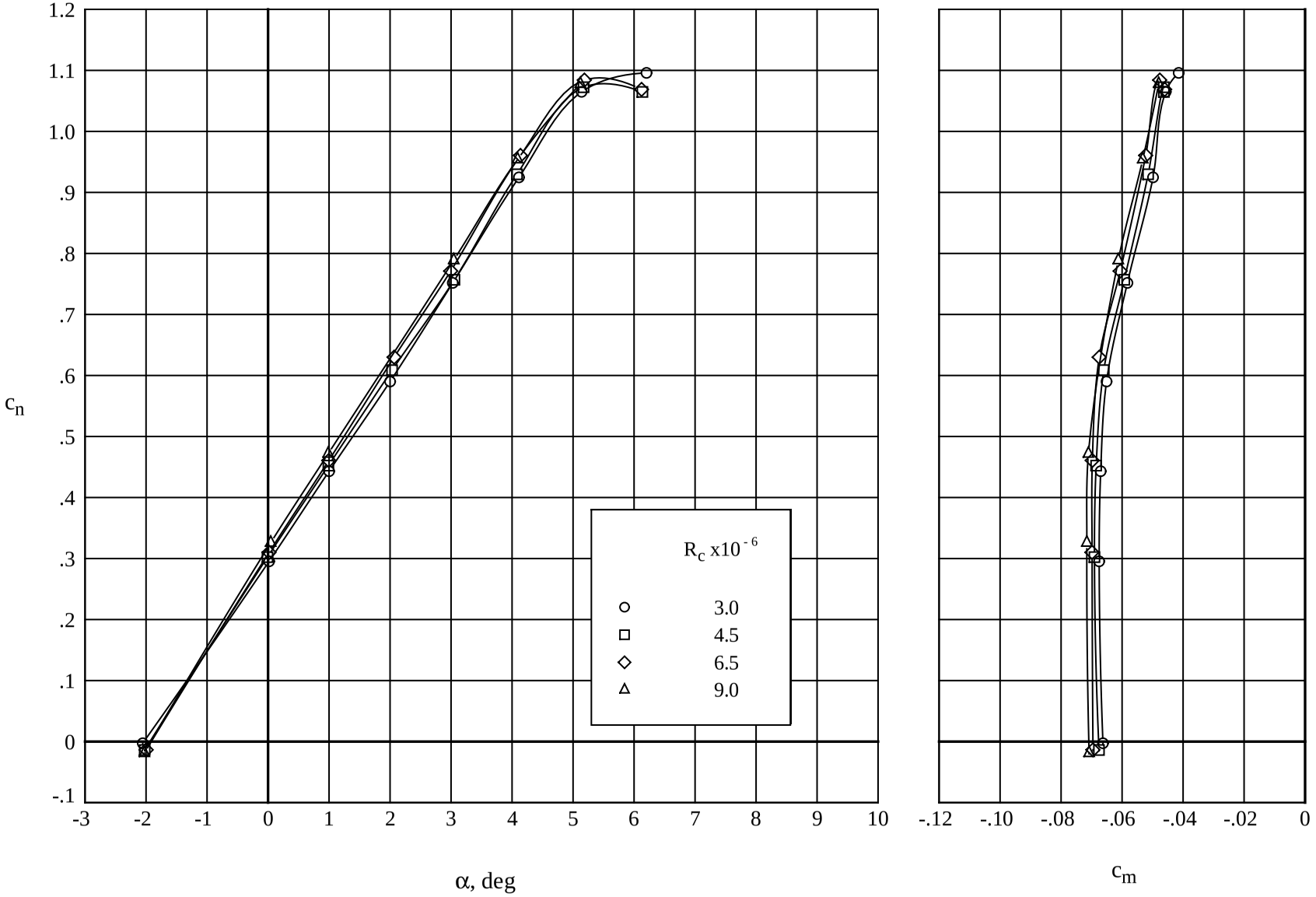

(g) Normal-force and pitching-moment coefficients. M_∞ = 0.655.

Figure 14. Continued.

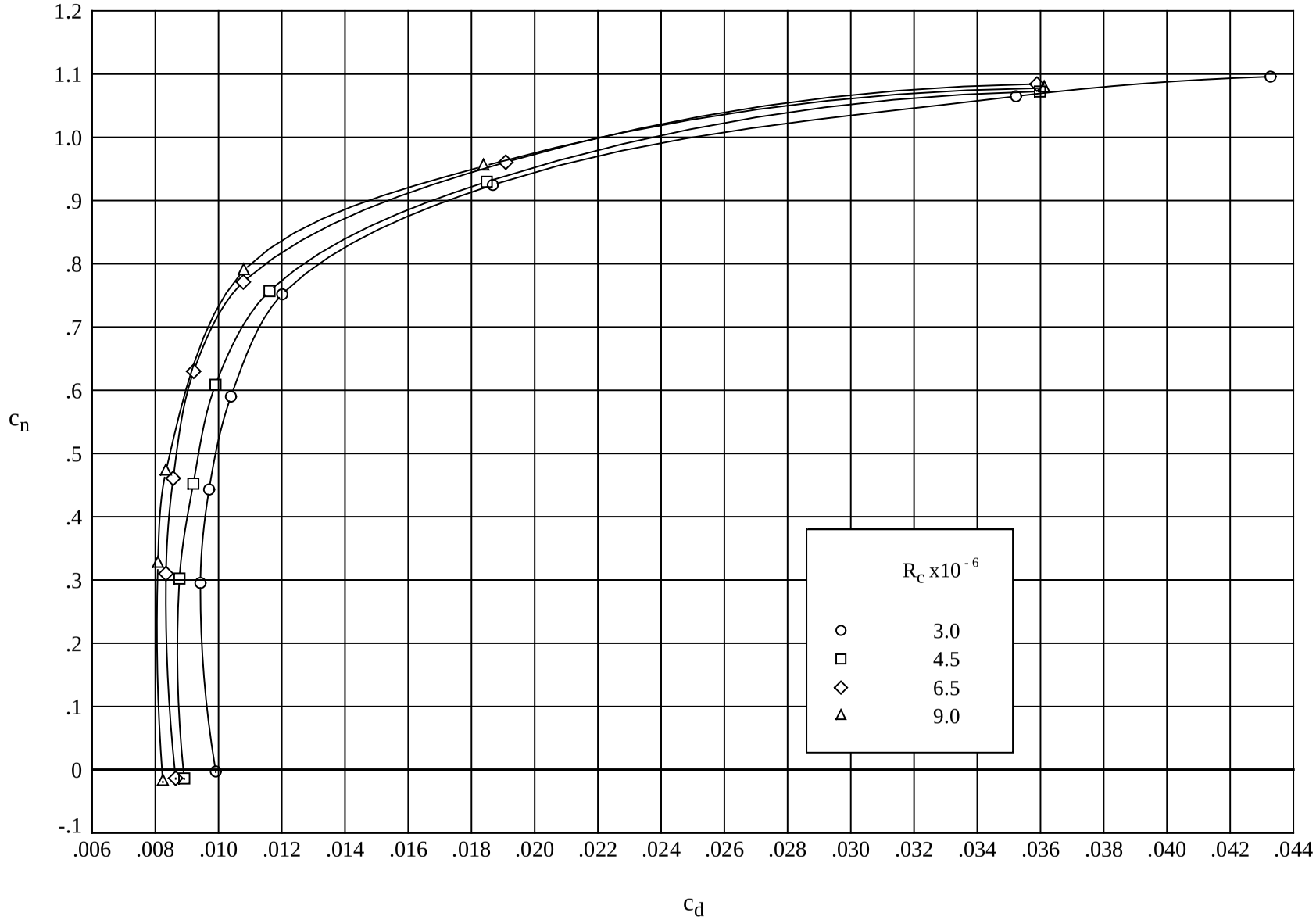

(h) Drag coefficient. M_∞ = 0.655.

Figure 14. Continued.

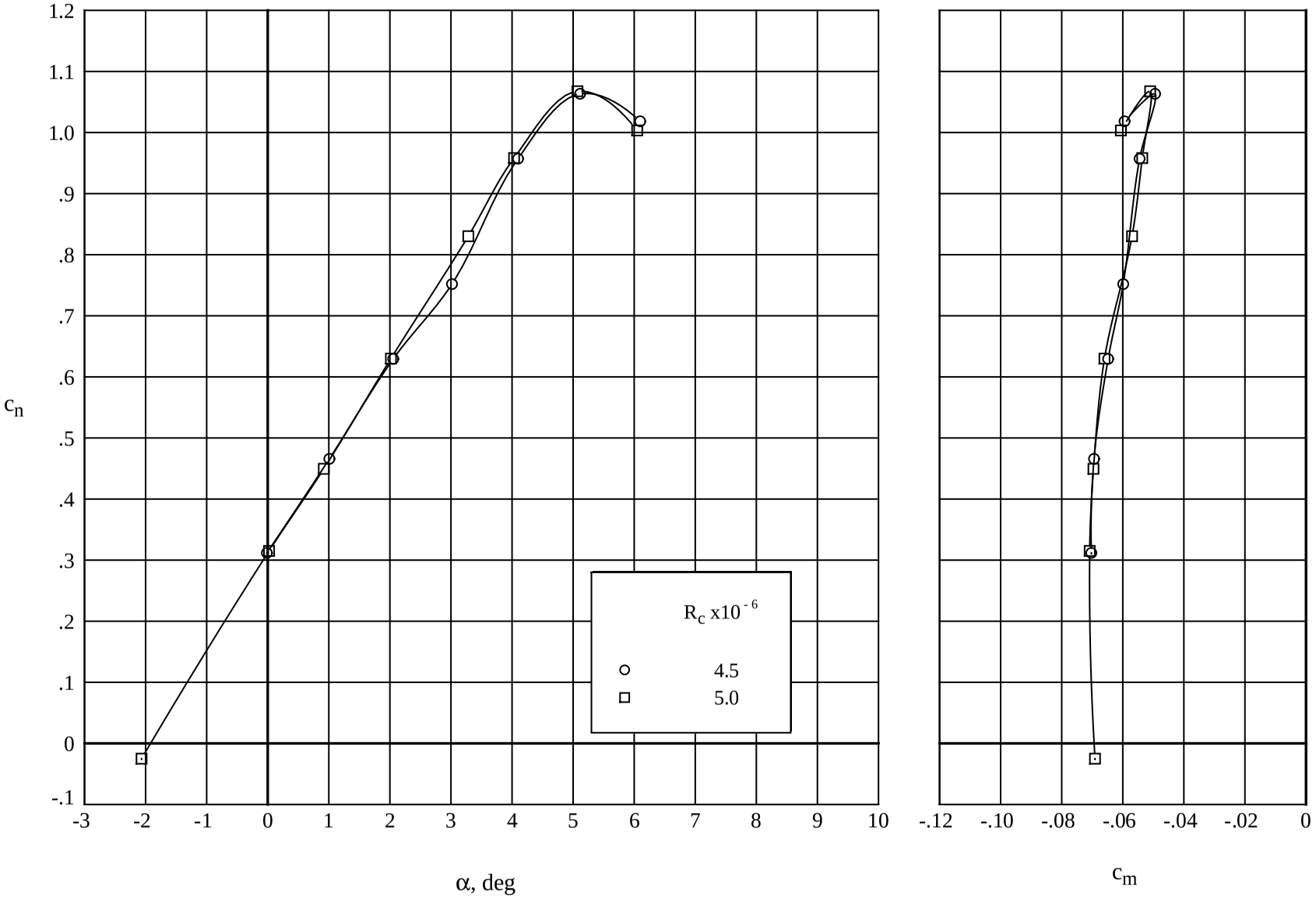

(i) Normal-force and pitching-moment coefficients. M_∞ = 0.670.

Figure 14. Continued.

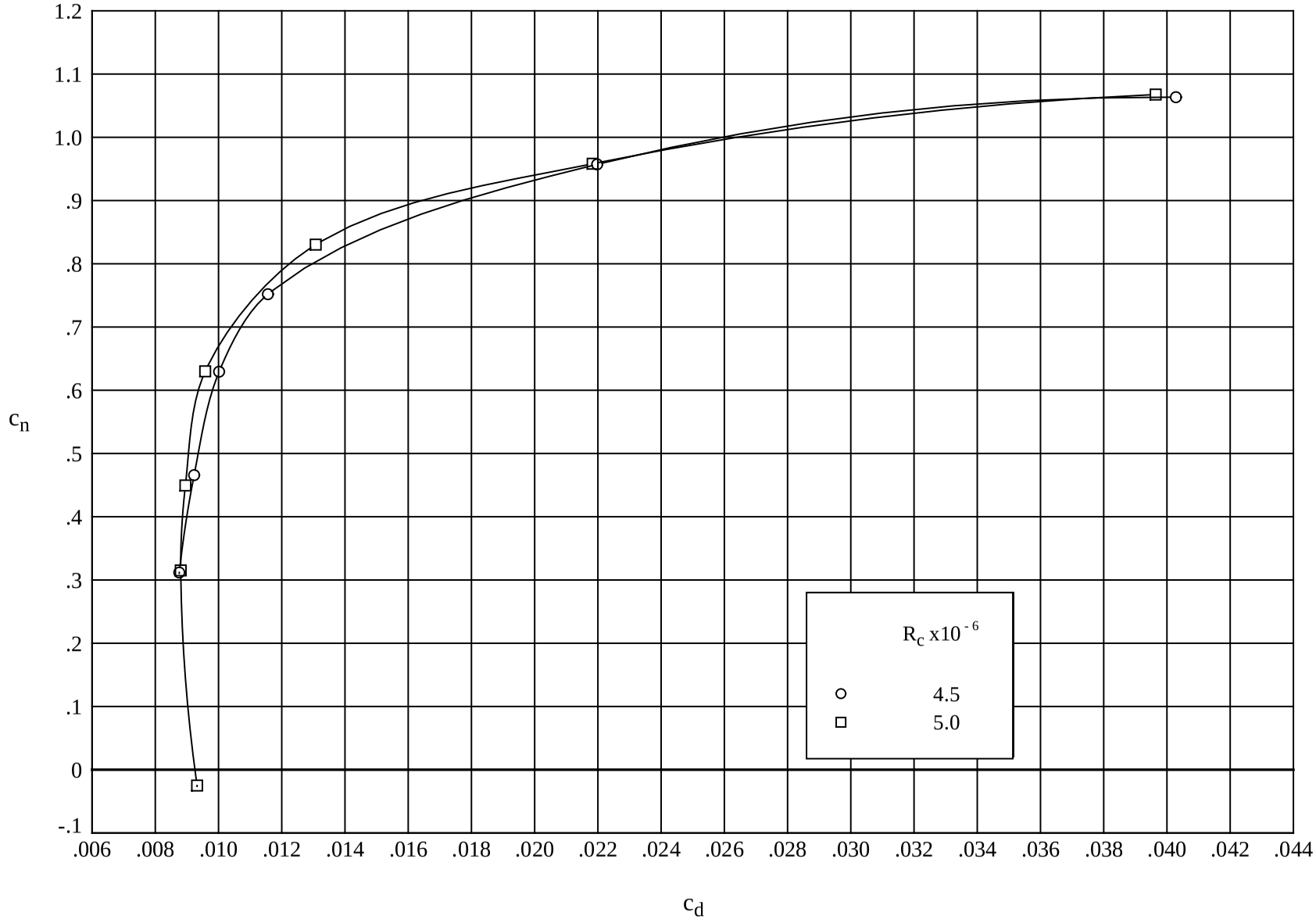

(j) Drag coefficient. M_∞ = 0.670.

Figure 14. Continued.

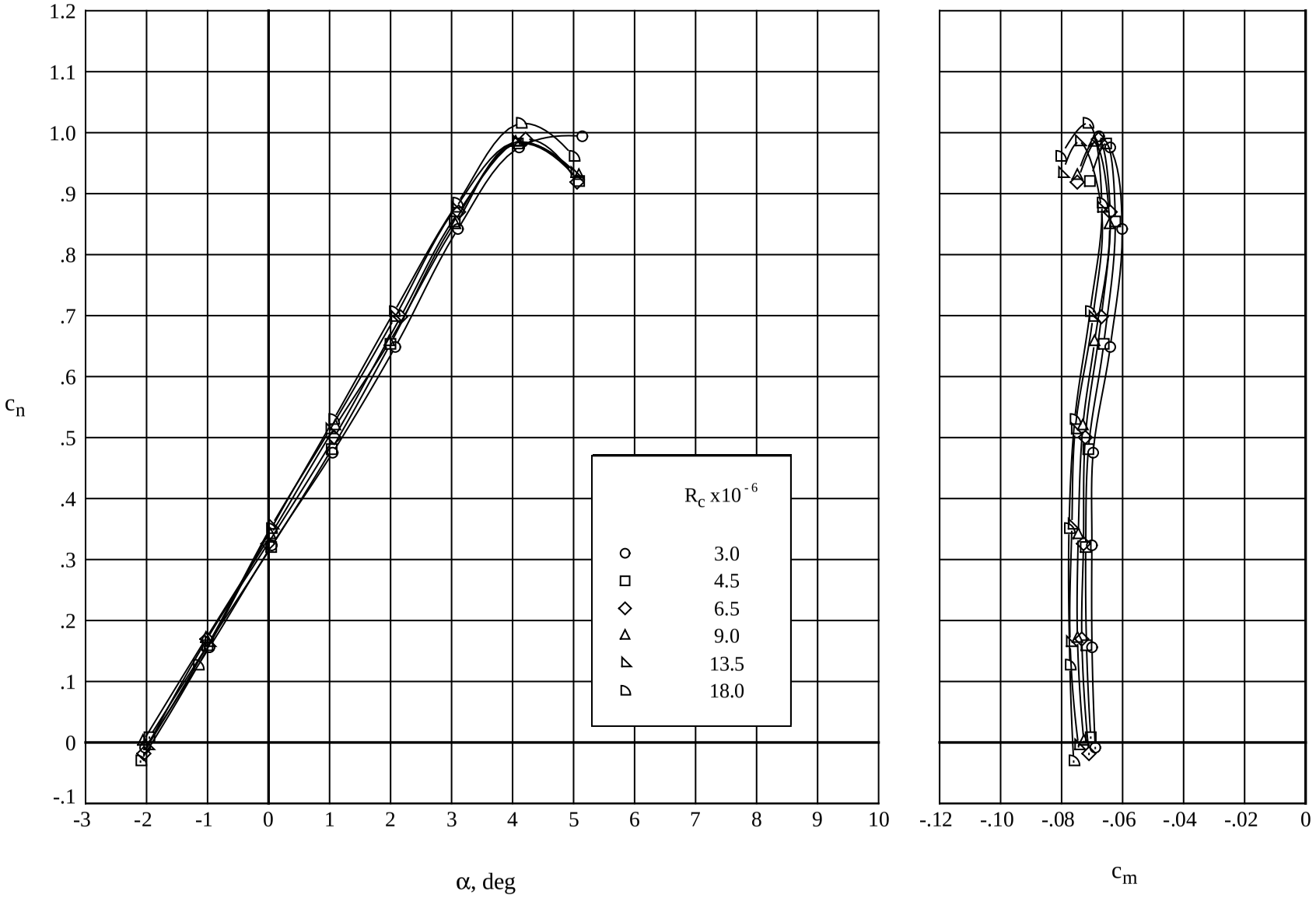

(k) Normal-force and pitching-moment coefficients. $M_\infty = 0.700$.

Figure 14. Continued.

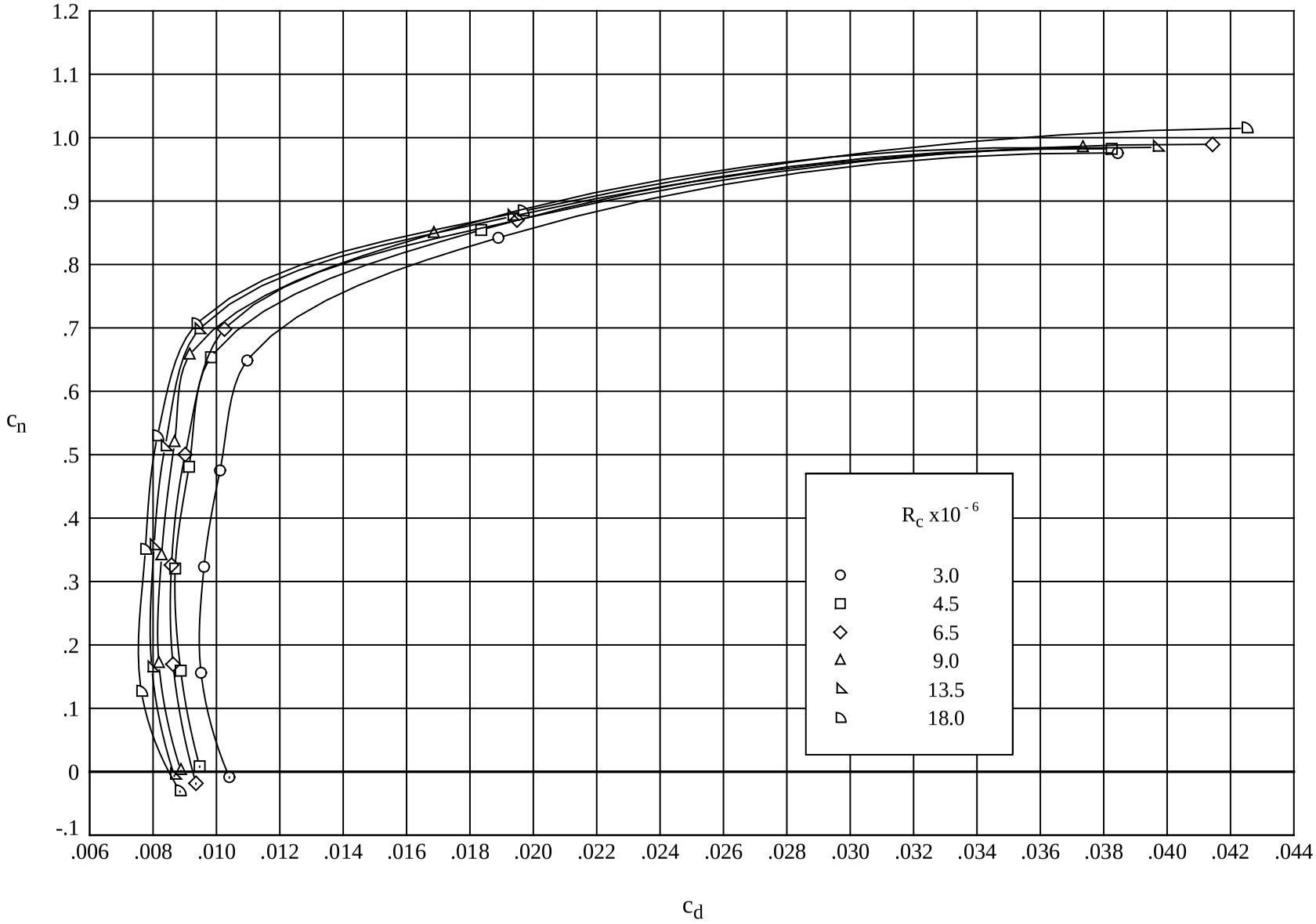

(l) Drag coefficient. M_∞ = 0.700.

Figure 14. Continued.

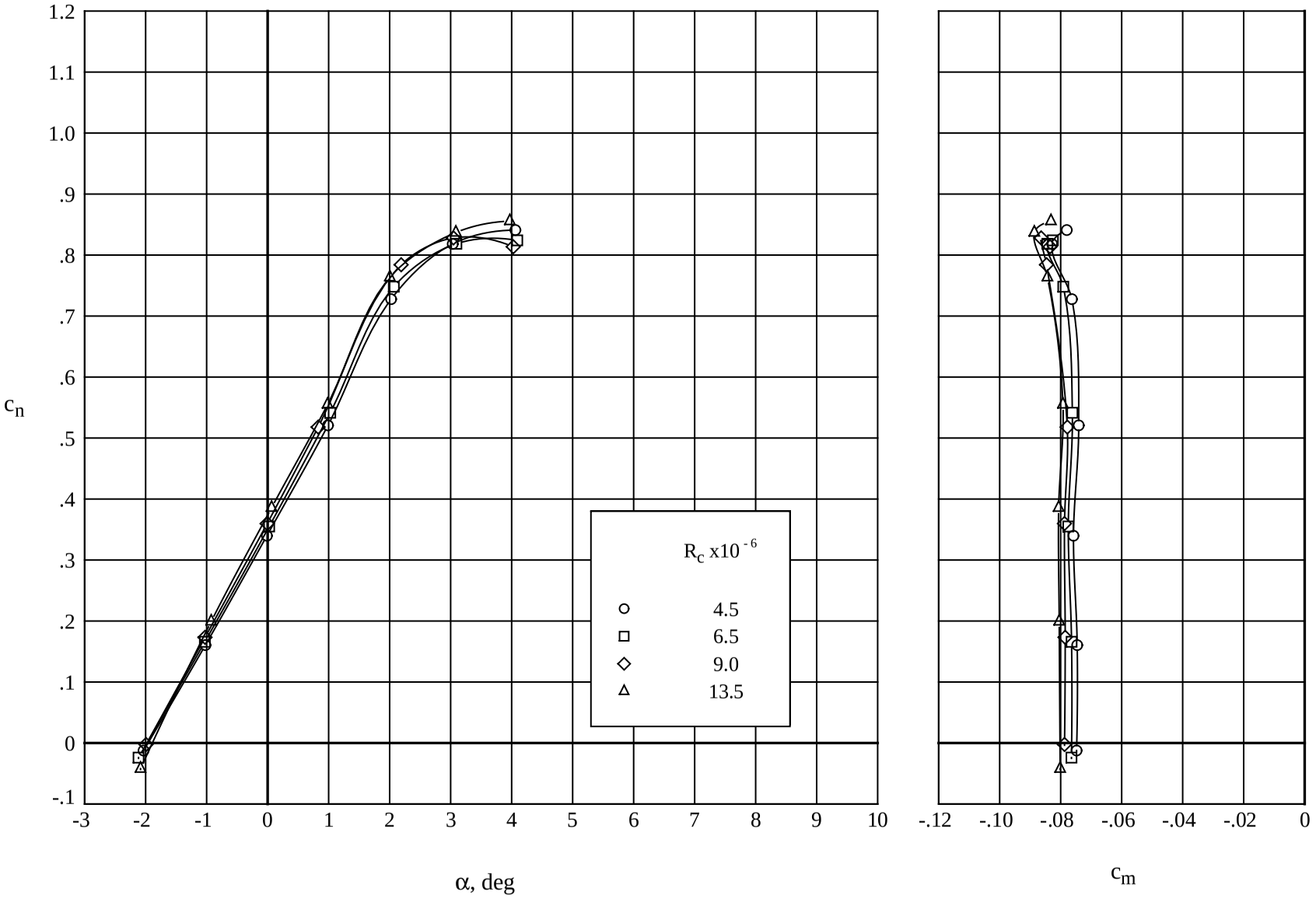

(m) Normal-force and pitching-moment coefficients. $M_\infty = 0.735$.

Figure 14. Continued.

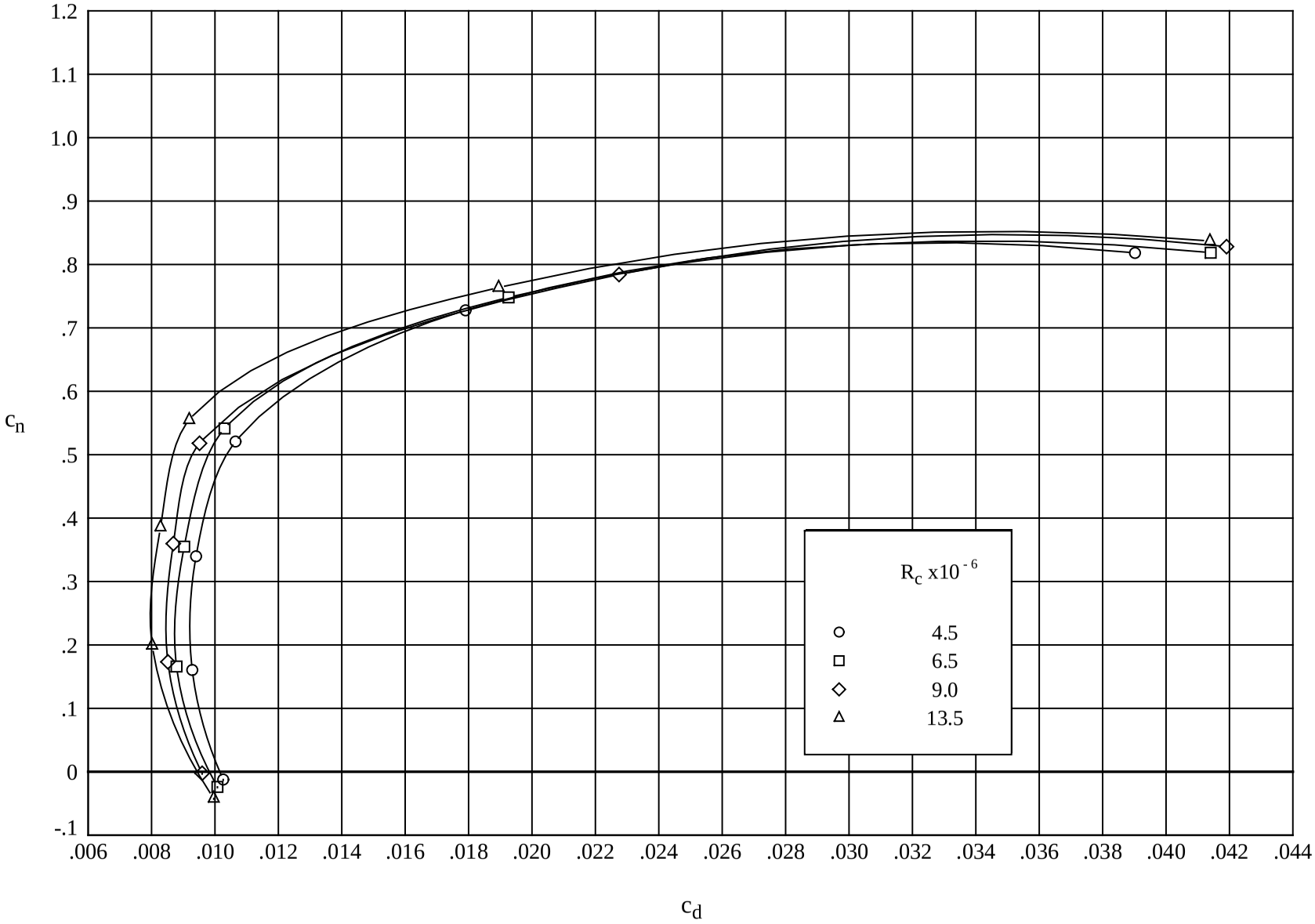

(n) Drag coefficient. $M_\infty = 0.735$.

Figure 14. Continued.

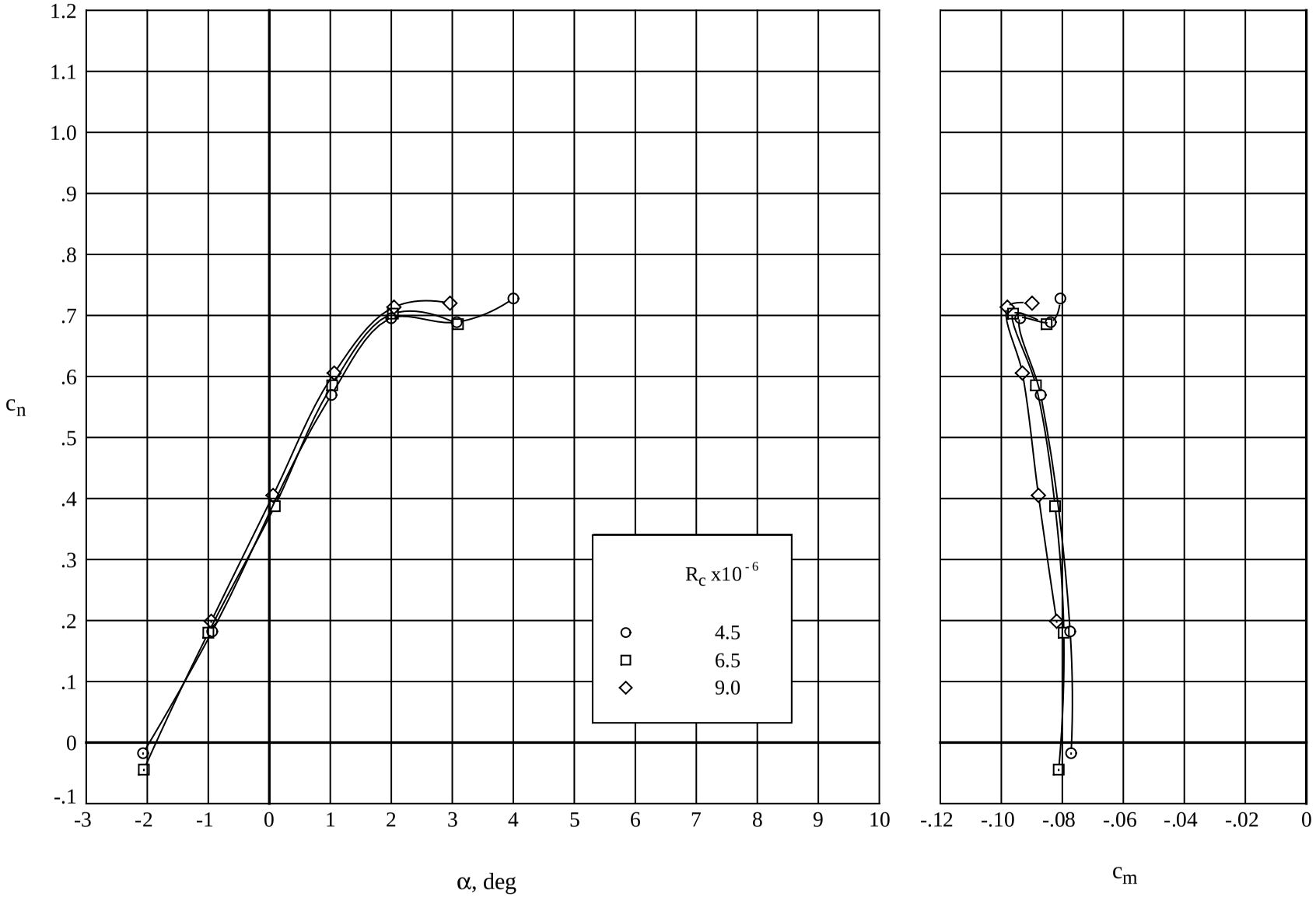

(o) Normal-force and pitching-moment coefficients. M_∞ = 0.760.

Figure 14. Continued.

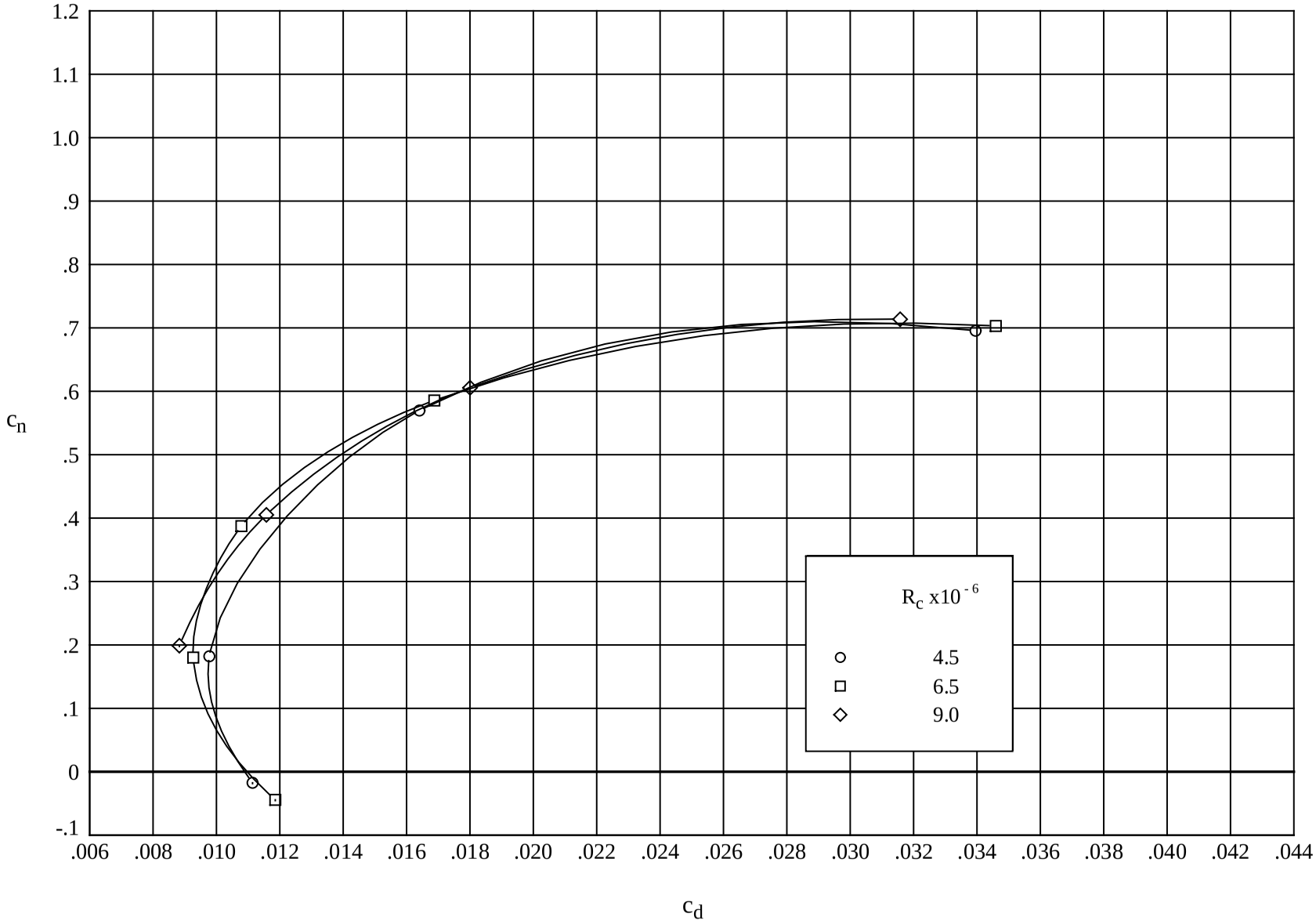

(p) Drag coefficient. M_∞ = 0.760.

Figure 14. Concluded.

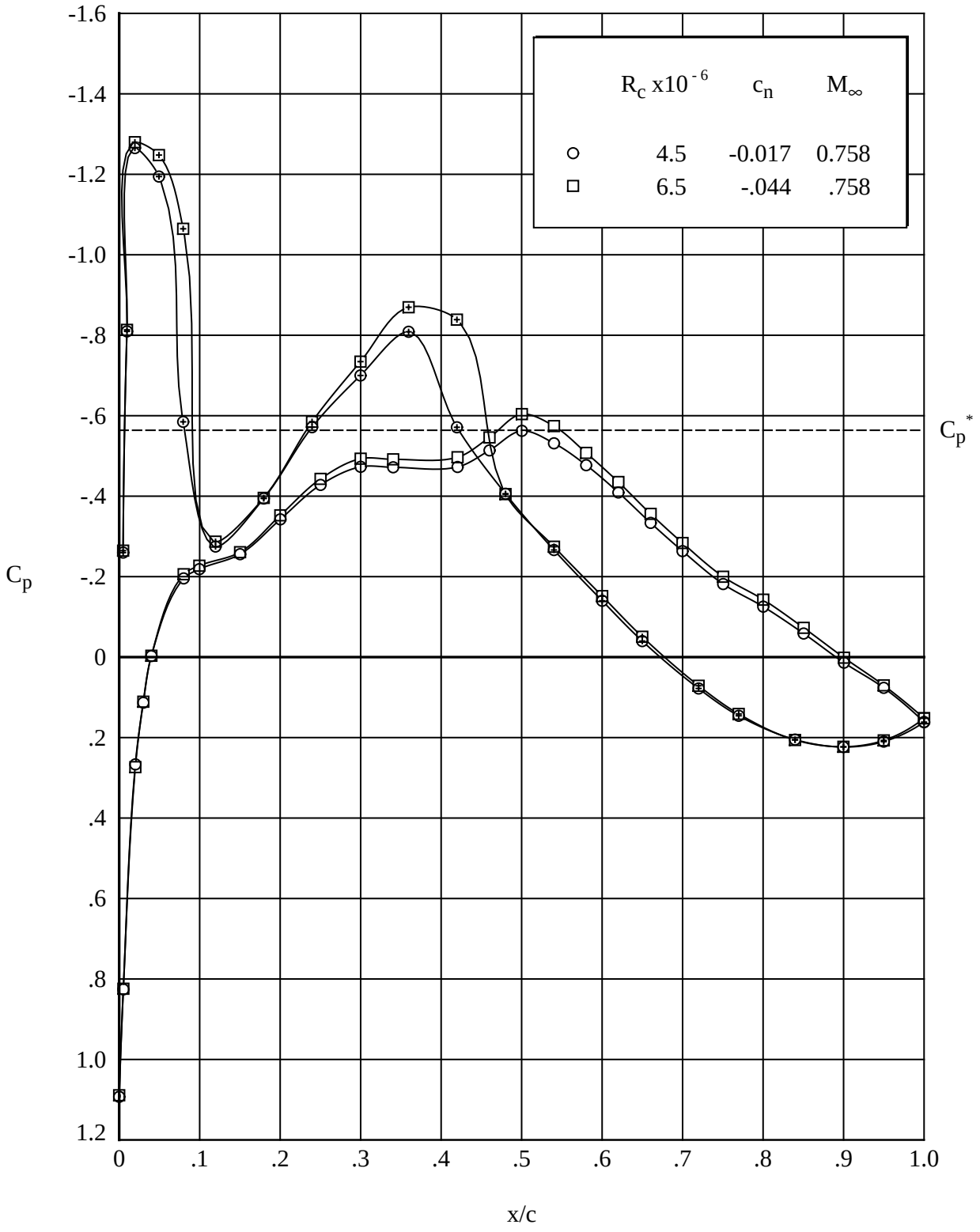

(a) $\alpha = -2.1°$; $c_n \approx 0$.

Figure 15. Effect of Reynolds number on chordwise pressure distributions for modified airfoil. Open symbols denote upper surface; "+" within symbol denotes lower surface. $M_\infty = 0.760$.

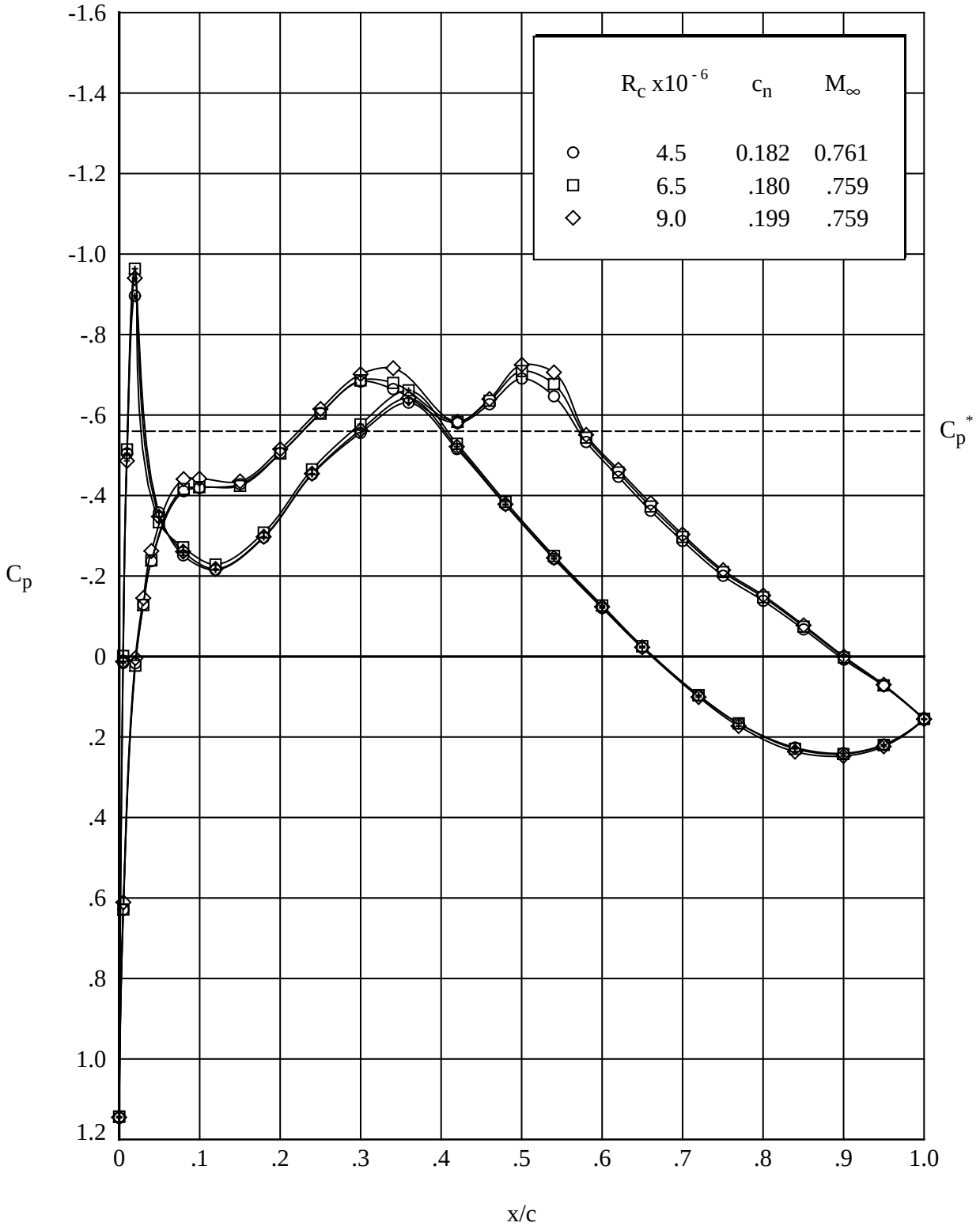

(b) $\alpha = -1.0°$; $c_n \approx 0.2$.

Figure 15. Continued.

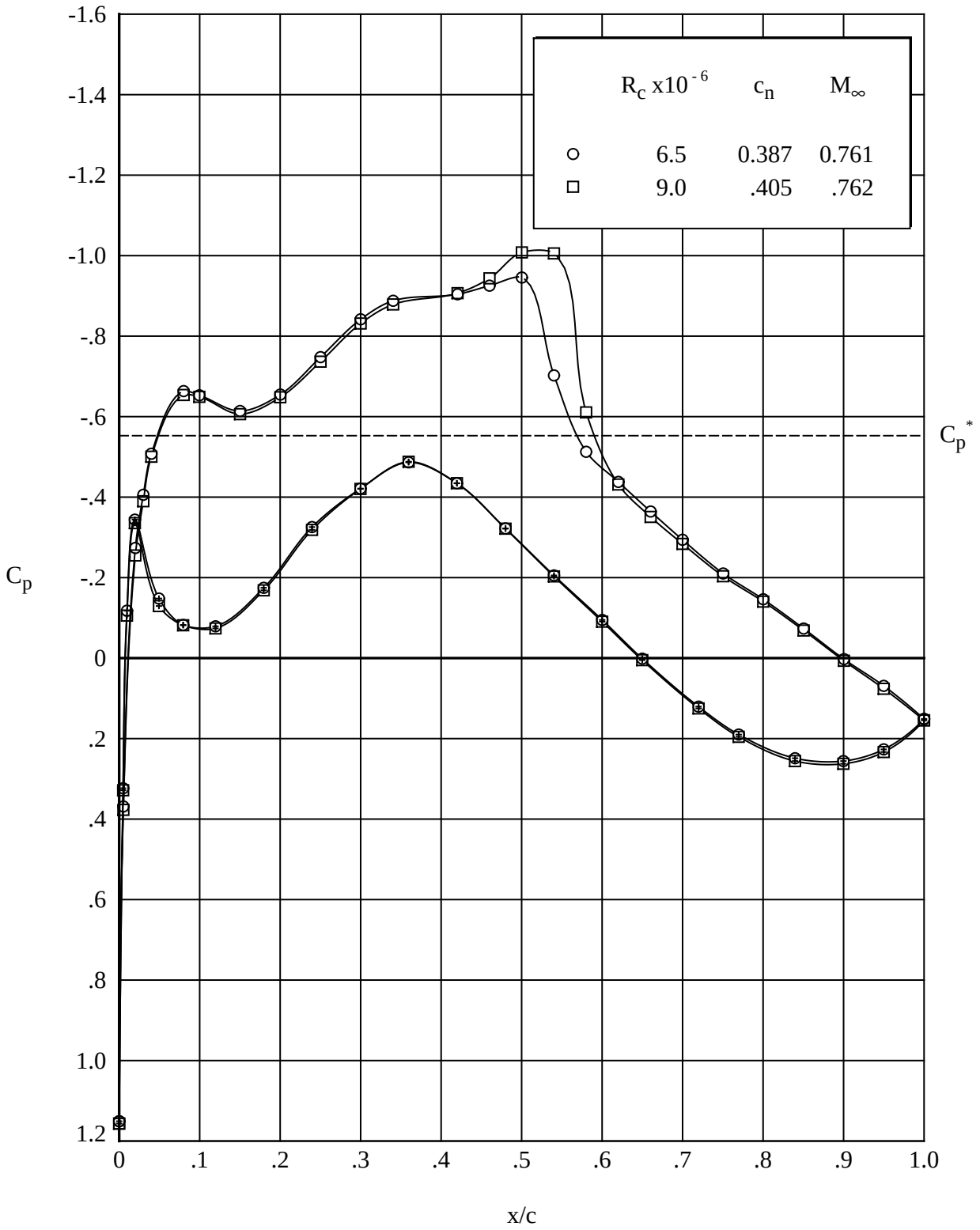

(c) $\alpha = 0.1°$; $c_n \approx 0.4$.

Figure 15. Concluded.

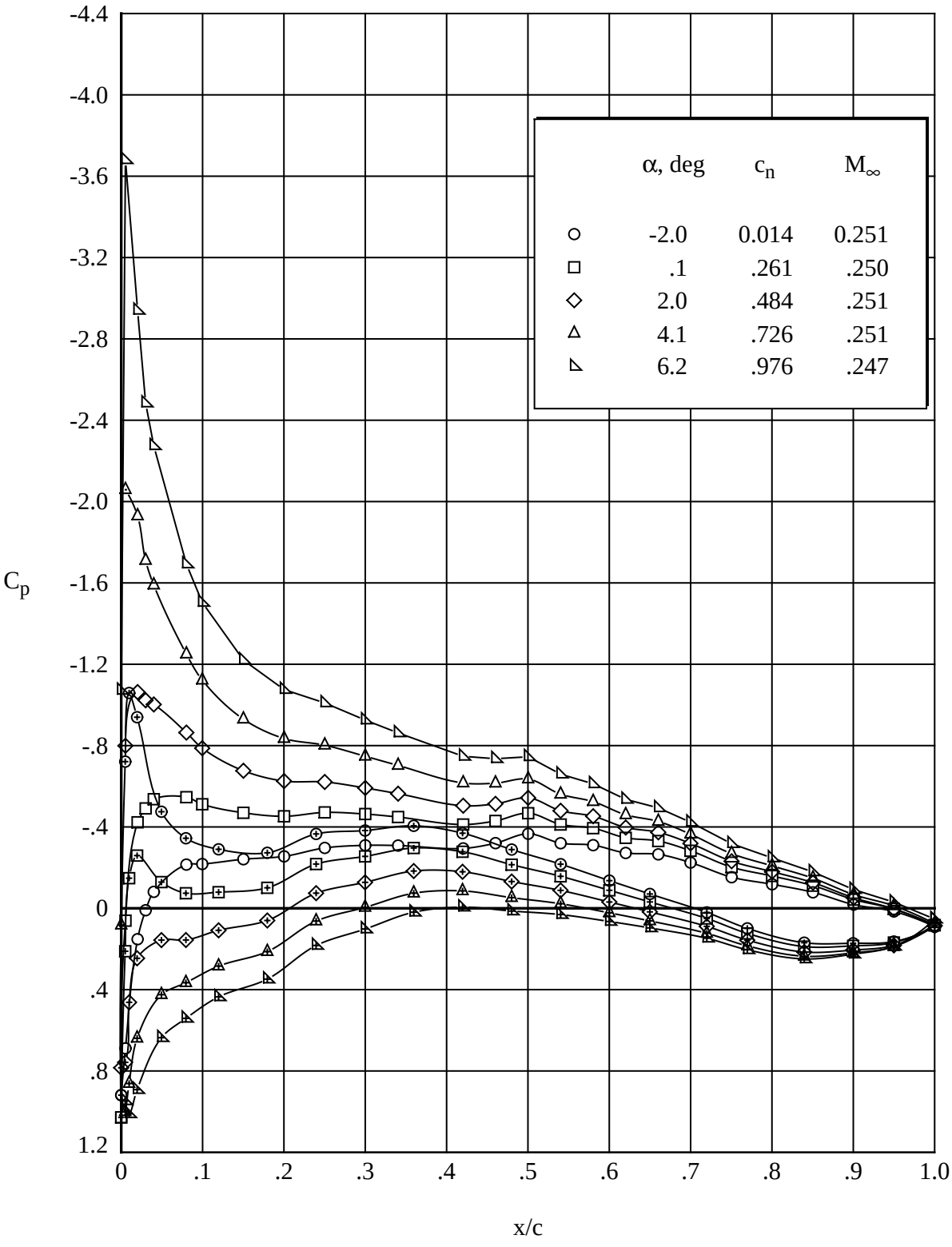

(a) $R_c = 4.5 \times 10^6$.

Figure 16. Effect of angle of attack on chordwise pressure distributions for modified airfoil. Open symbols denote upper surface; "+" within symbol denotes lower surface. $M_\infty = 0.250$.

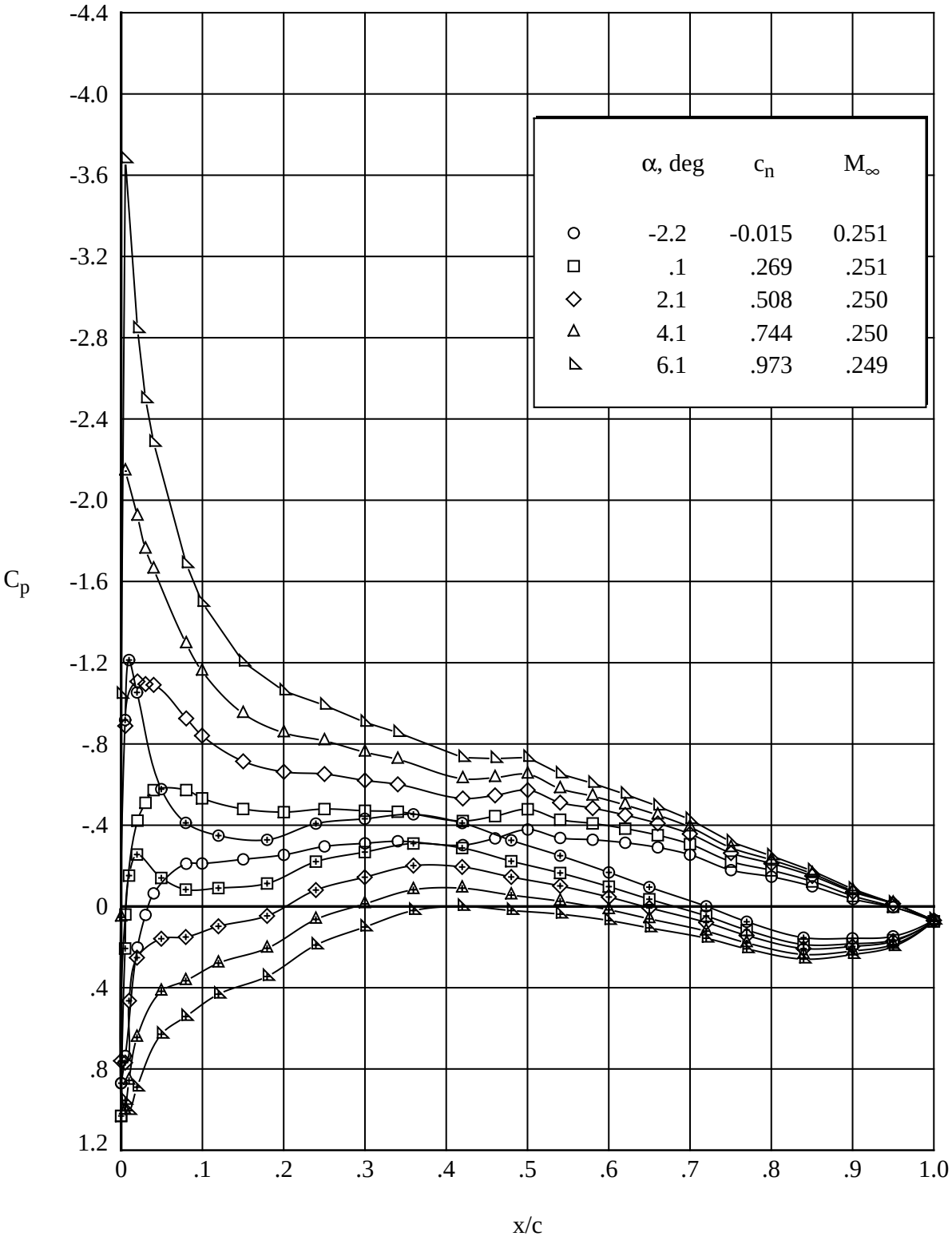

(b) $R_c = 9.0 \times 10^6$.

Figure 16. Concluded.

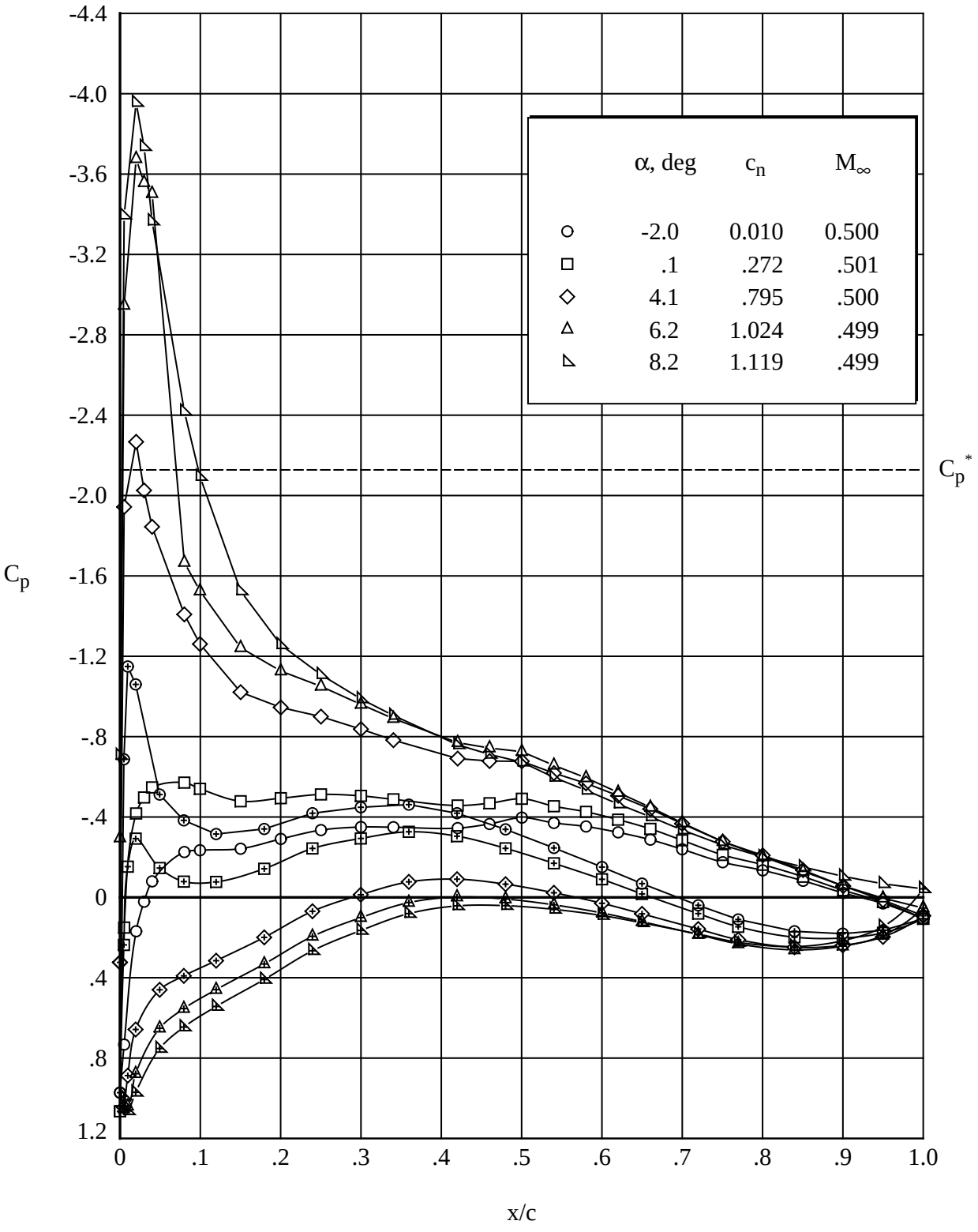

(a) $R_c = 4.5 \times 10^6$.

Figure 17. Effect of angle of attack on chordwise pressure distributions for modified airfoil. Open symbols denote upper surface; "+" within symbol denotes lower surface. $M_\infty = 0.500$.

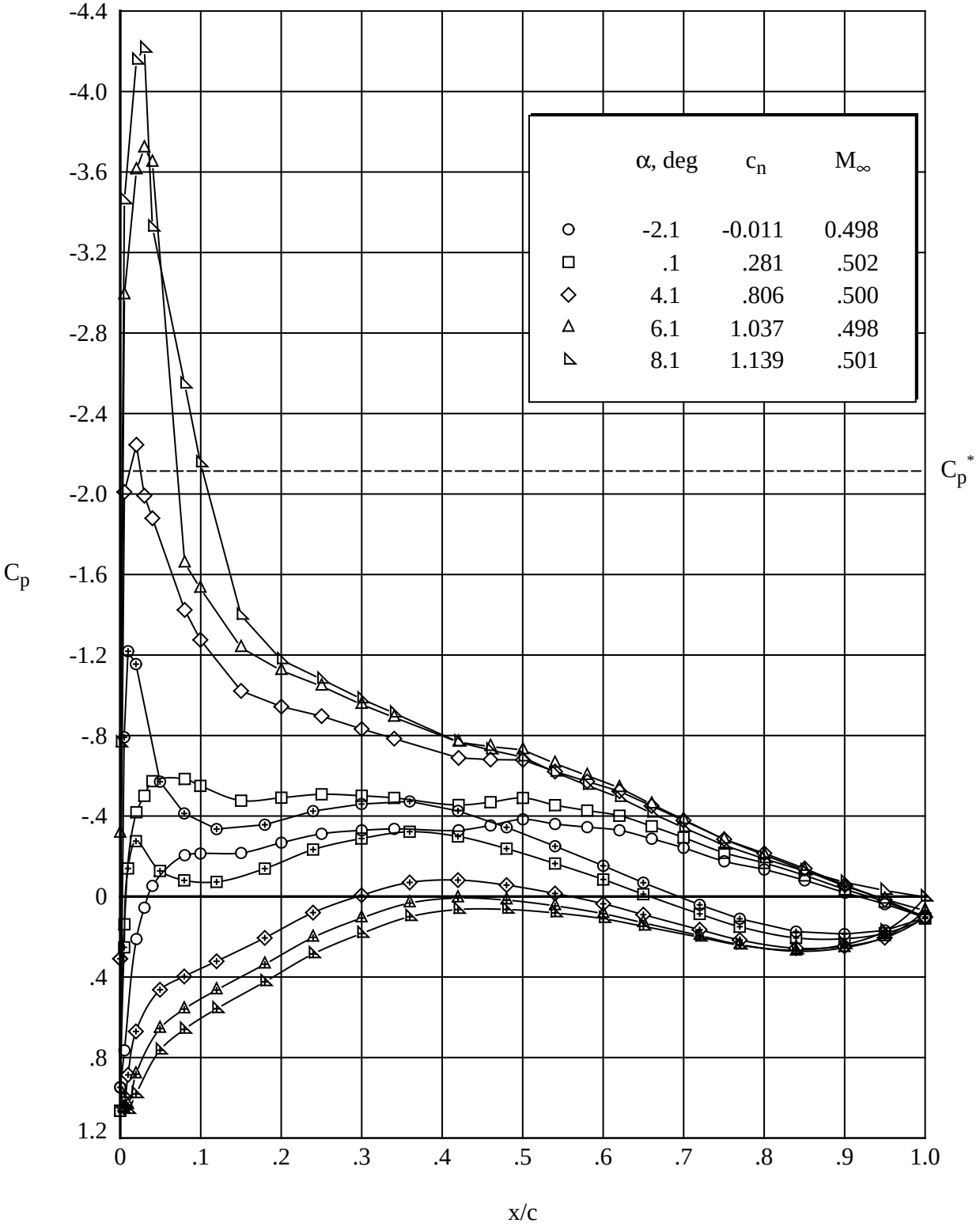

(b) $R_c = 9.0 \times 10^6$.

Figure 17. Concluded.

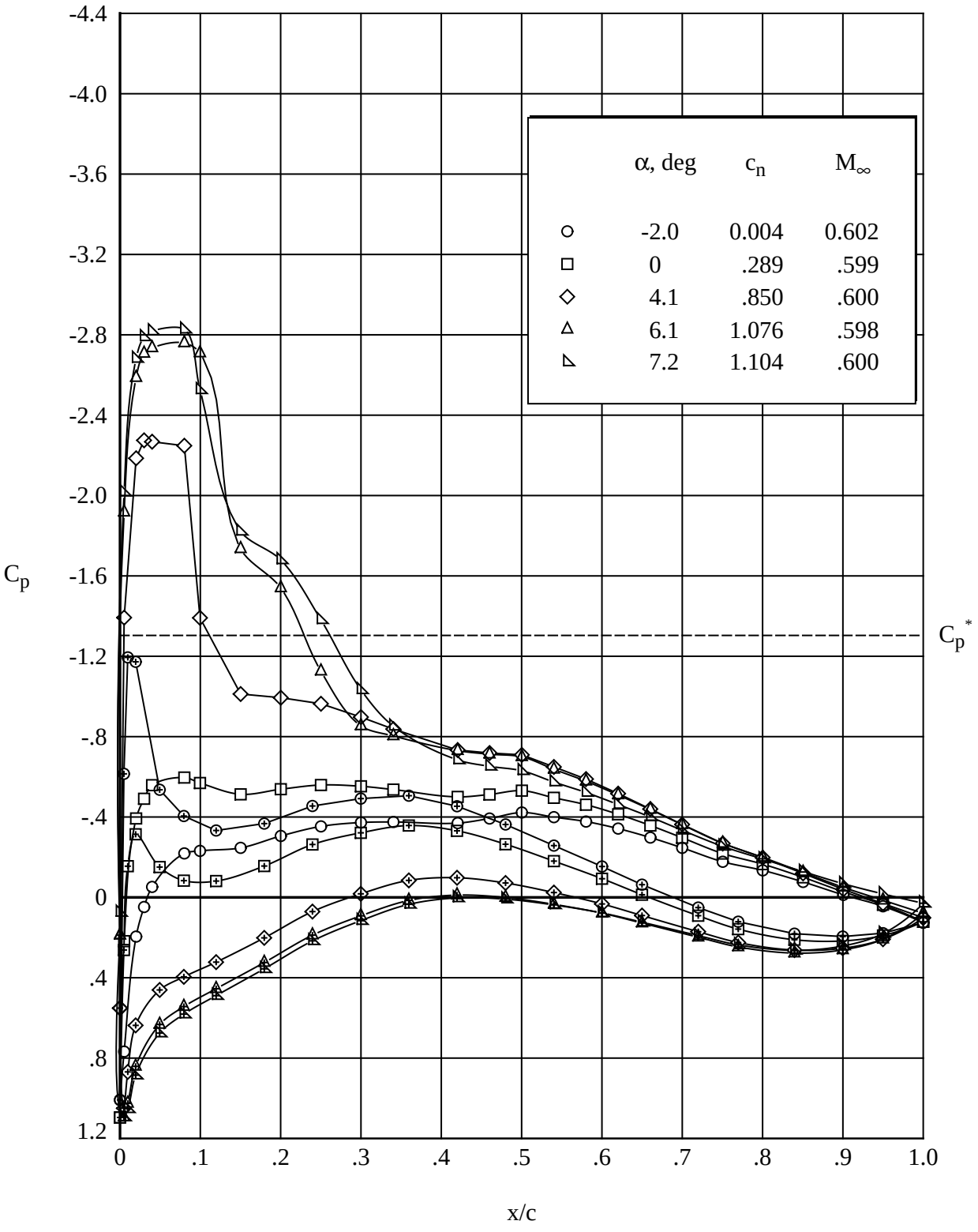

(a) $R_c = 4.5 \times 10^6$.

Figure 18. Effect of angle of attack on chordwise pressure distributions for modified airfoil. Open symbols denote upper surface; "+" within symbol denotes lower surface. $M_\infty = 0.600$.

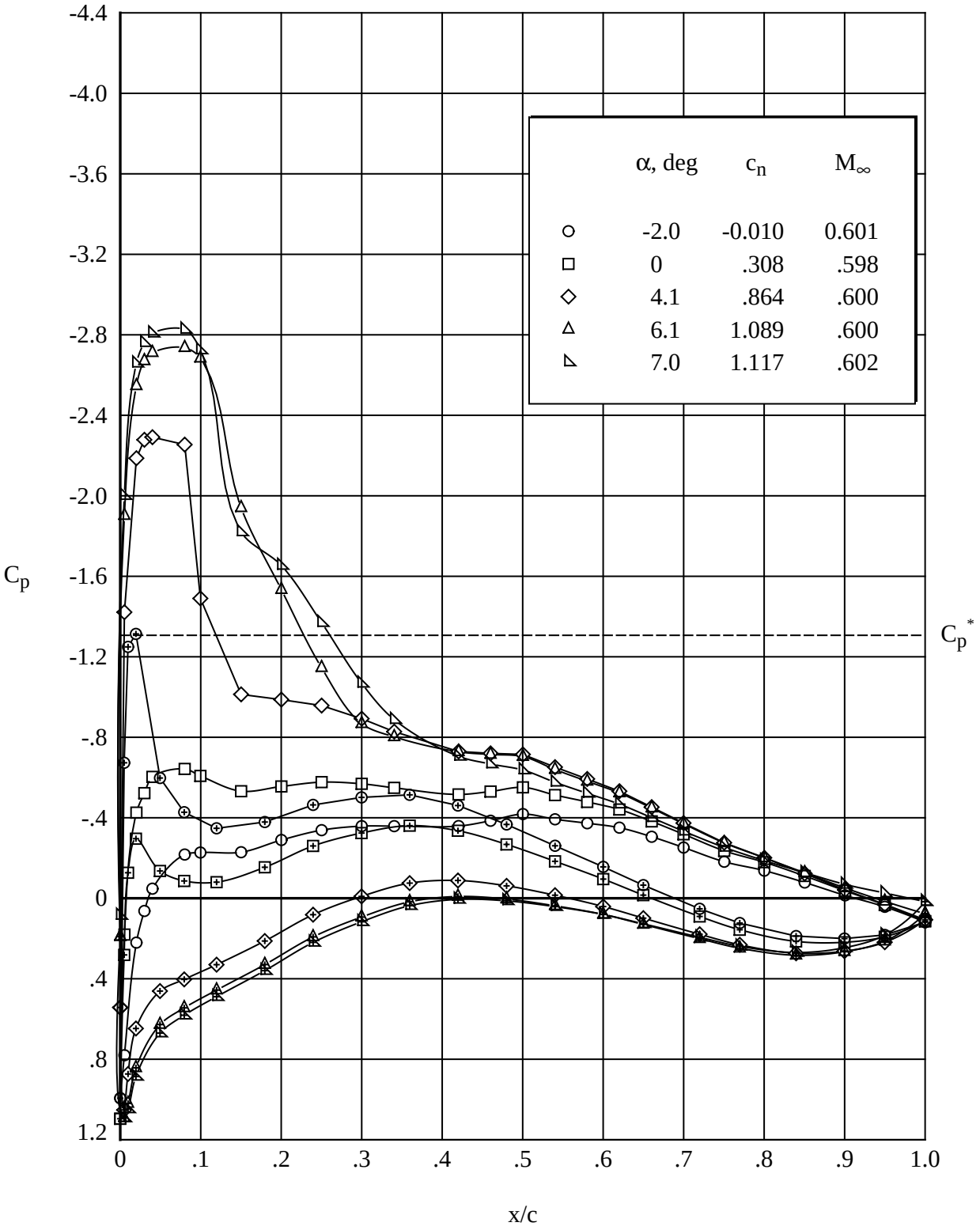

(b) $R_c = 9.0 \times 10^6$.

Figure 18. Concluded.

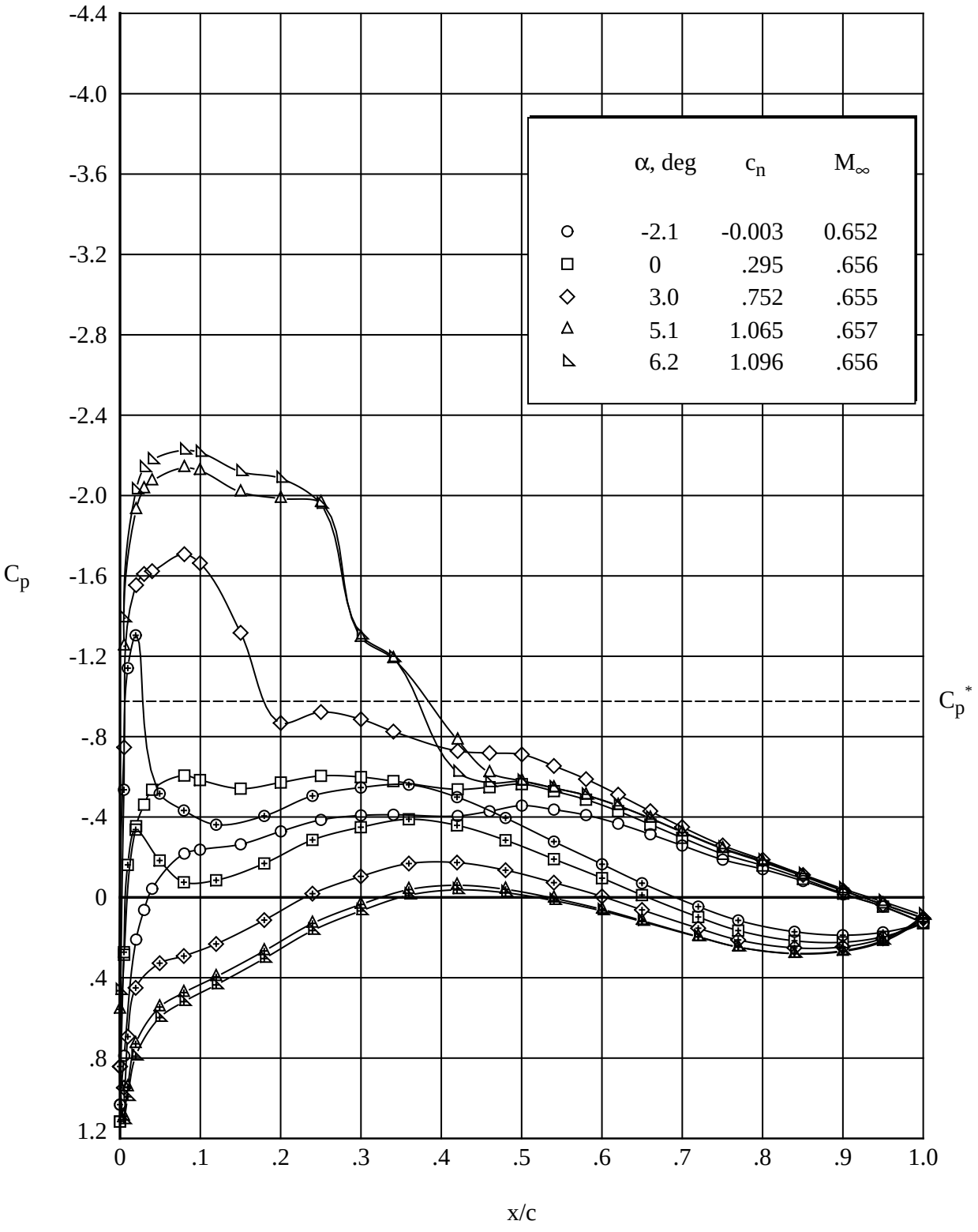

(a) $R_c = 3.0 \times 10^6$.

Figure 19. Effect of angle of attack on chordwise pressure distributions for modified airfoil. Open symbols denote upper surface; "+" within symbol denotes lower surface. $M_\infty = 0.655$.

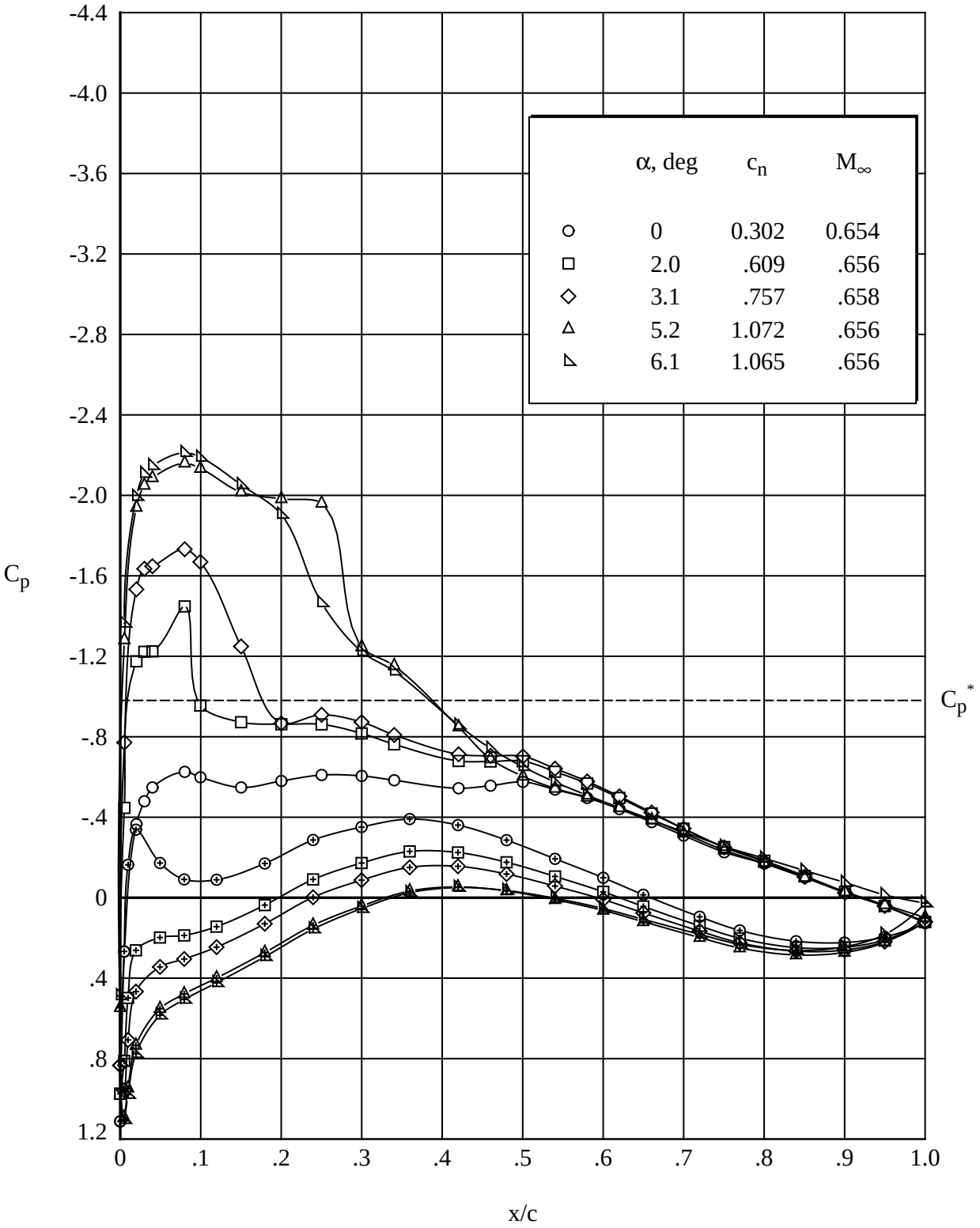

(b) $R_c = 4.5 \times 10^6$.

Figure 19. Continued.

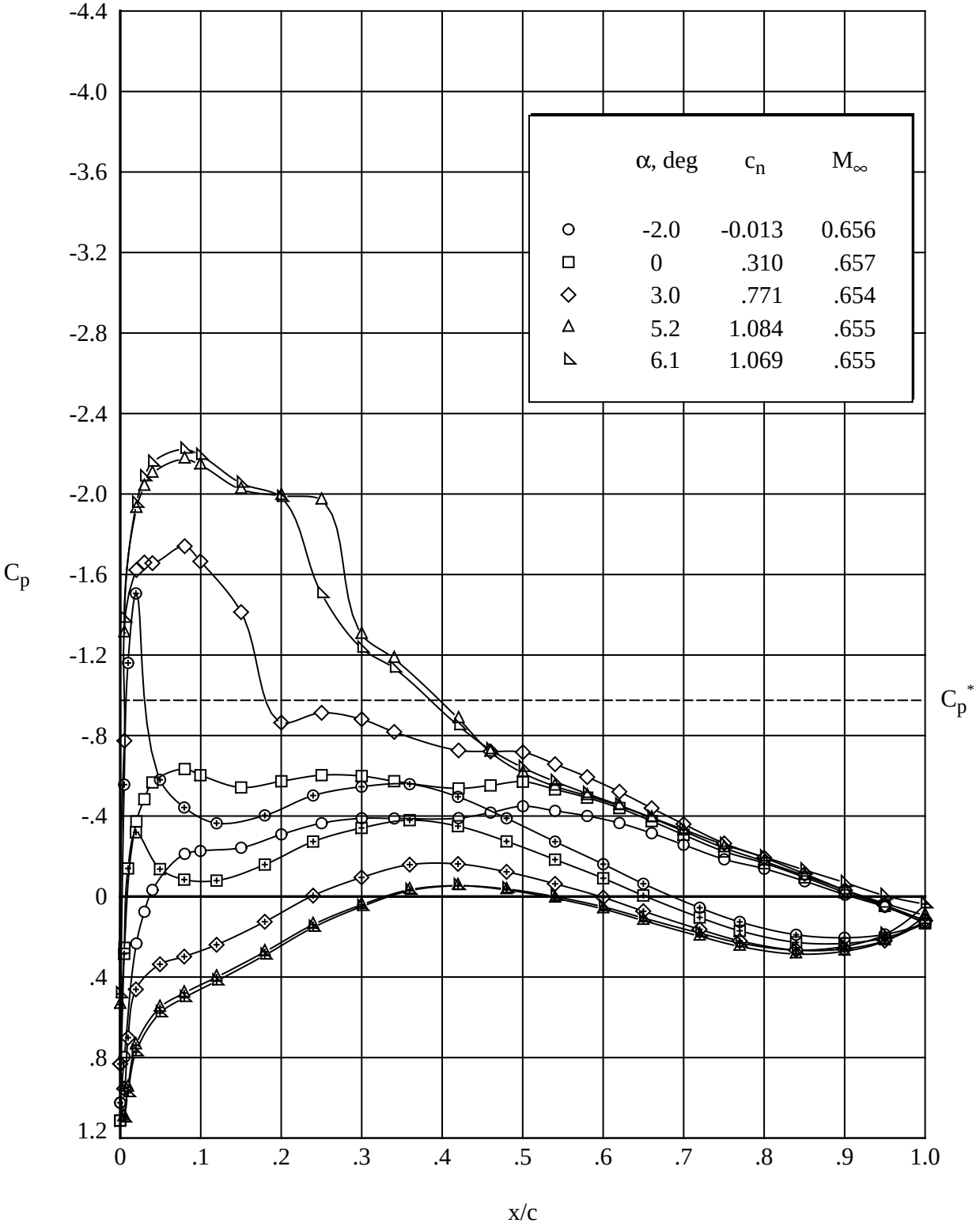

(c) $R_c = 6.5 \times 10^6$.

Figure 19. Continued.

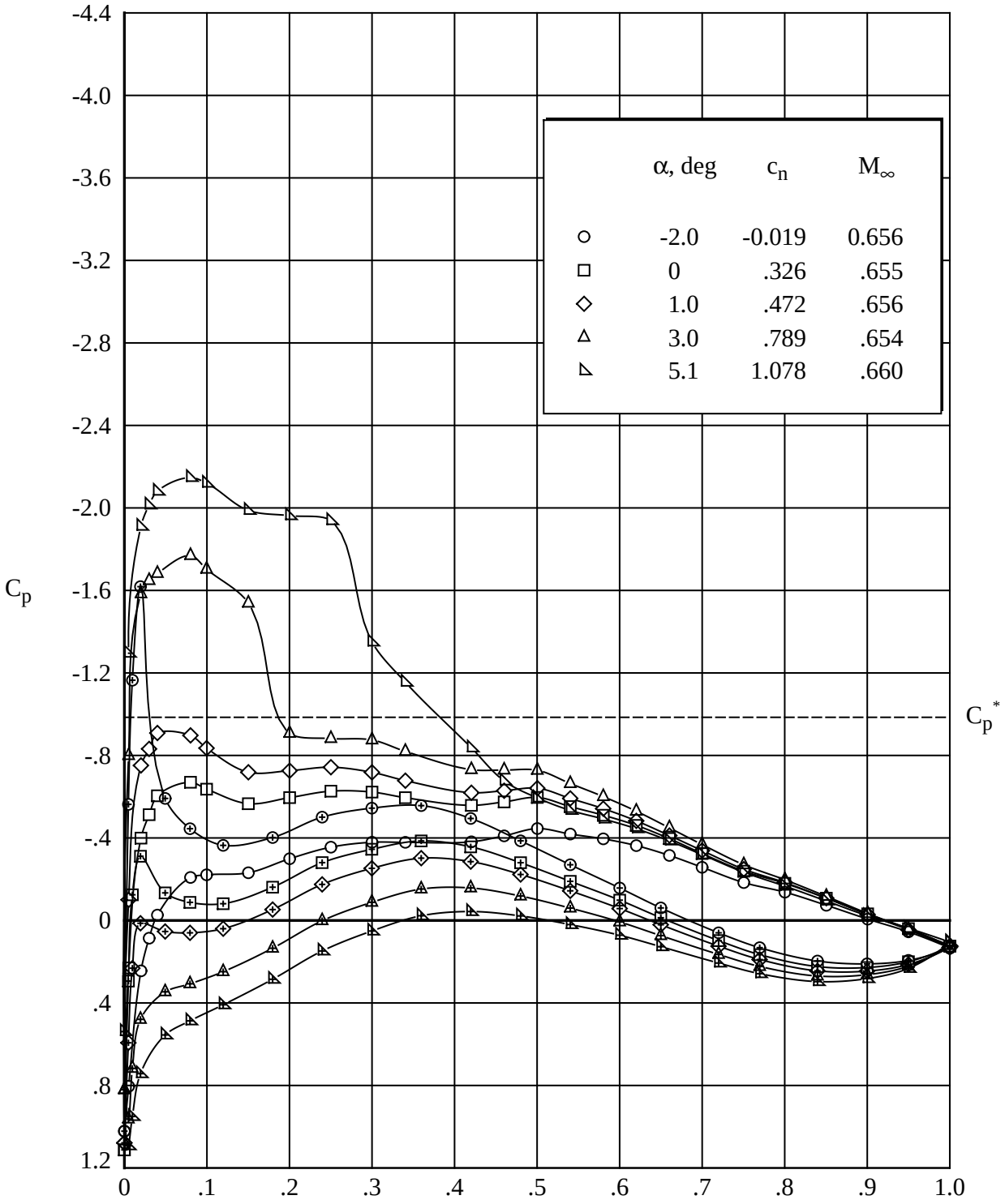

(d) $R_c = 9.0 \times 10^6$.

Figure 19. Concluded.

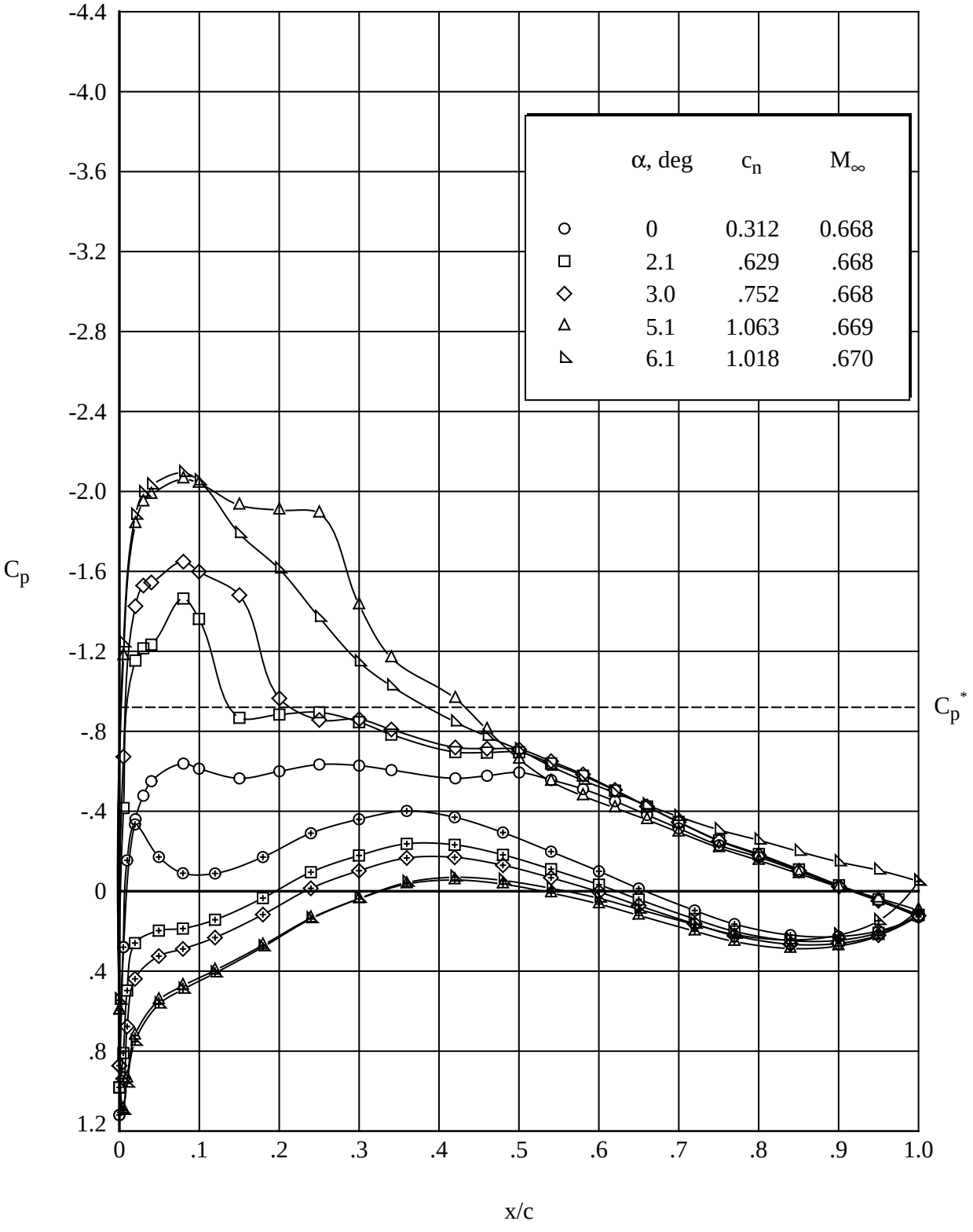

(a) $R_c = 4.5 \times 10^6$.

Figure 20. Effect of angle of attack on chordwise pressure distributions for modified airfoil. Open symbols denote upper surface; "+" within symbol denotes lower surface. $M_\infty = 0.670$.

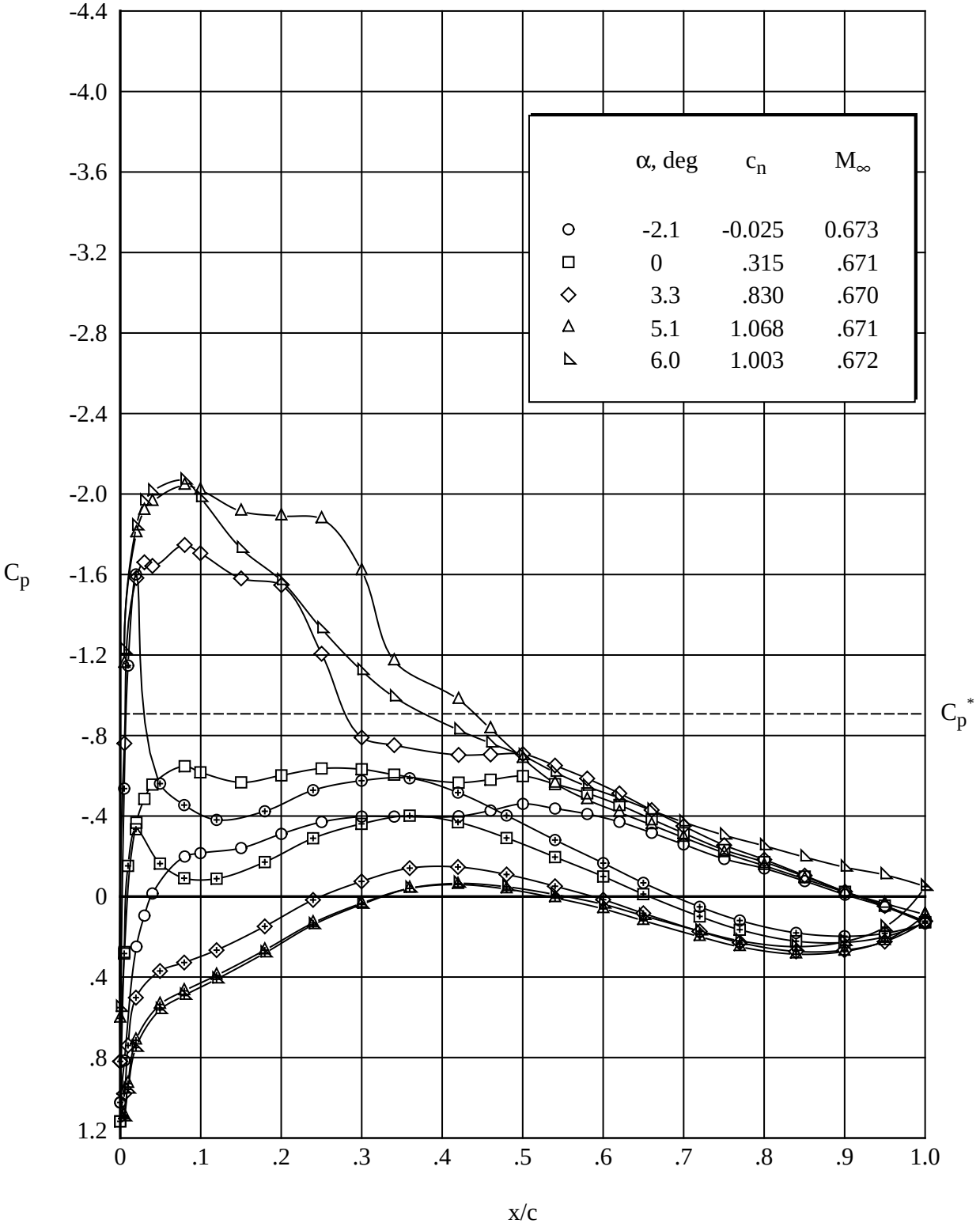

(b) $R_c = 5.0 \times 10^6$.

Figure 20. Concluded.

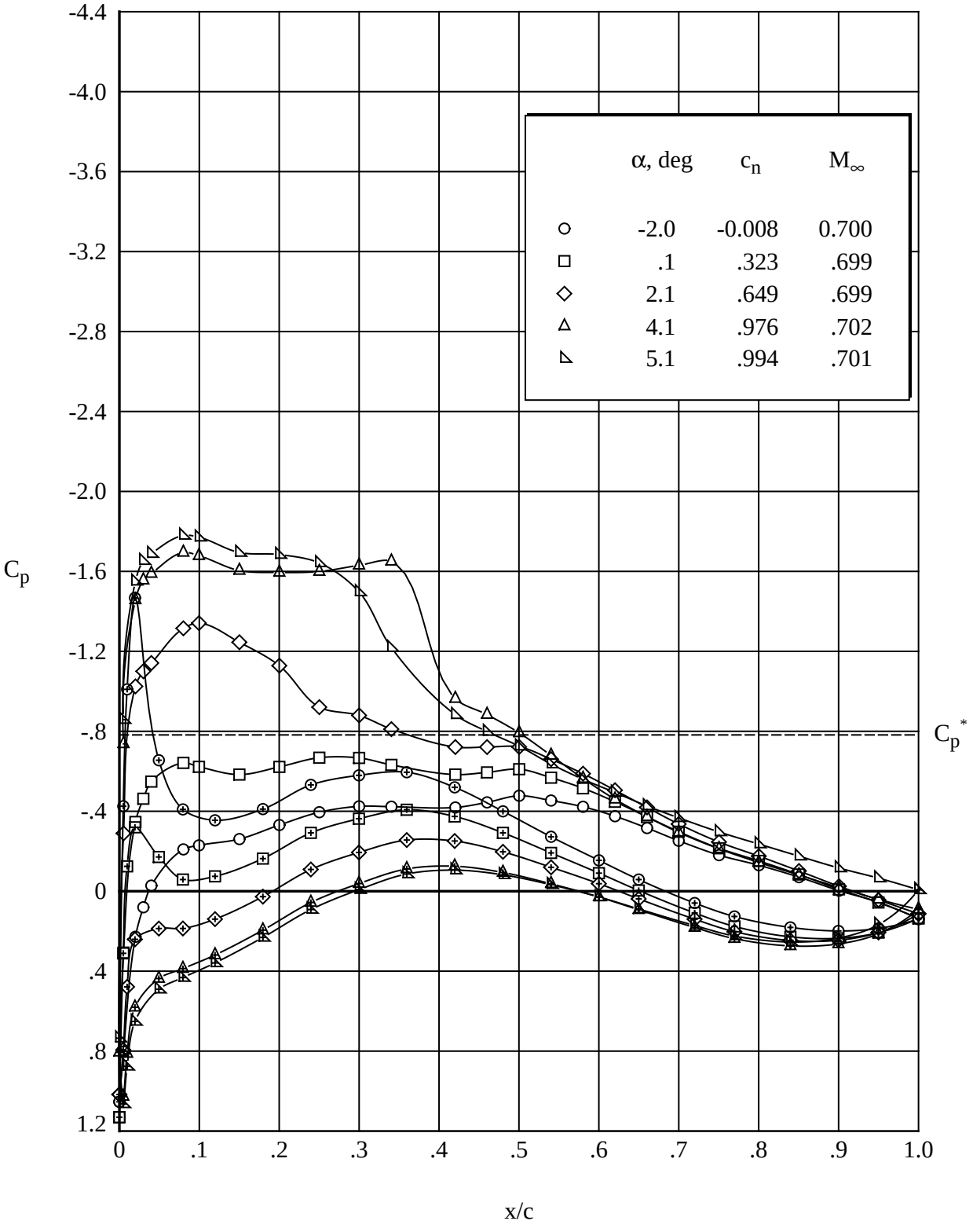

(a) $R_c = 3.0 \times 10^6$.

Figure 21. Effect of angle of attack on chordwise pressure distributions for modified airfoil. Open symbols denote upper surface; "+" within symbol denotes lower surface. $M_\infty = 0.700$.

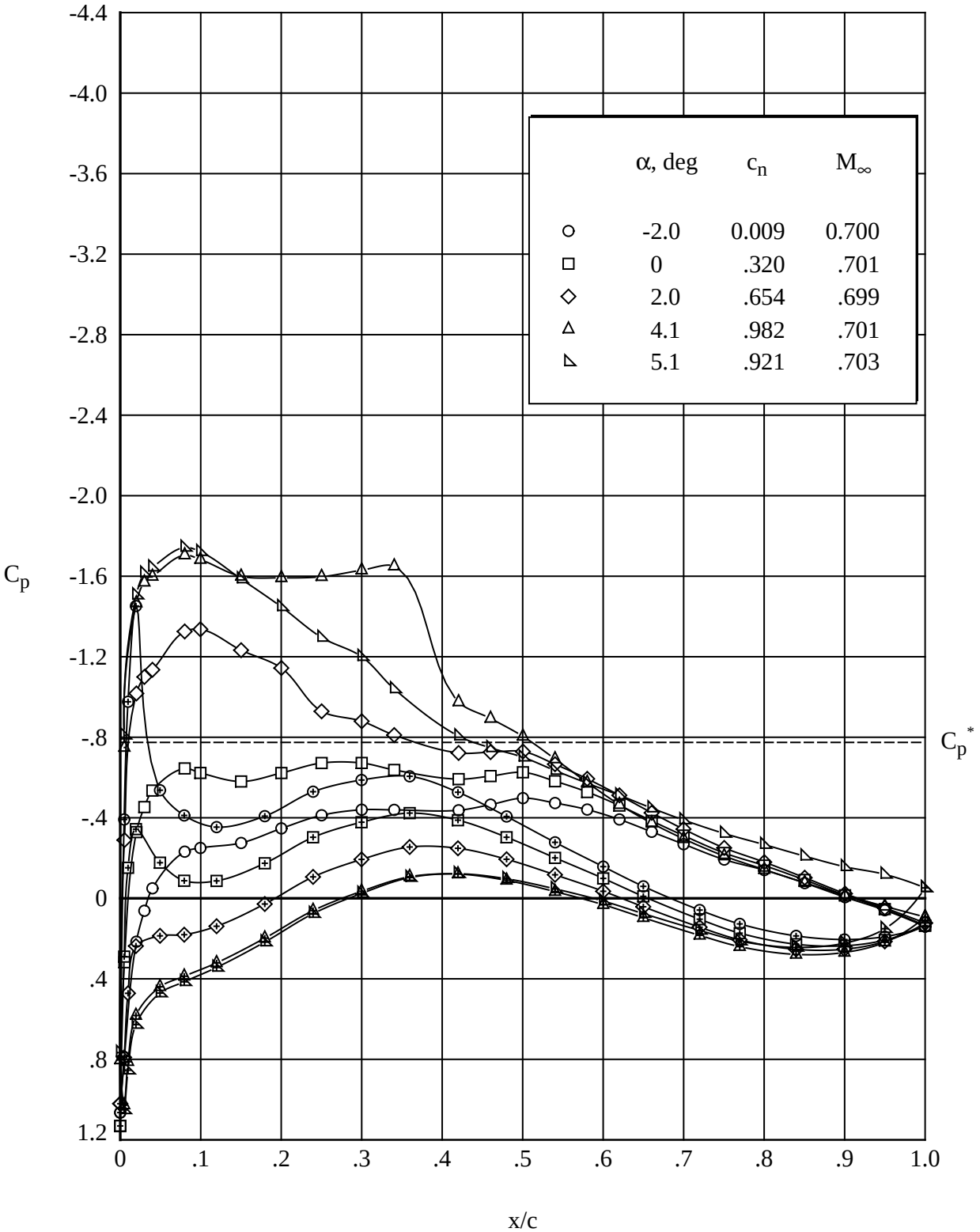

(b) $R_c = 4.5 \times 10^6$.

Figure 21. Continued.

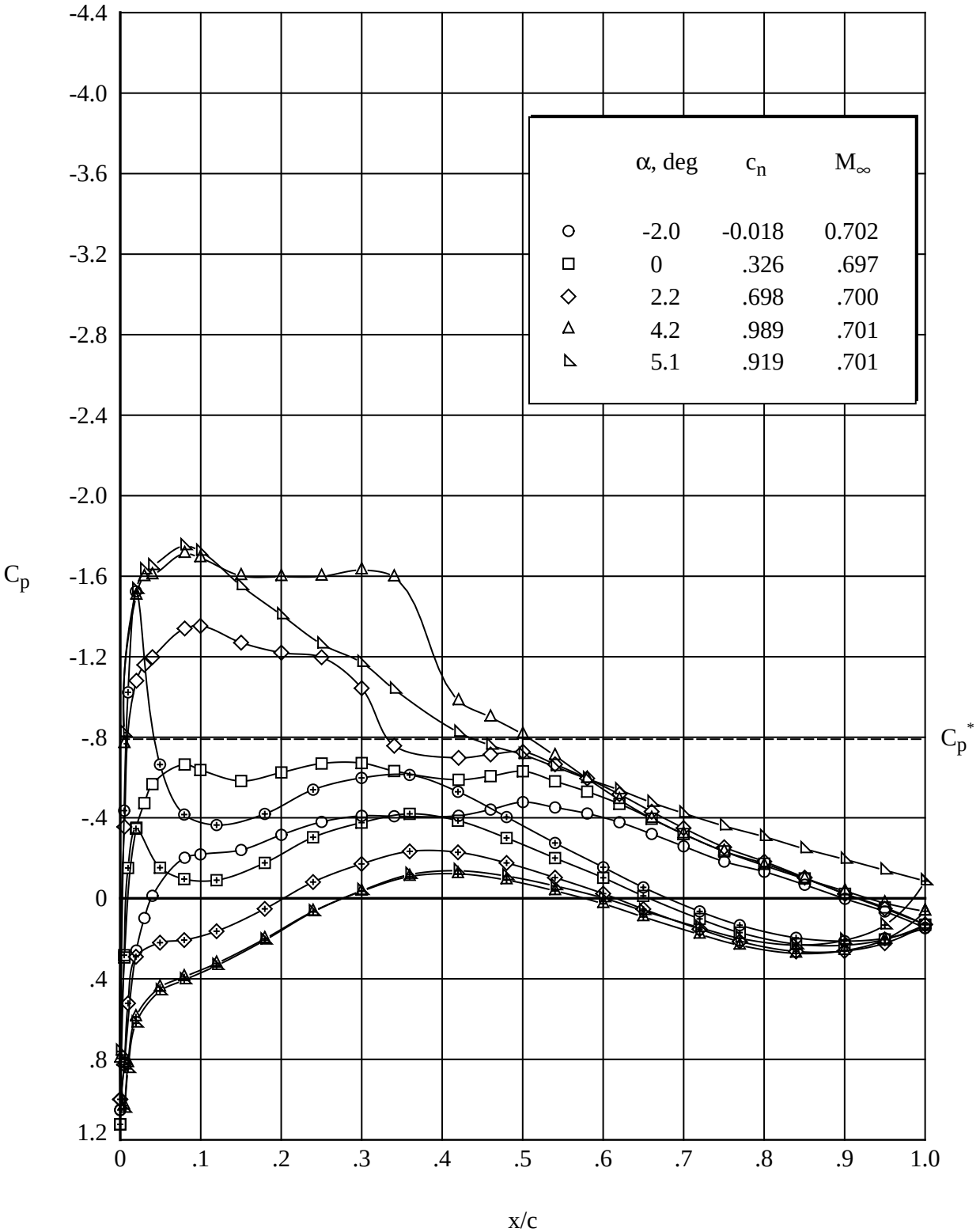

(c) $R_c = 6.5 \times 10^6$.

Figure 21. Continued.

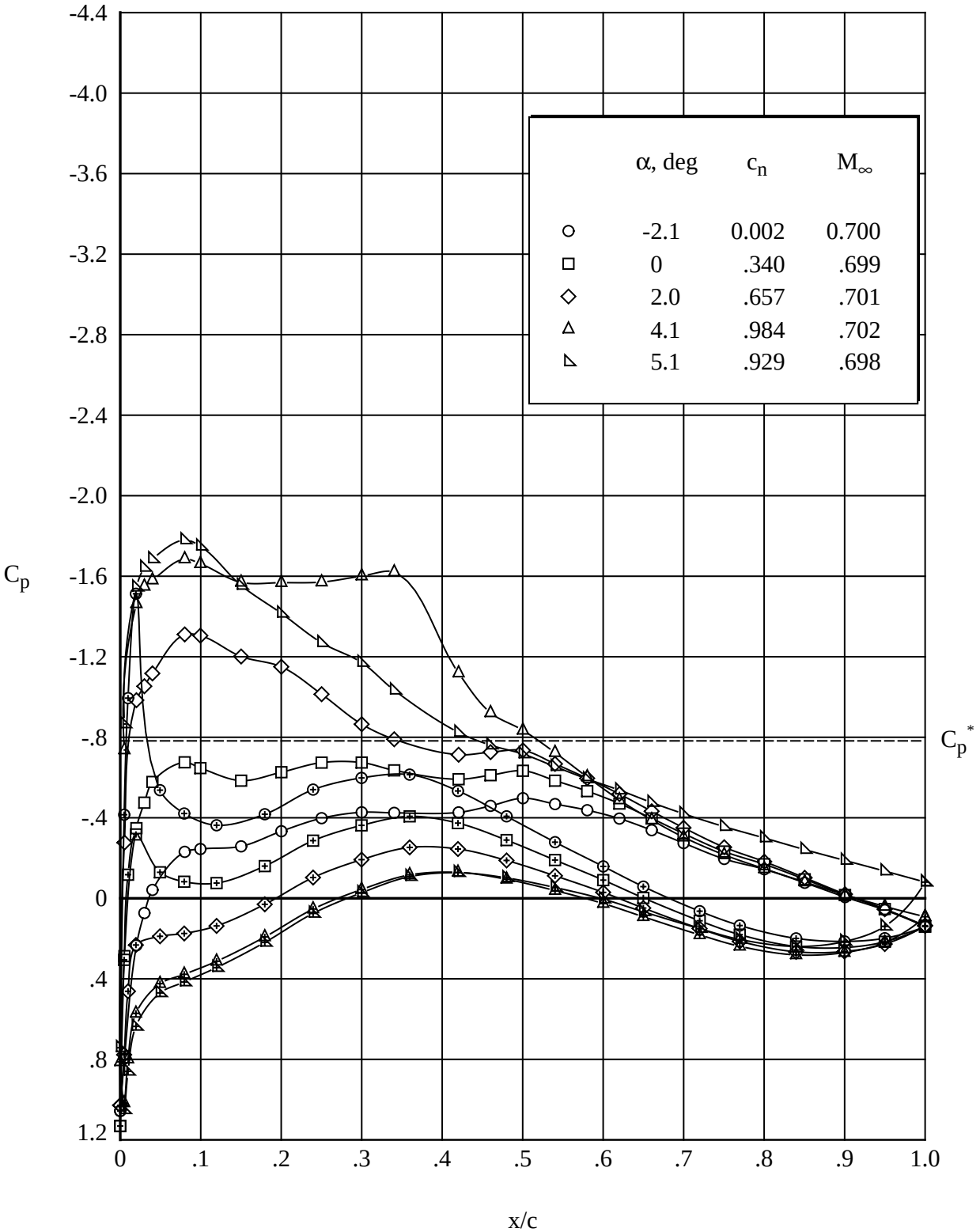

(d) $R_c = 9.0 \times 10^6$.

Figure 21. Continued.

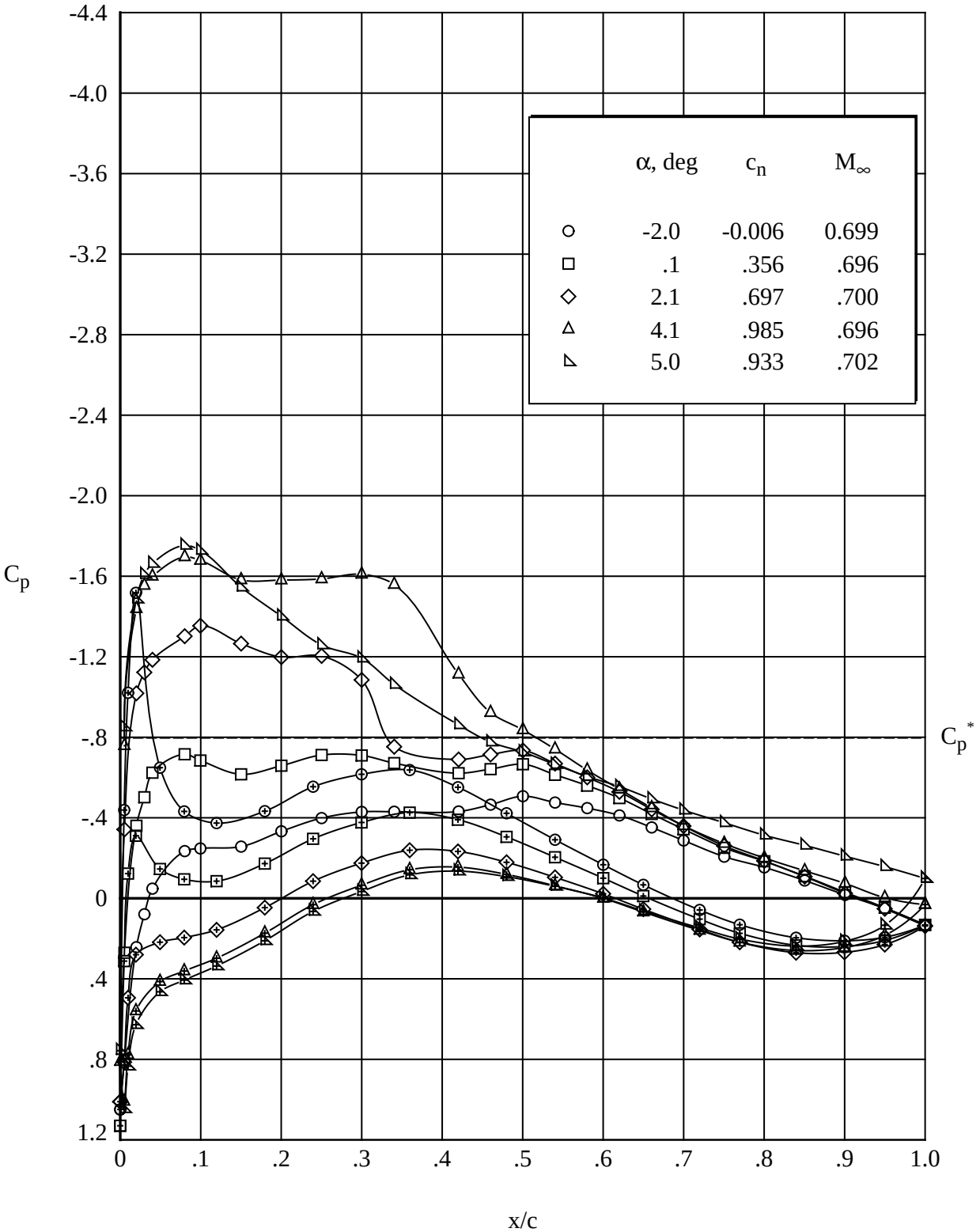

(e) $R_c = 13.5 \times 10^6$.

Figure 21. Continued.

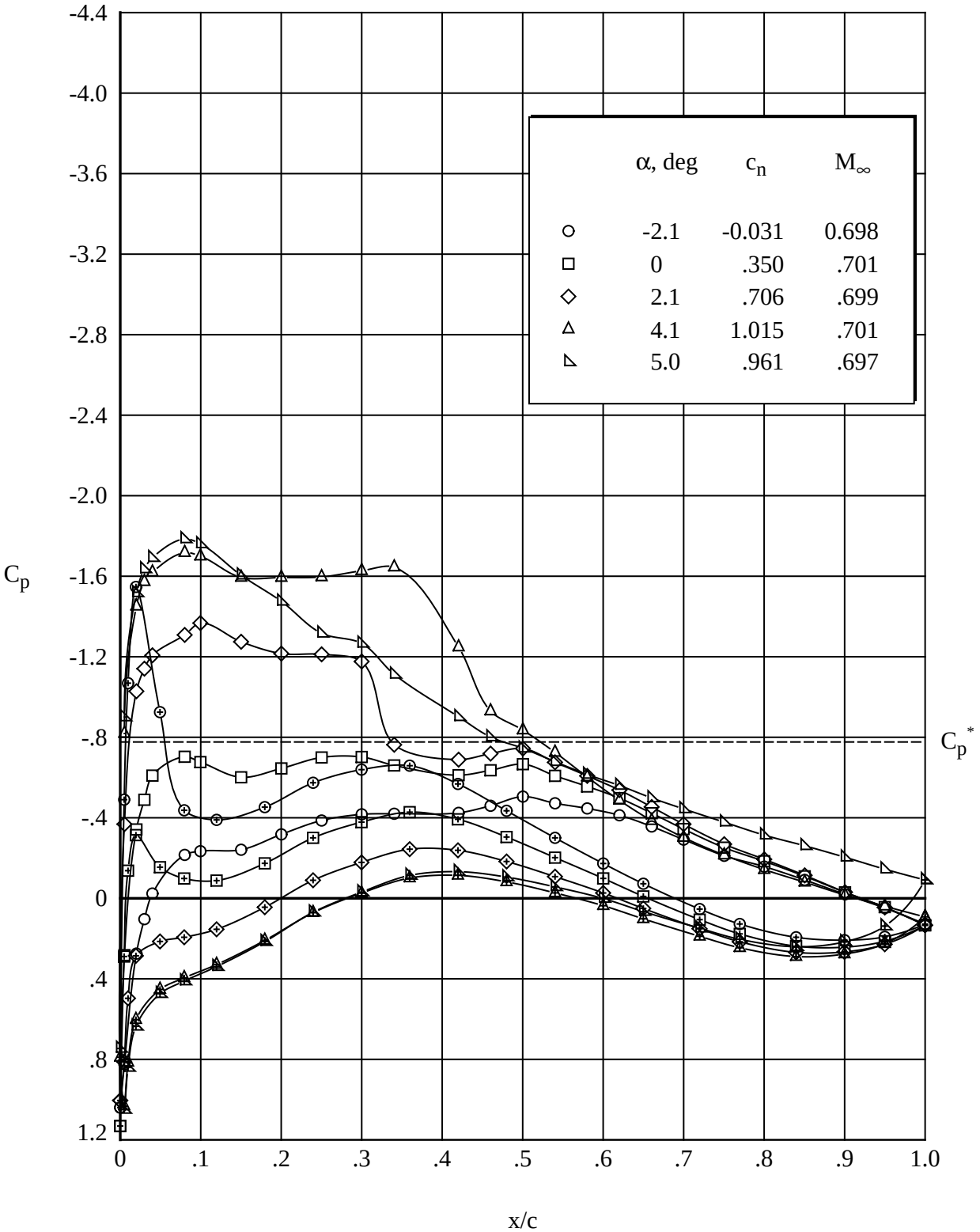

(f) $R_c = 18.0 \times 10^6$.

Figure 21. Concluded.

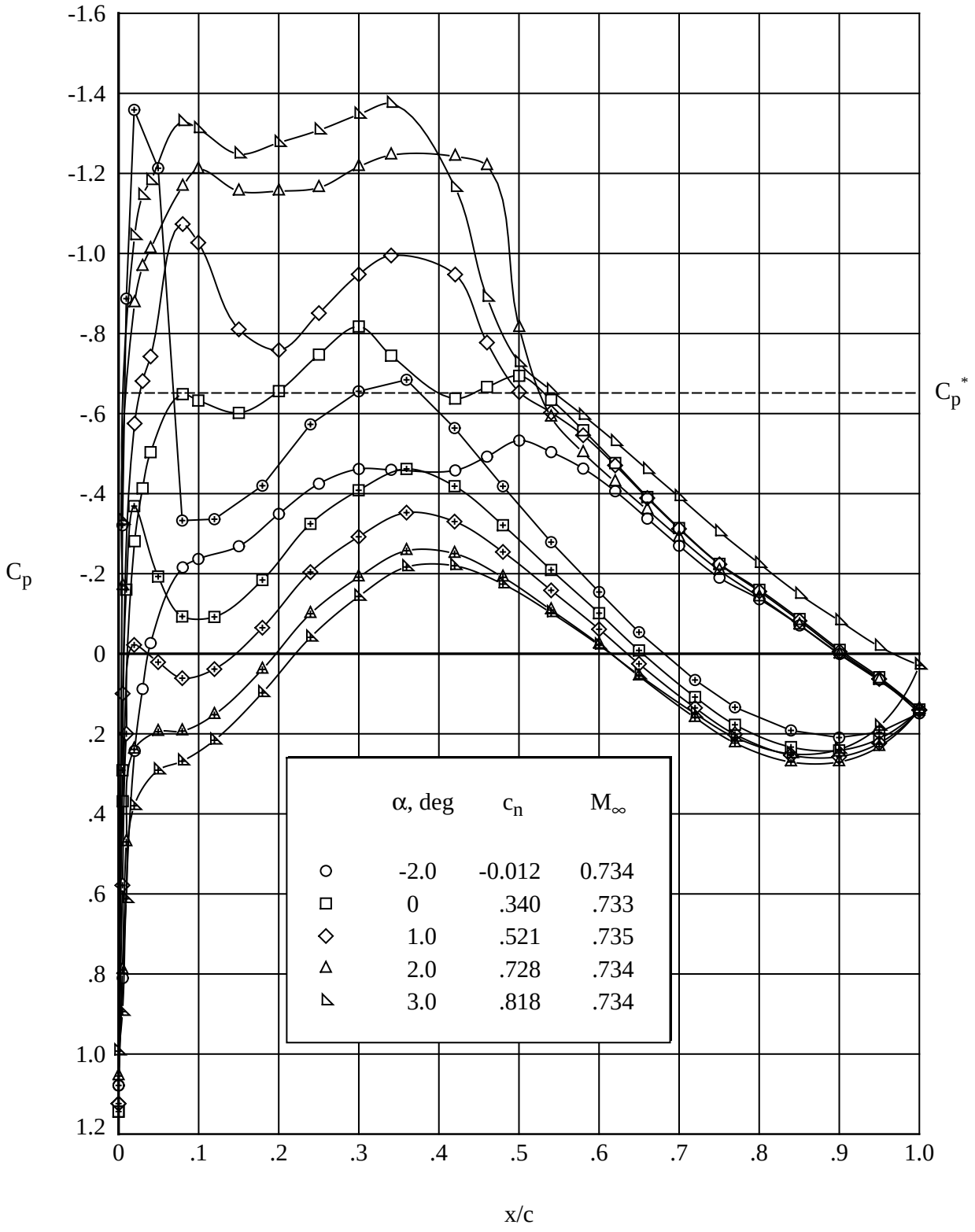

(a) $R_c = 4.5 \times 10^6$.

Figure 22. Effect of angle of attack on chordwise pressure distributions for modified airfoil. Open symbols denote upper surface; "+" within symbol denotes lower surface. $M_\infty = 0.735$.

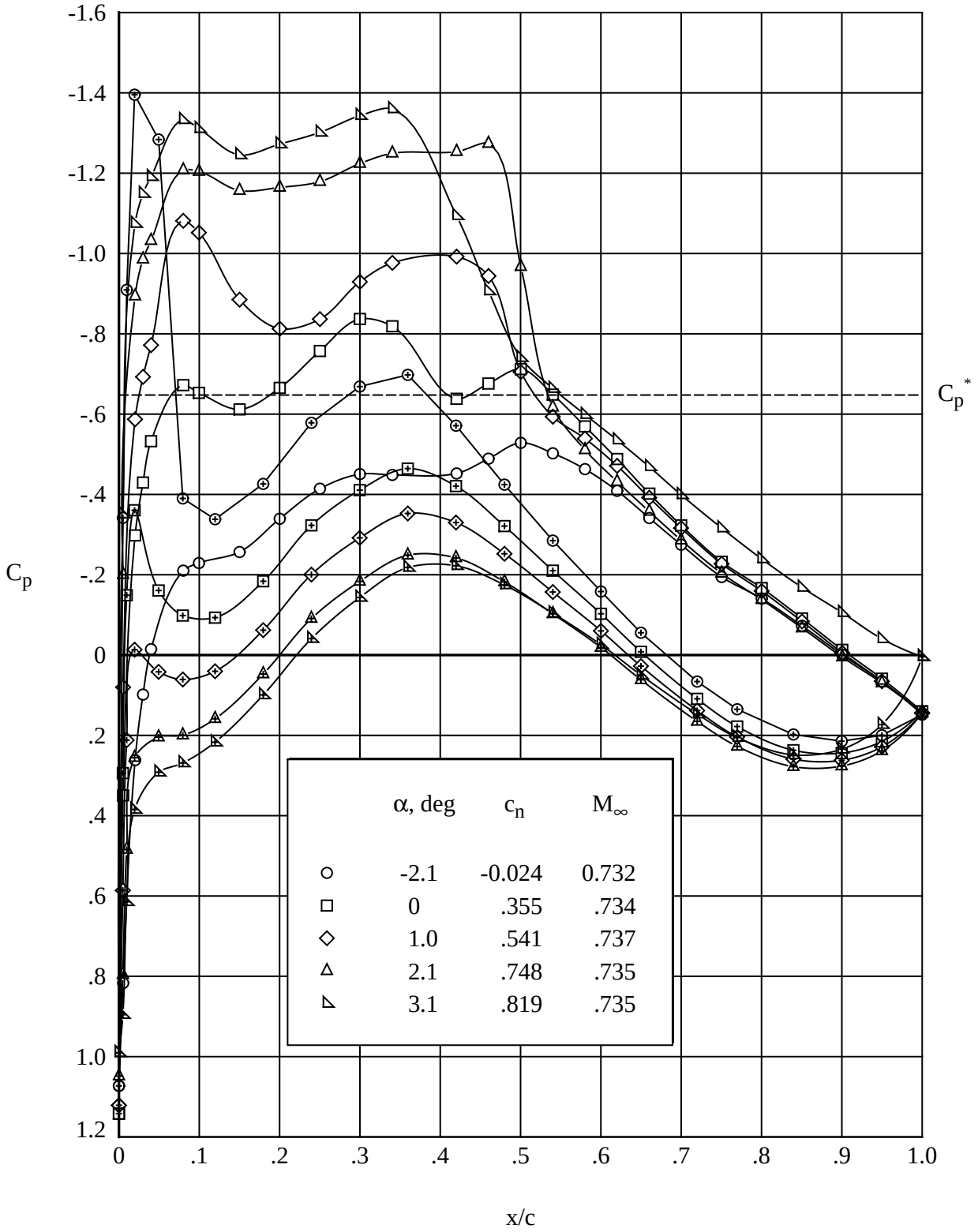

(b) $R_c = 6.5 \times 10^6$.

Figure 22. Continued.

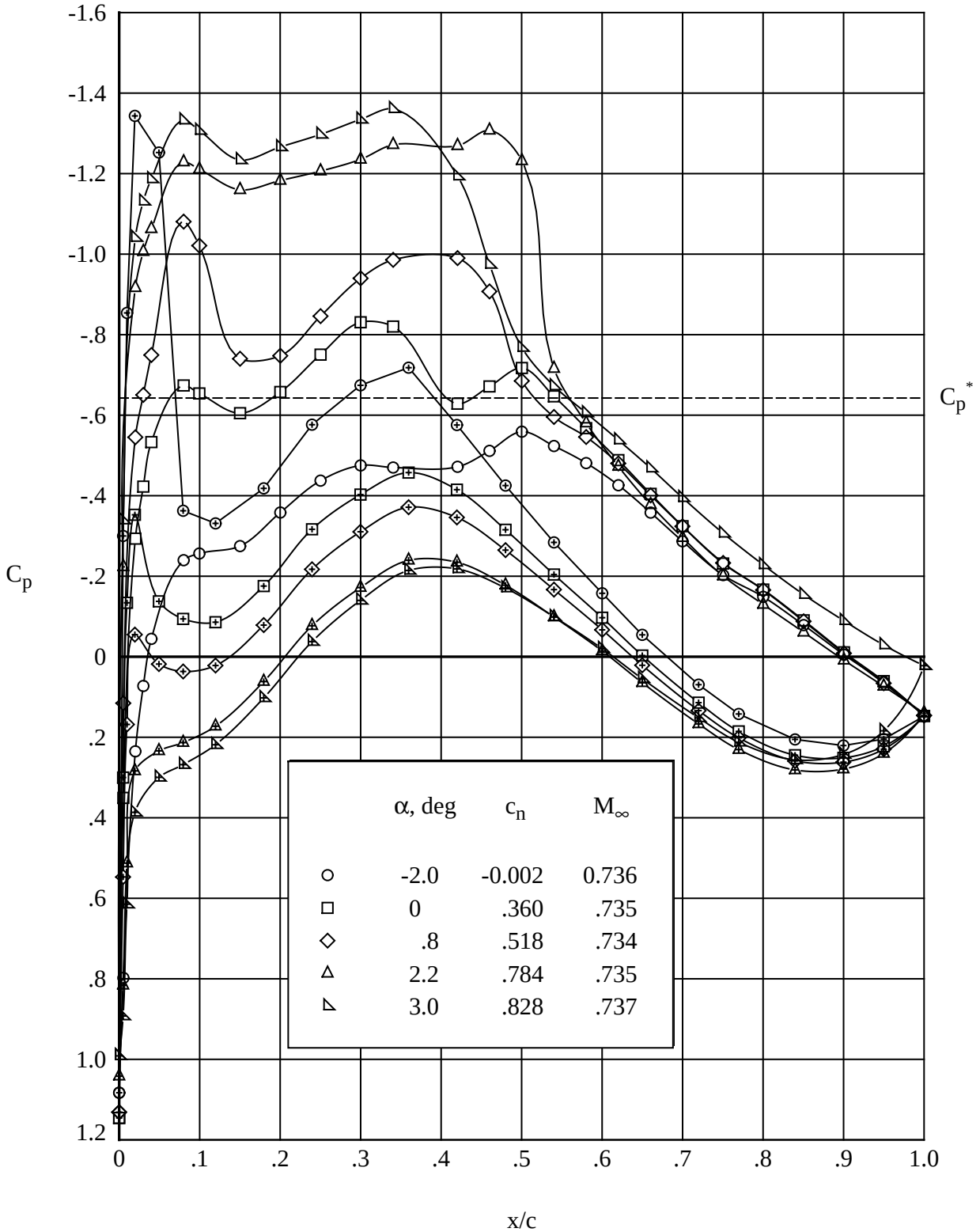

(c) $R_c = 9.0 \times 10^6$.

Figure 22. Continued.

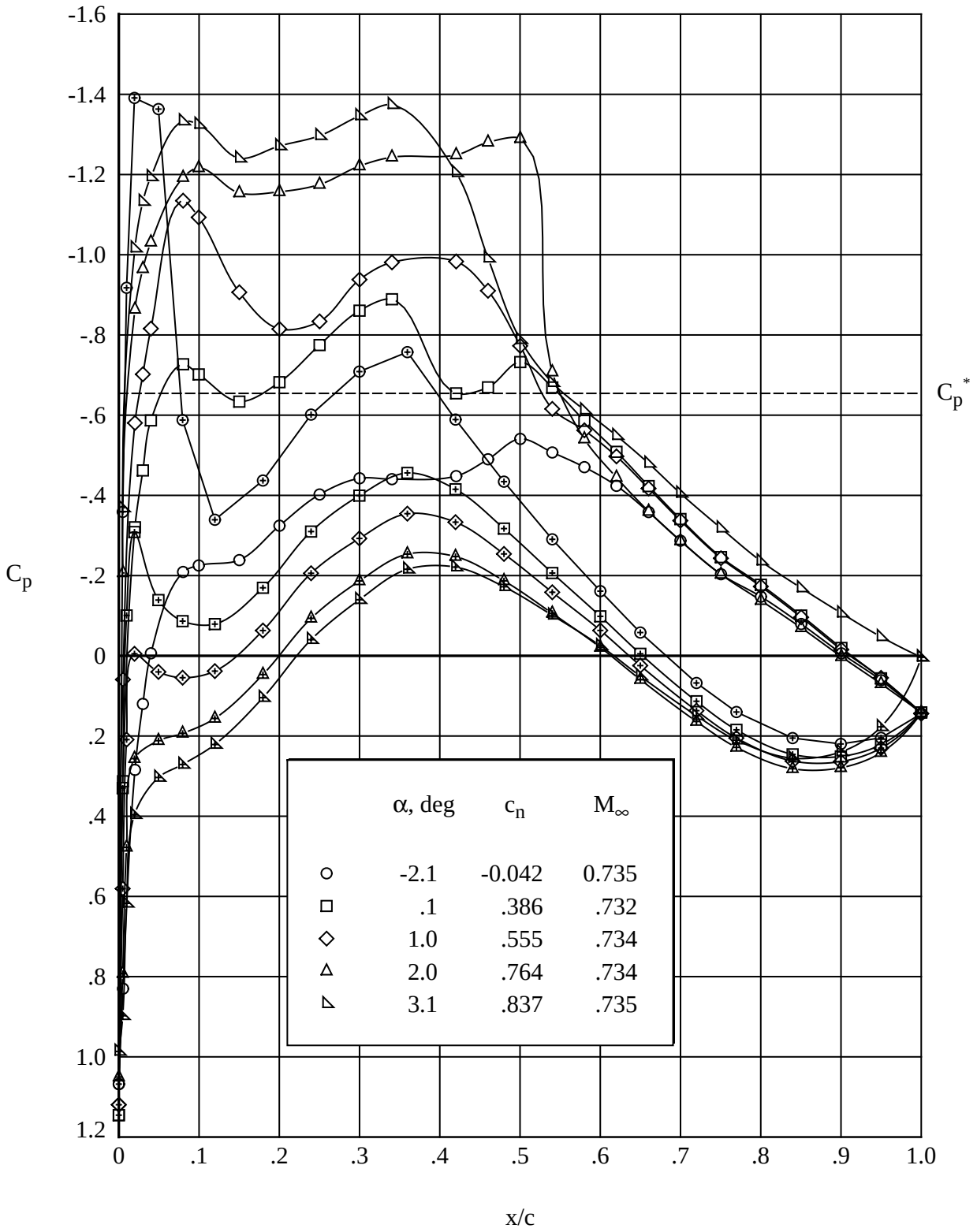

(d) $R_c = 13.5 \times 10^6$.

Figure 22. Concluded.

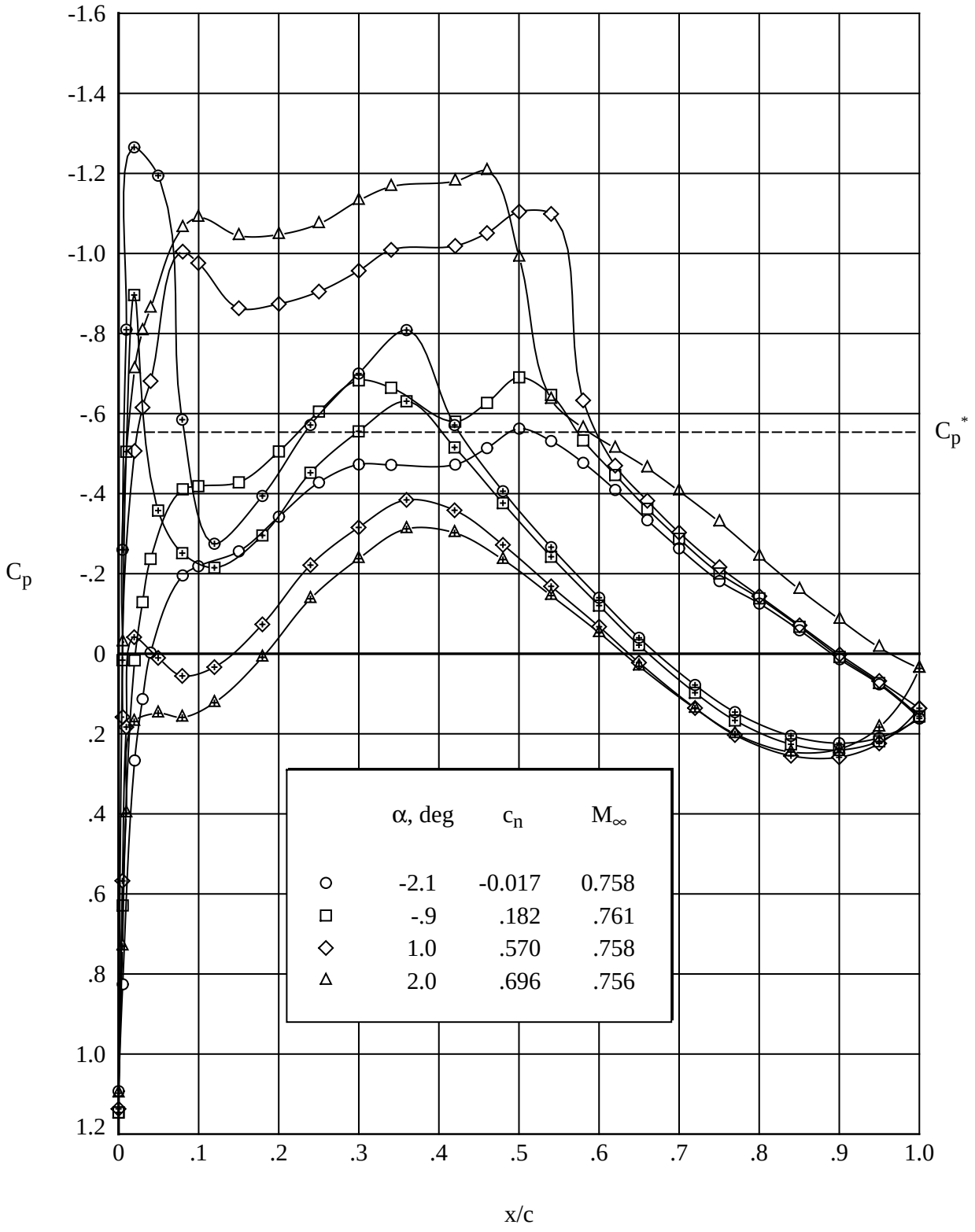

(a) $R_c = 4.5 \times 10^6$.

Figure 23. Effect of angle of attack on chordwise pressure distributions for modified airfoil. Open symbols denote upper surface; "+" within symbol denotes lower surface. $M_\infty = 0.760$.

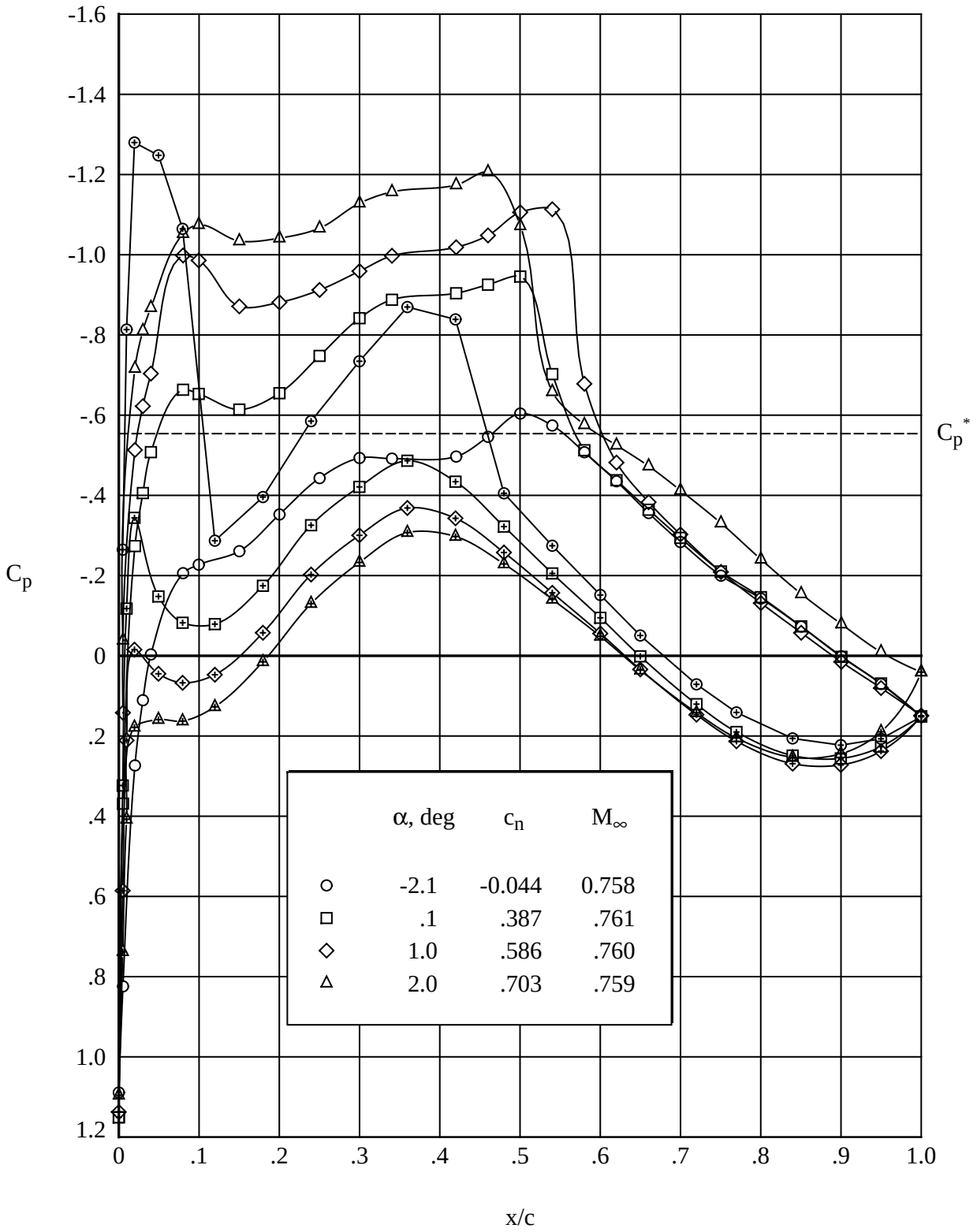

(b) $R_c = 6.5 \times 10^6$.

Figure 23. Continued.

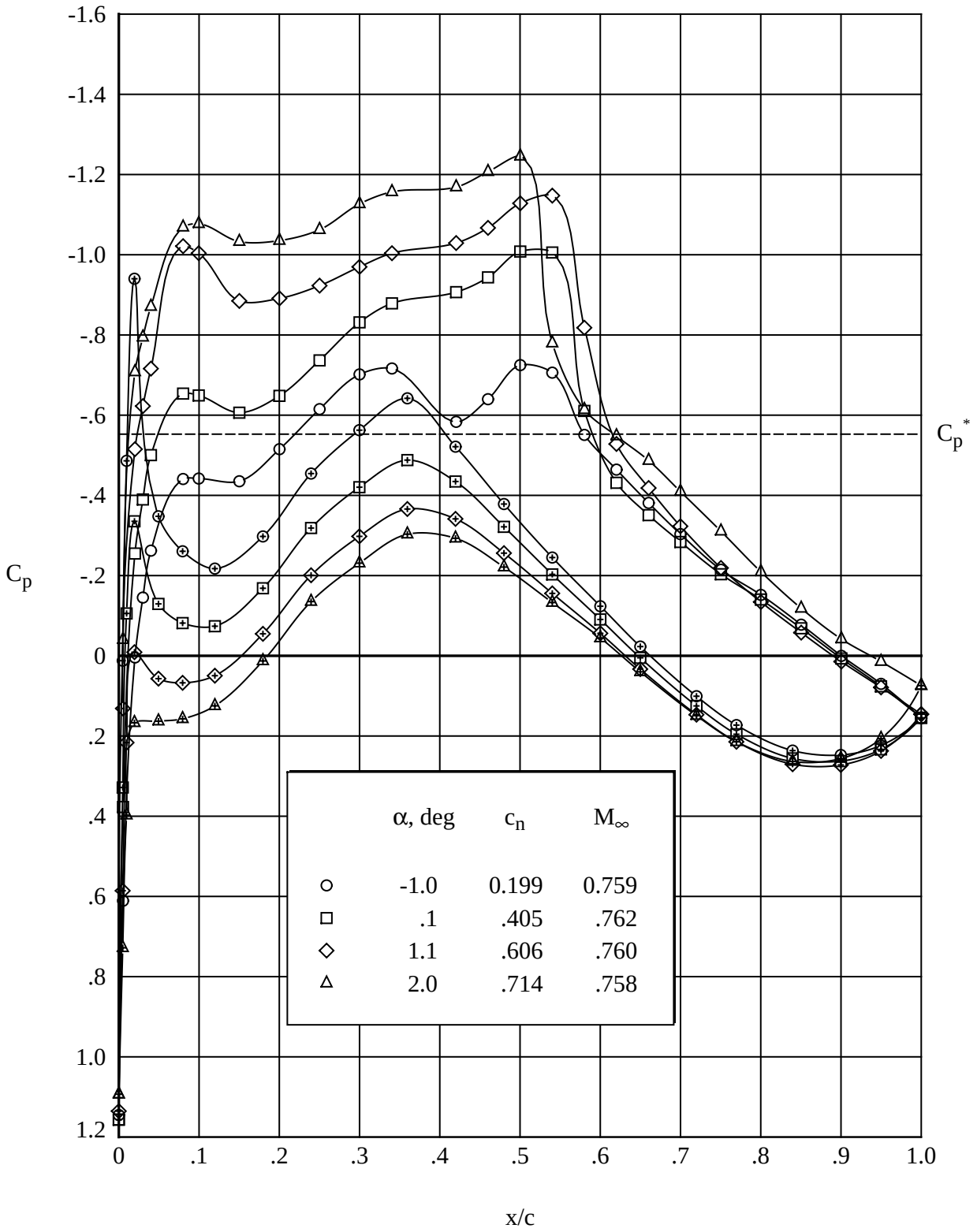

(c) $R_c = 9.0 \times 10^6$.

Figure 23. Concluded.

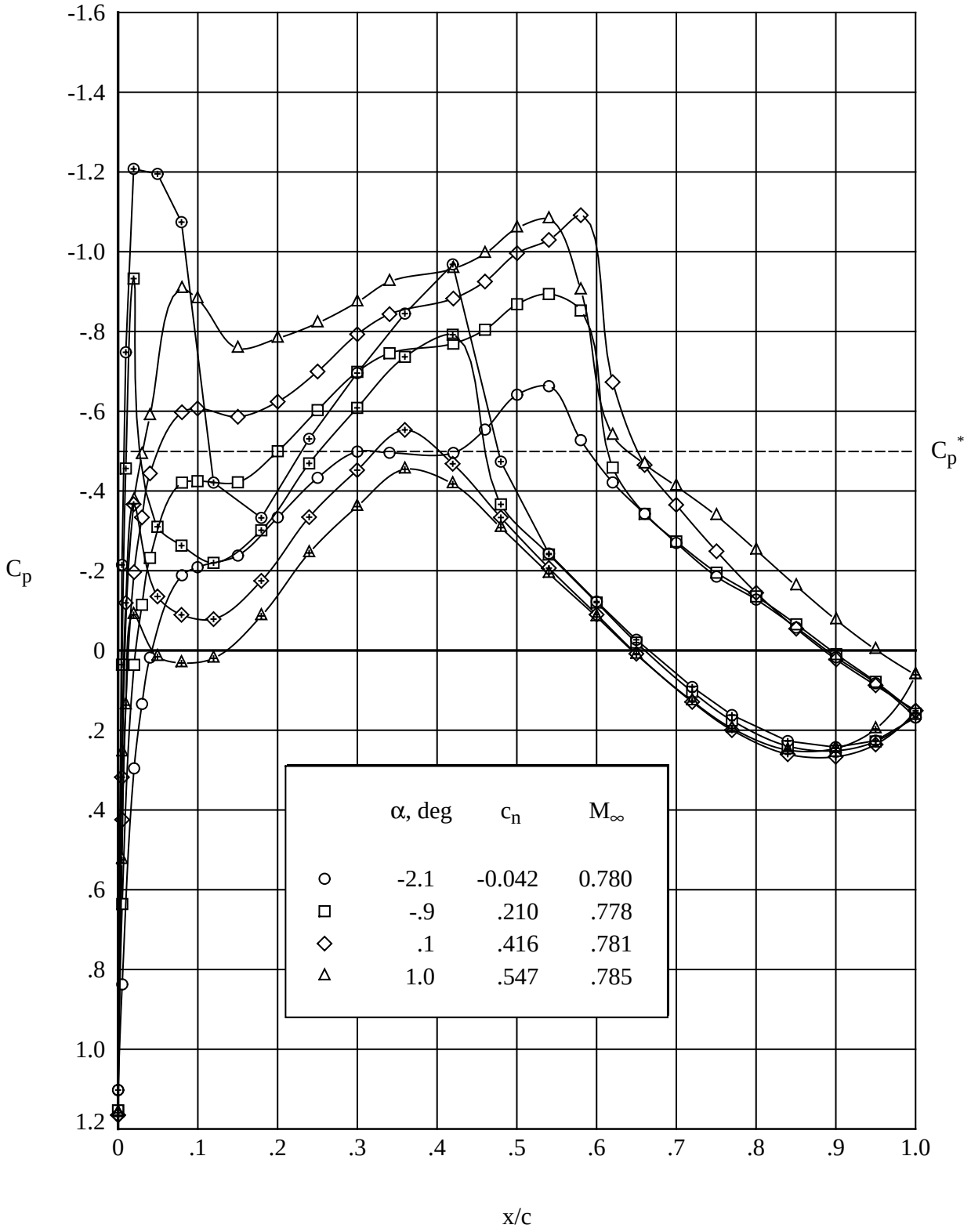

Figure 24. Effect of angle of attack on chordwise pressure distributions for modified airfoil. Open symbols denote upper surface; "+" within symbol denotes lower surface. $M_\infty = 0.780$, $R_c = 9.0 \times 10^6$.

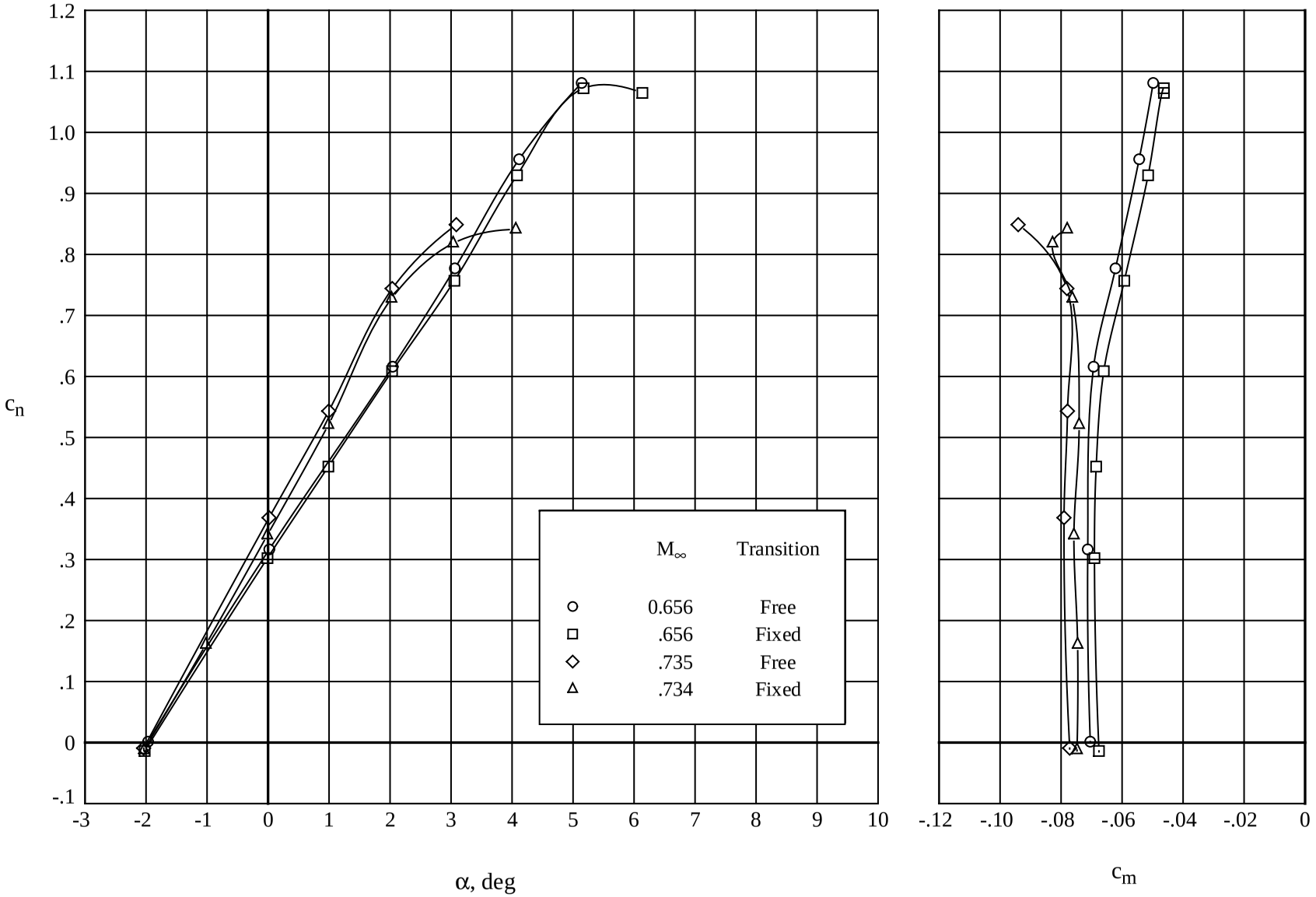

(a) Normal-force and pitching-moment coefficients. $R_c = 4.5 \times 10^6$.

Figure 25. Effect of free transition on force and moment coefficients for modified airfoil.

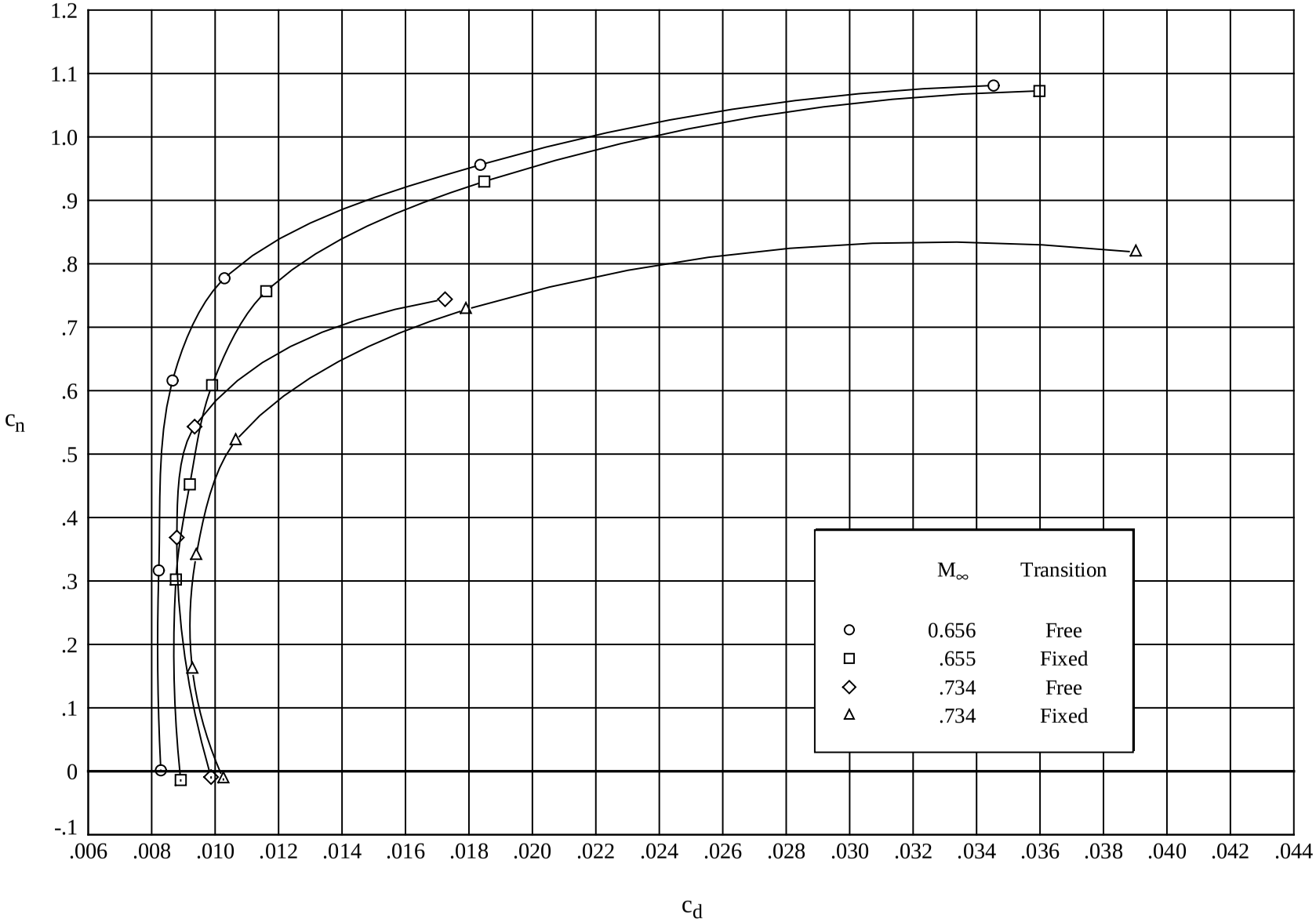

(b) Drag coefficient. $R_c = 4.5 \times 10^6$.

Figure 25. Continued.

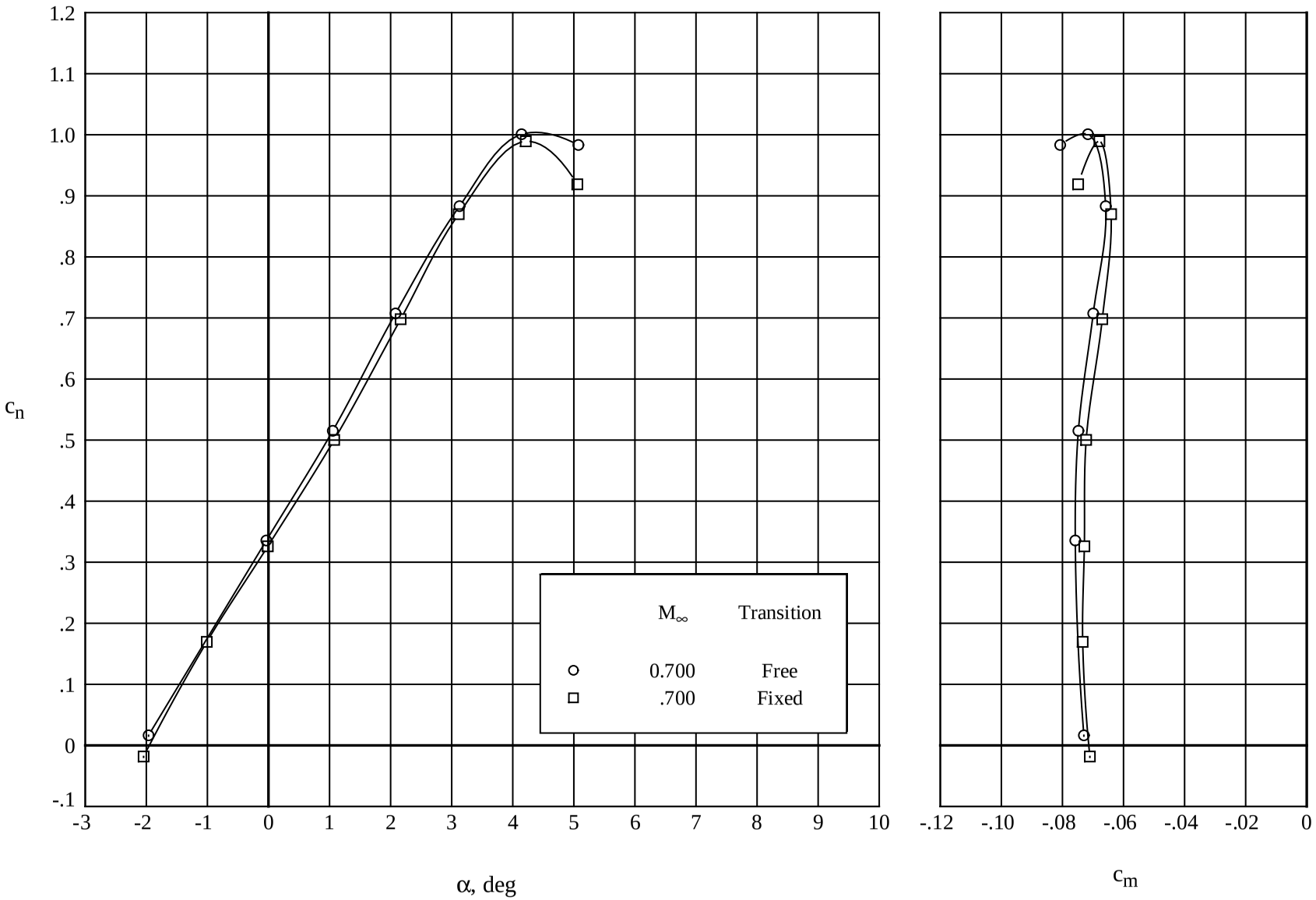

(c) Normal-force and pitching-moment coefficients. $R_c = 6.5 \times 10^6$.

Figure 25. Continued.

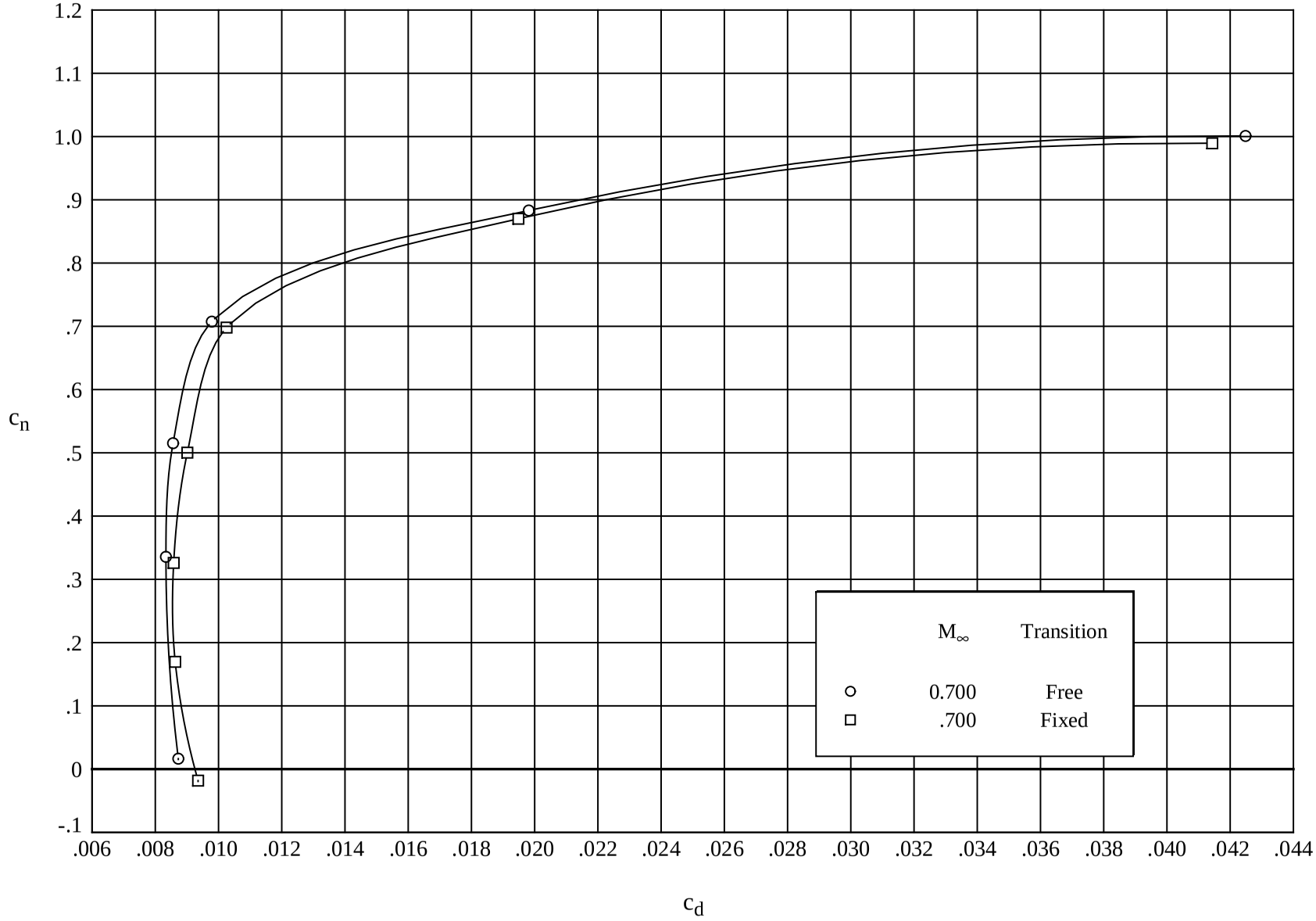

(d) Drag coefficient. $R_c = 6.5 \times 10^6$.

Figure 25. Continued.

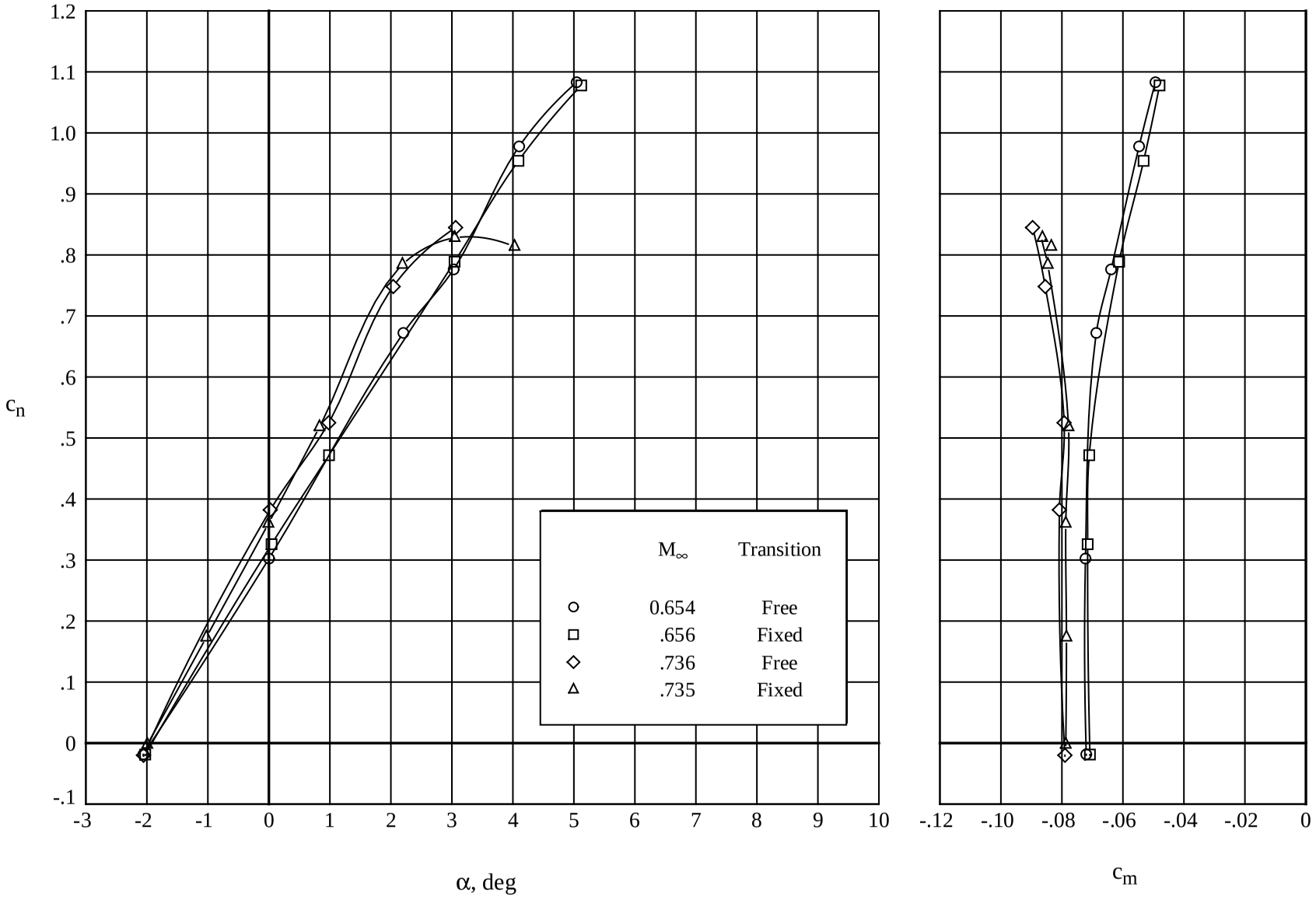

(e) Normal-force and pitching-moment coefficients. $R_c = 9.0 \times 10^6$.

Figure 25. Continued.

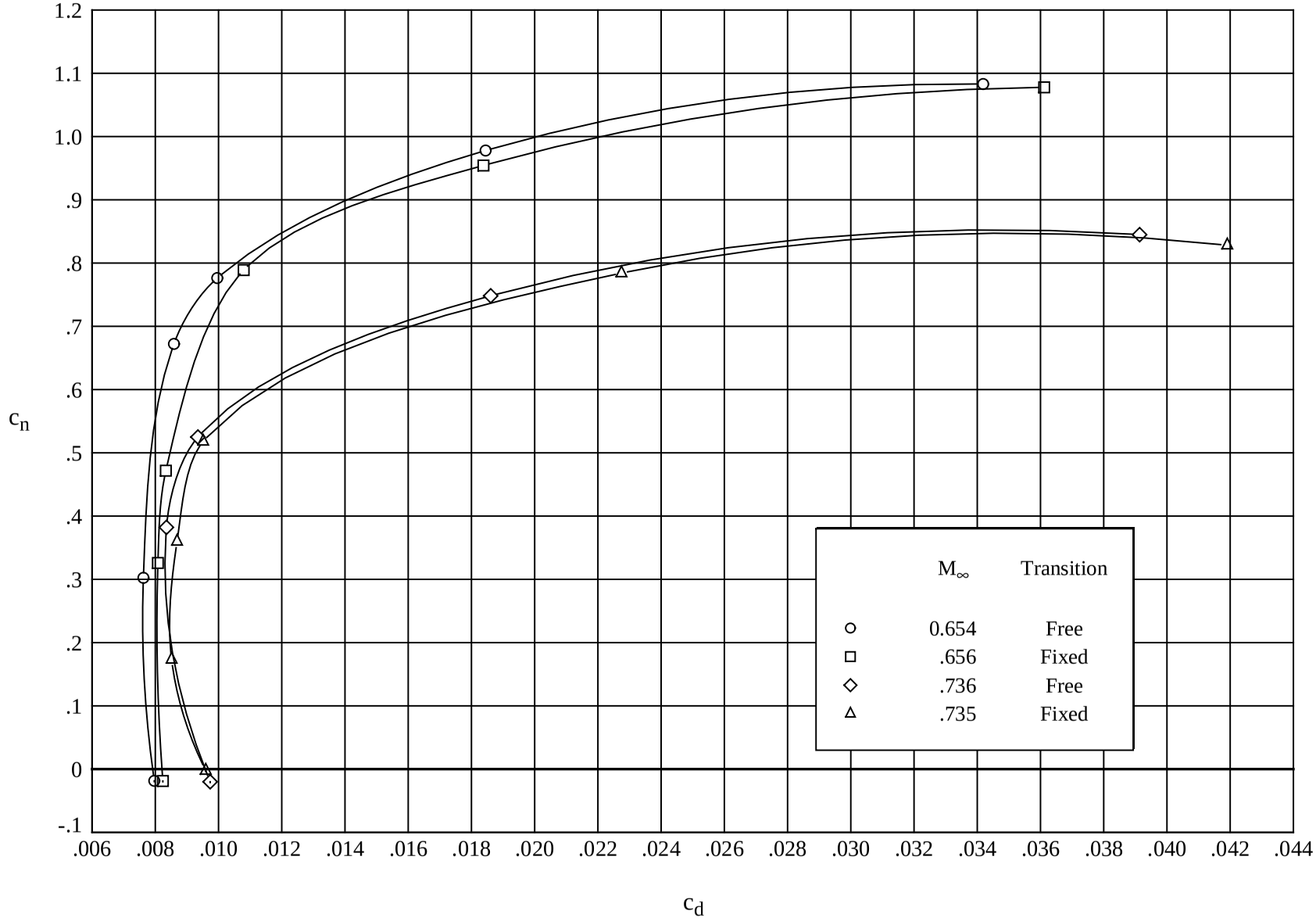

(f) Drag coefficient. $R_c = 9.0 \times 10^6$.

Figure 25. Concluded.

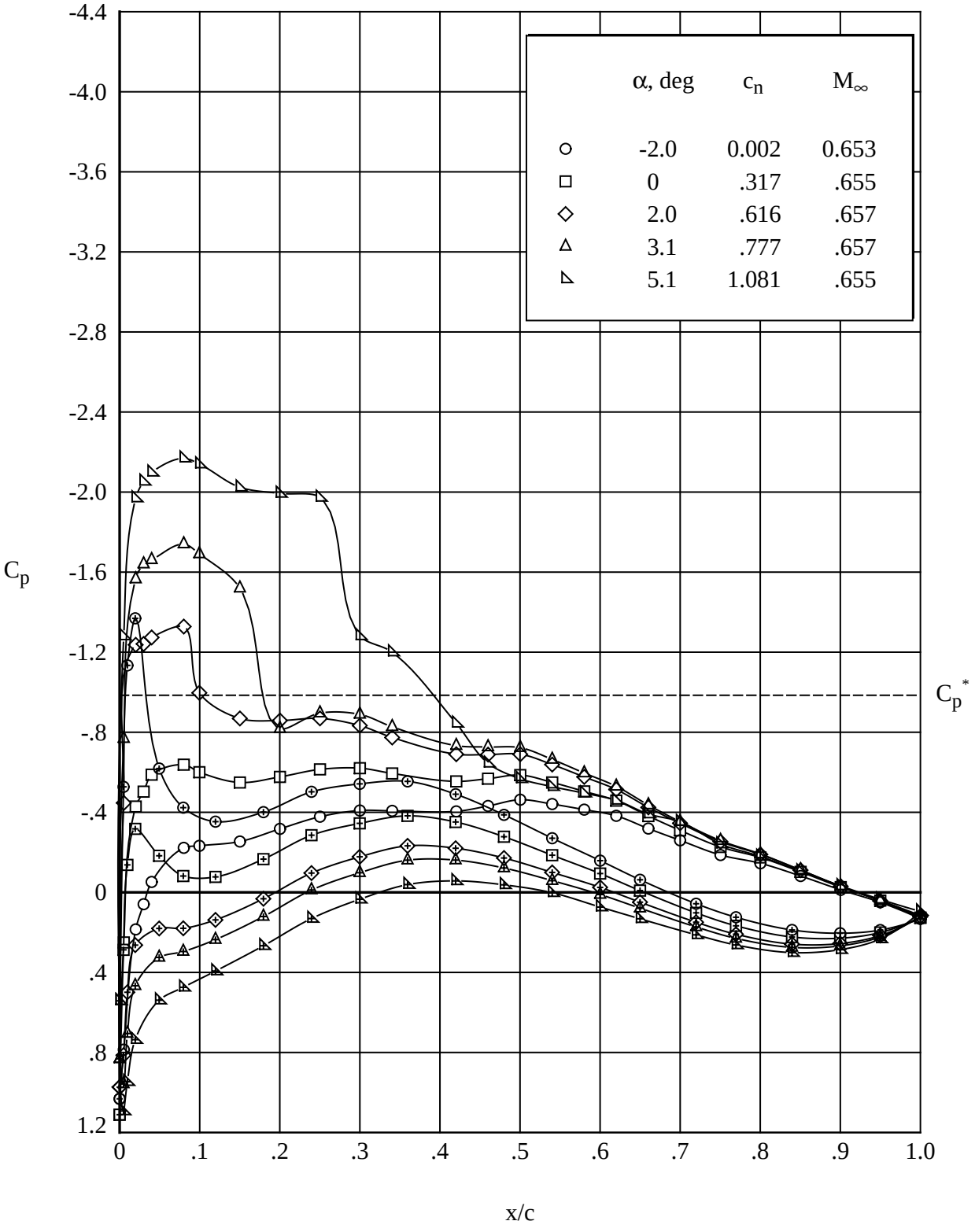

(a) $M_\infty = 0.655$, $R_c = 4.5 \times 10^6$.

Figure 26. Effect of angle of attack on chordwise pressure distributions for modified airfoil with free transition. Open symbols denote upper surface; "+" within symbol denotes lower surface.

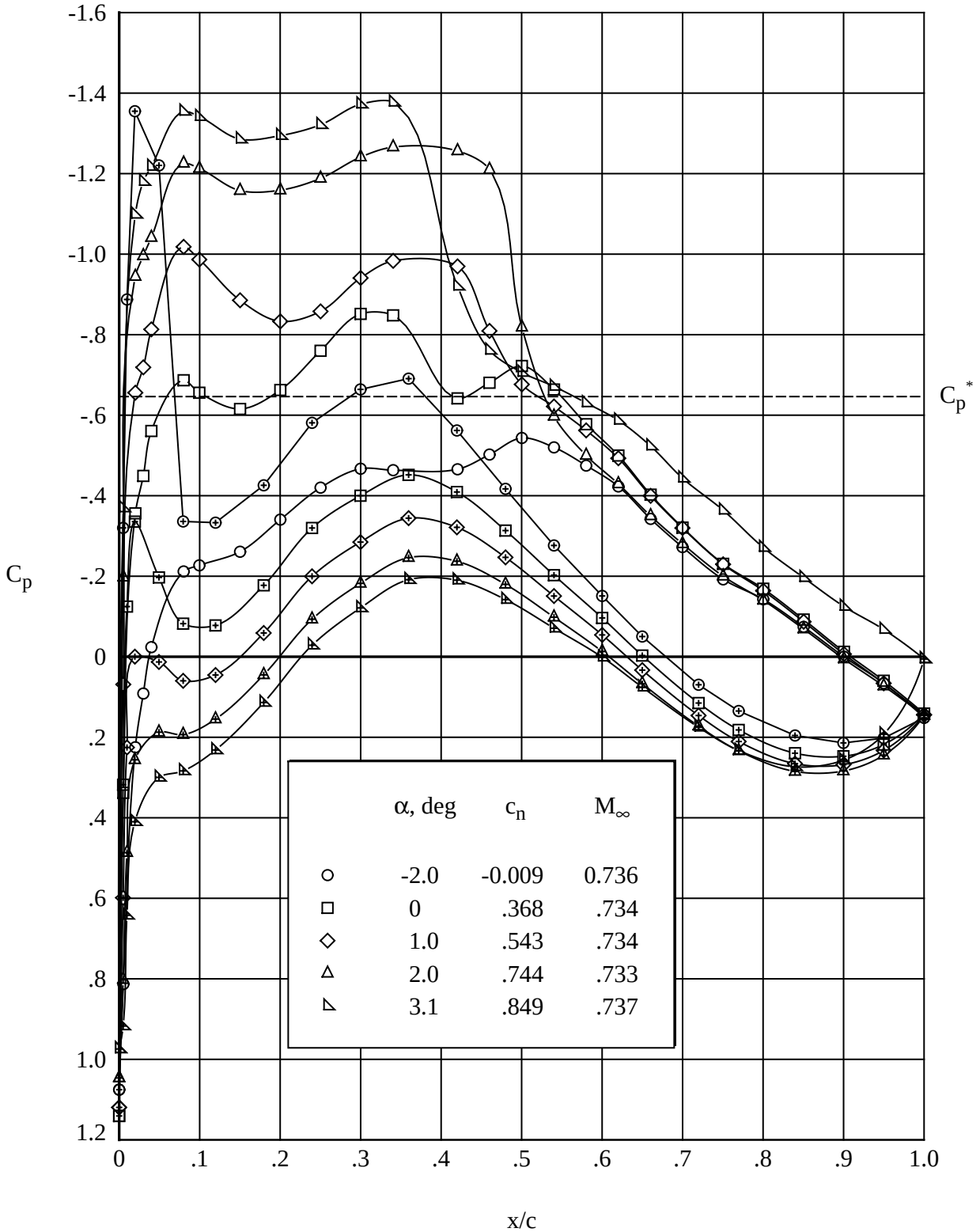

(b) $M_\infty = 0.735$, $R_c = 4.5 \times 10^6$.

Figure 26. Continued.

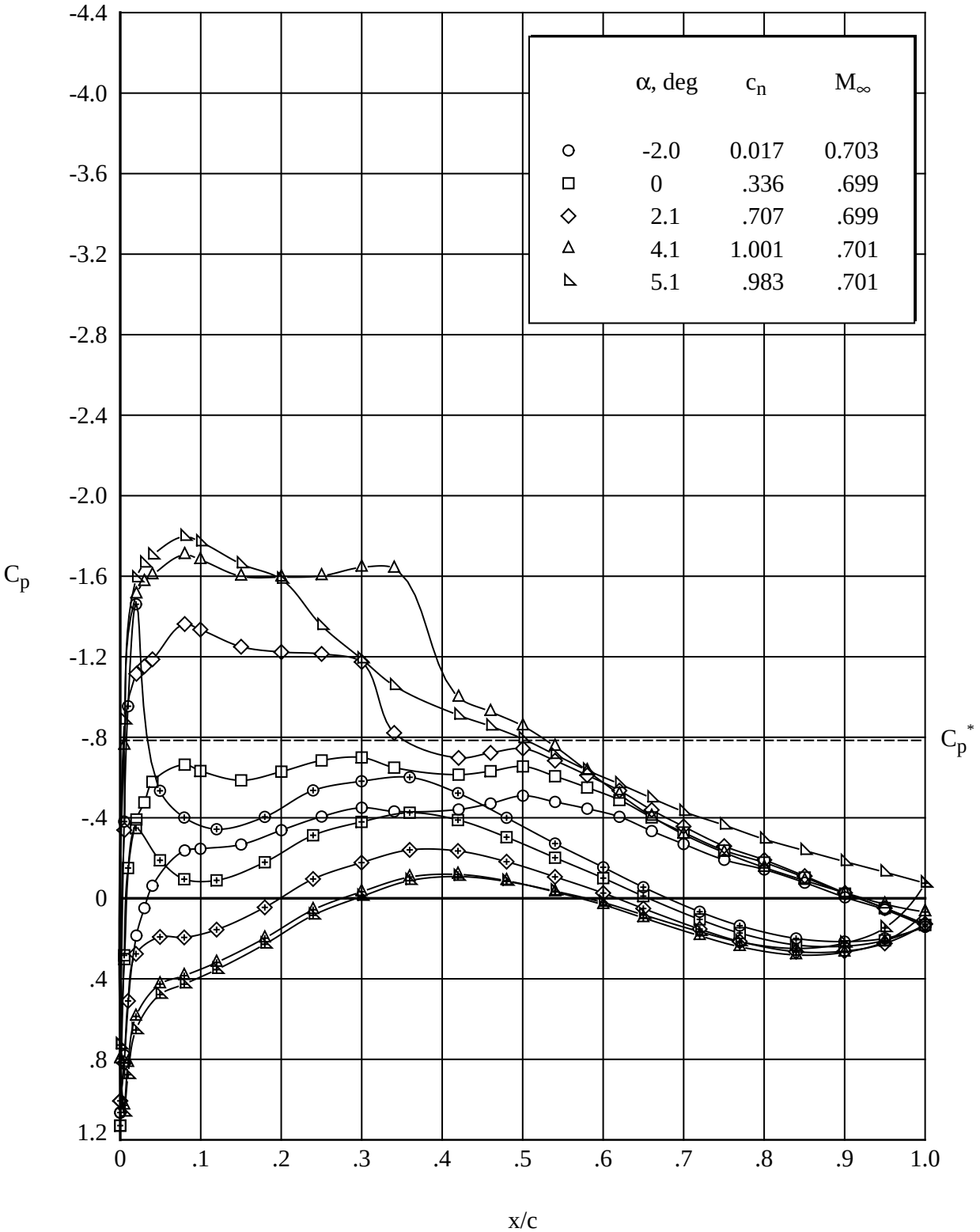

(c) $M_\infty = 0.700$, $R_c = 6.5 \times 10^6$.

Figure 26. Continued.

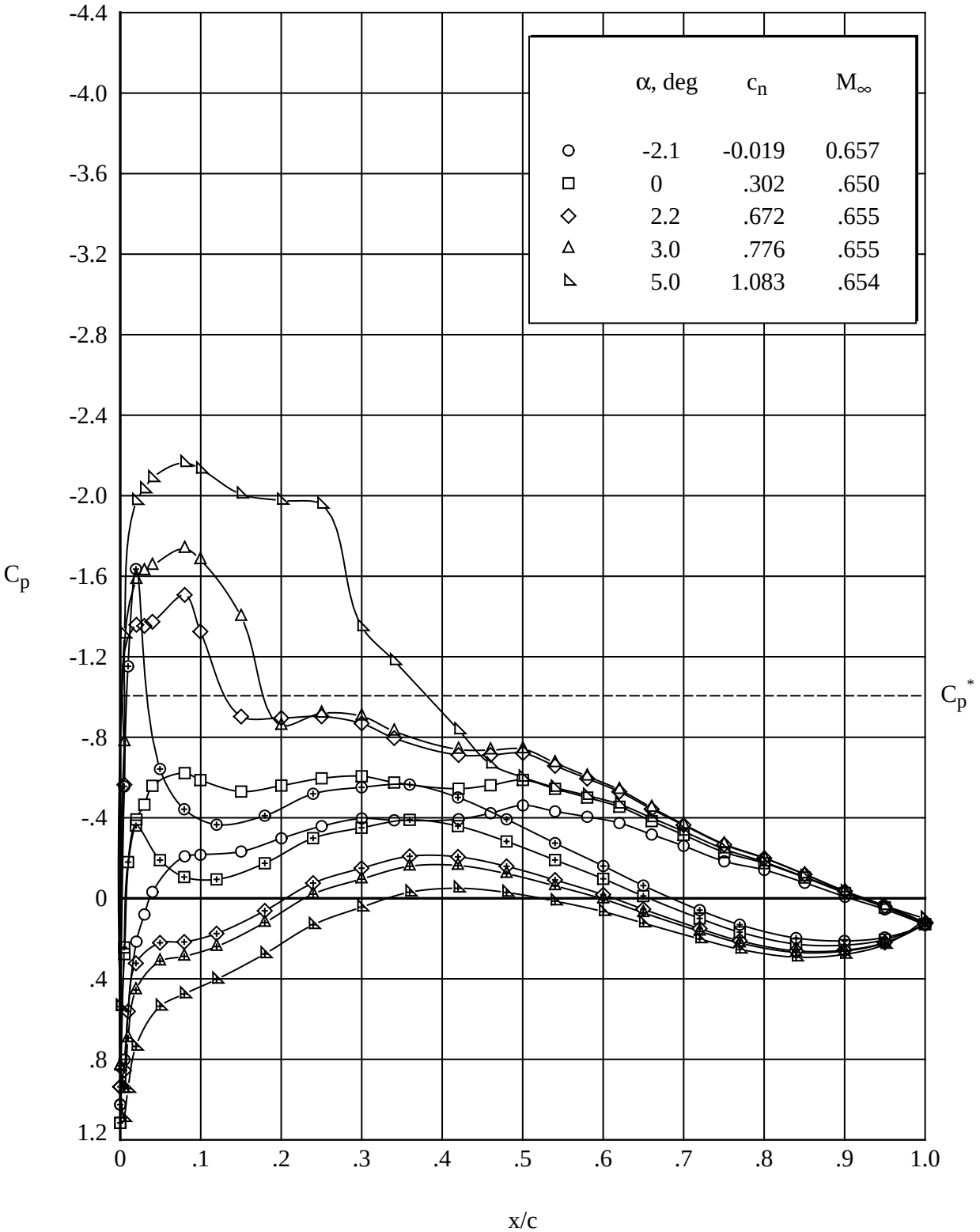

(d) $M_\infty = 0.655$, $R_c = 9.0 \times 10^6$.

Figure 26. Continued.

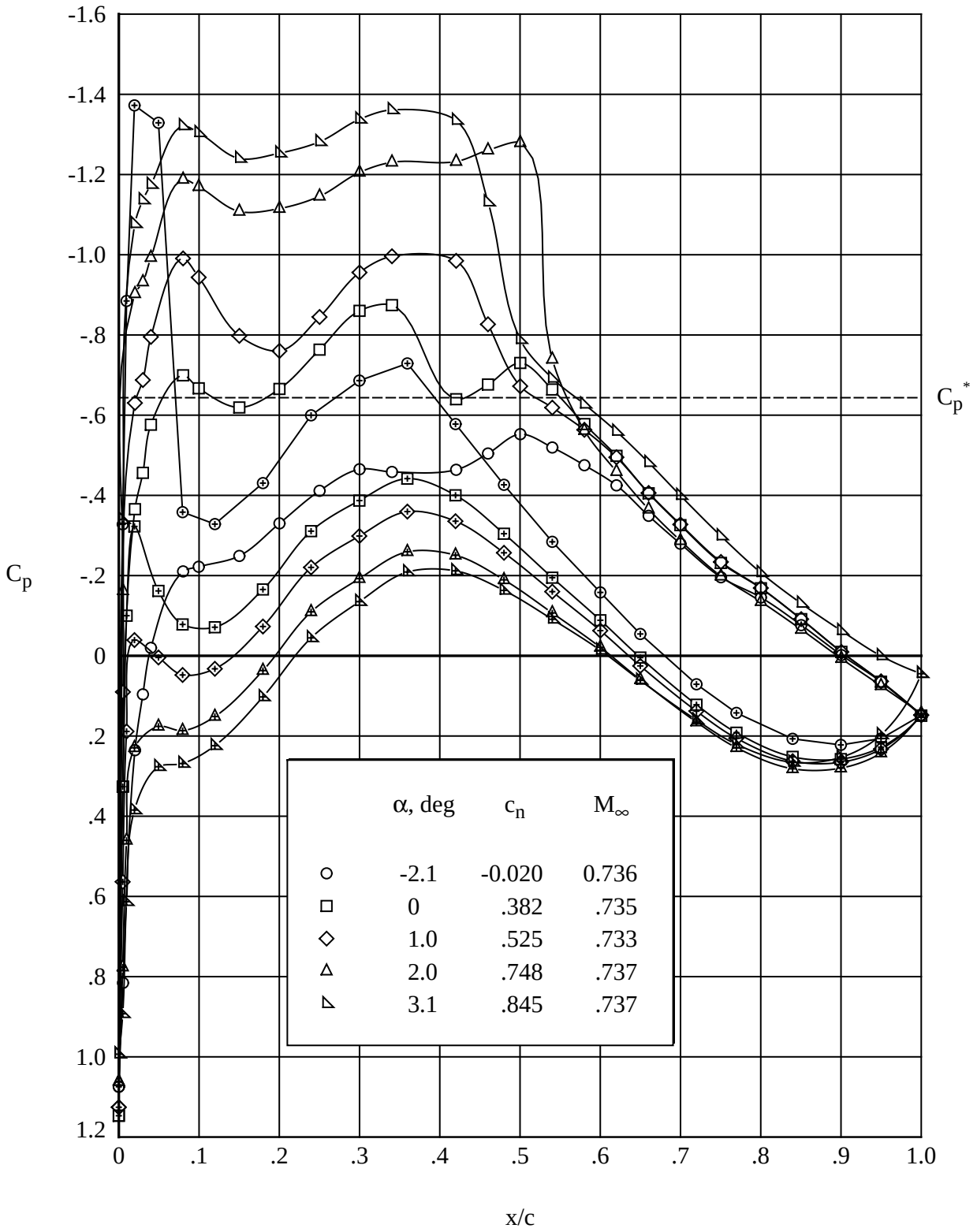

(e) $M_\infty = 0.735$, $R_c = 9.0 \times 10^6$.

Figure 26. Concluded.

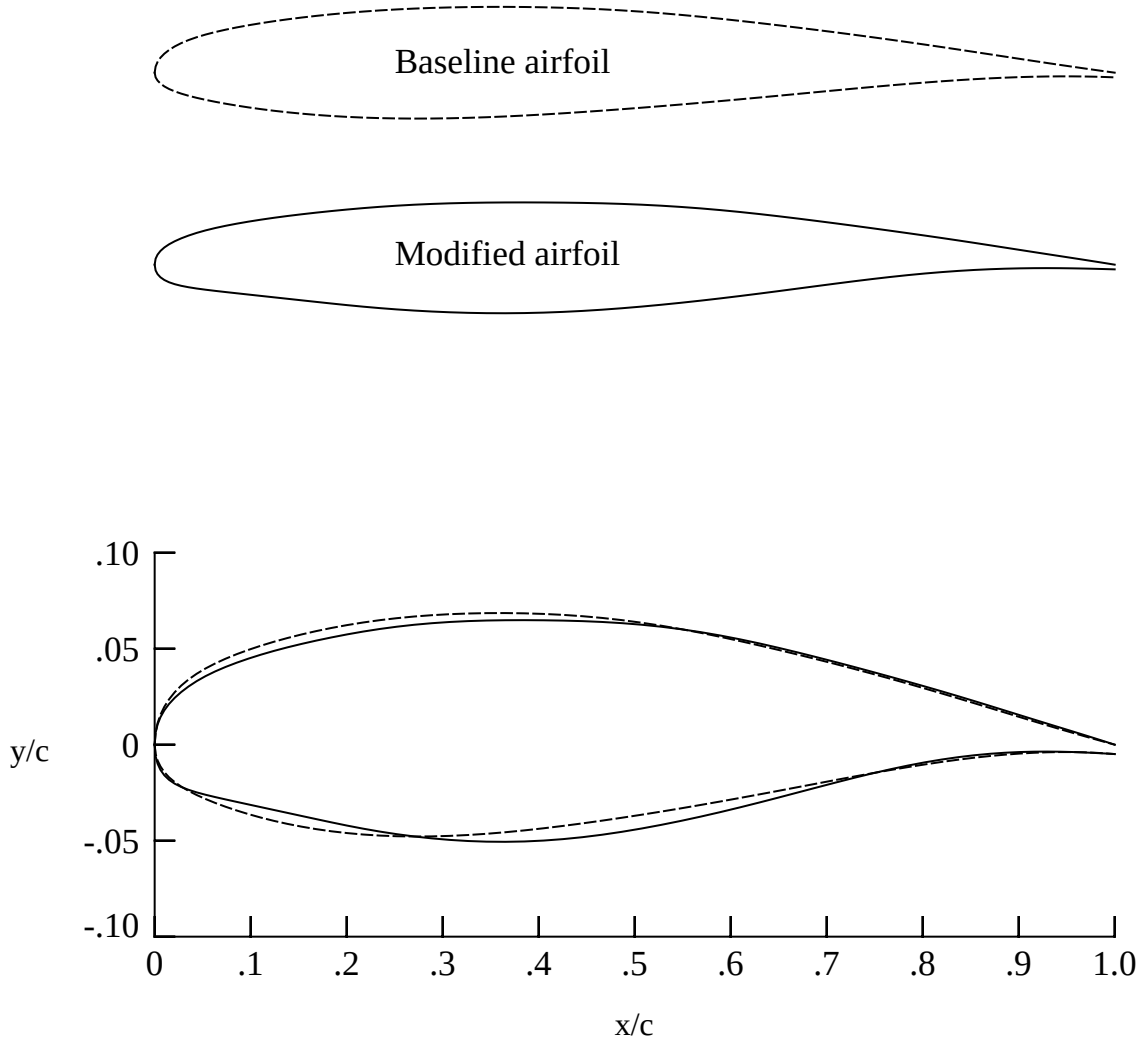

Figure 27. Comparison of baseline and modified airfoils. $t_{max} = 0.115c$ and $t_{0.85c} = 0.028c$ for both airfoils.

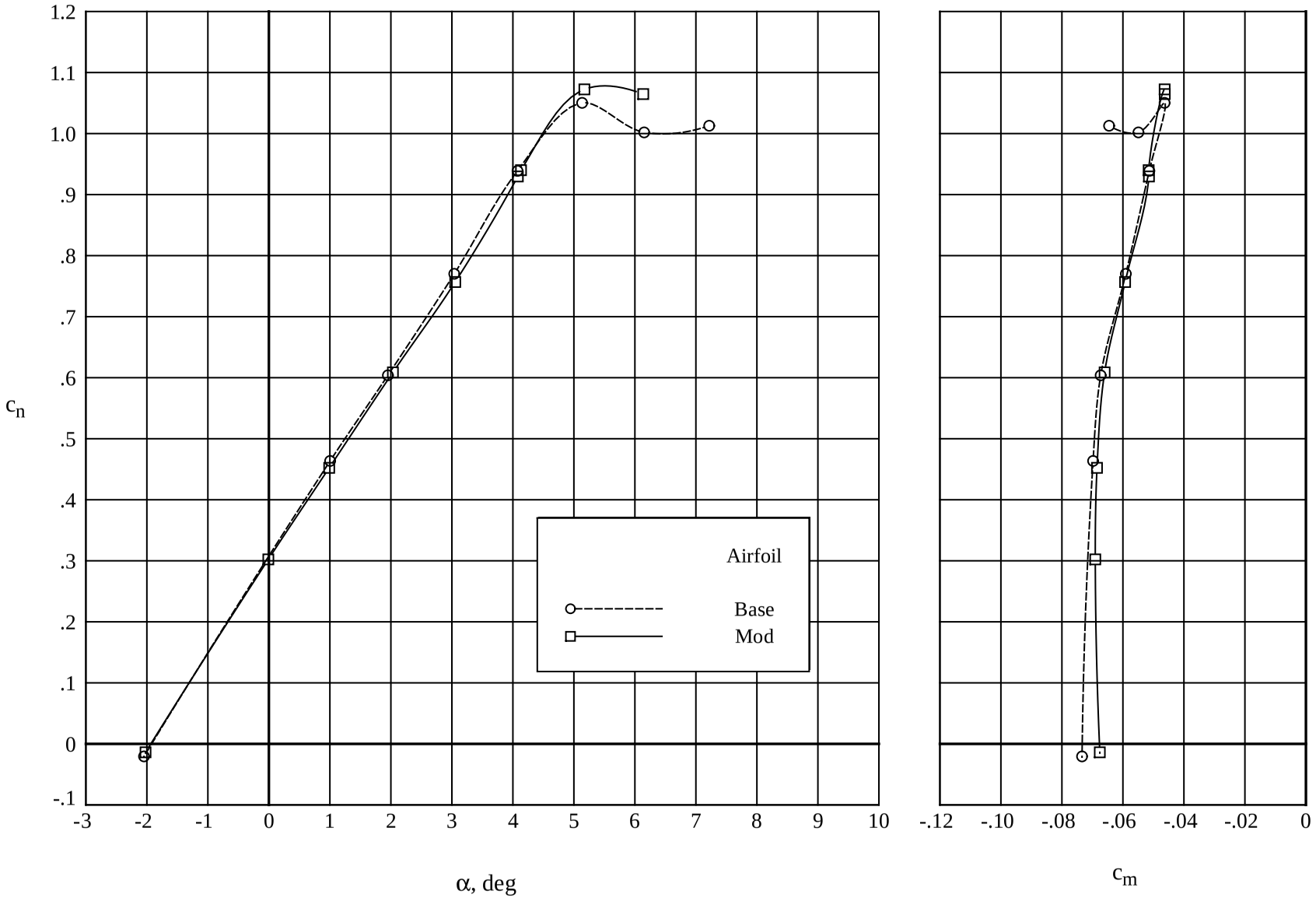

(a) Normal-force and pitching-moment coefficients.

Figure 28. Comparison of characteristics for baseline and modified airfoil. $M_\infty = 0.655$, $R_c = 4.5 \times 10^6$.

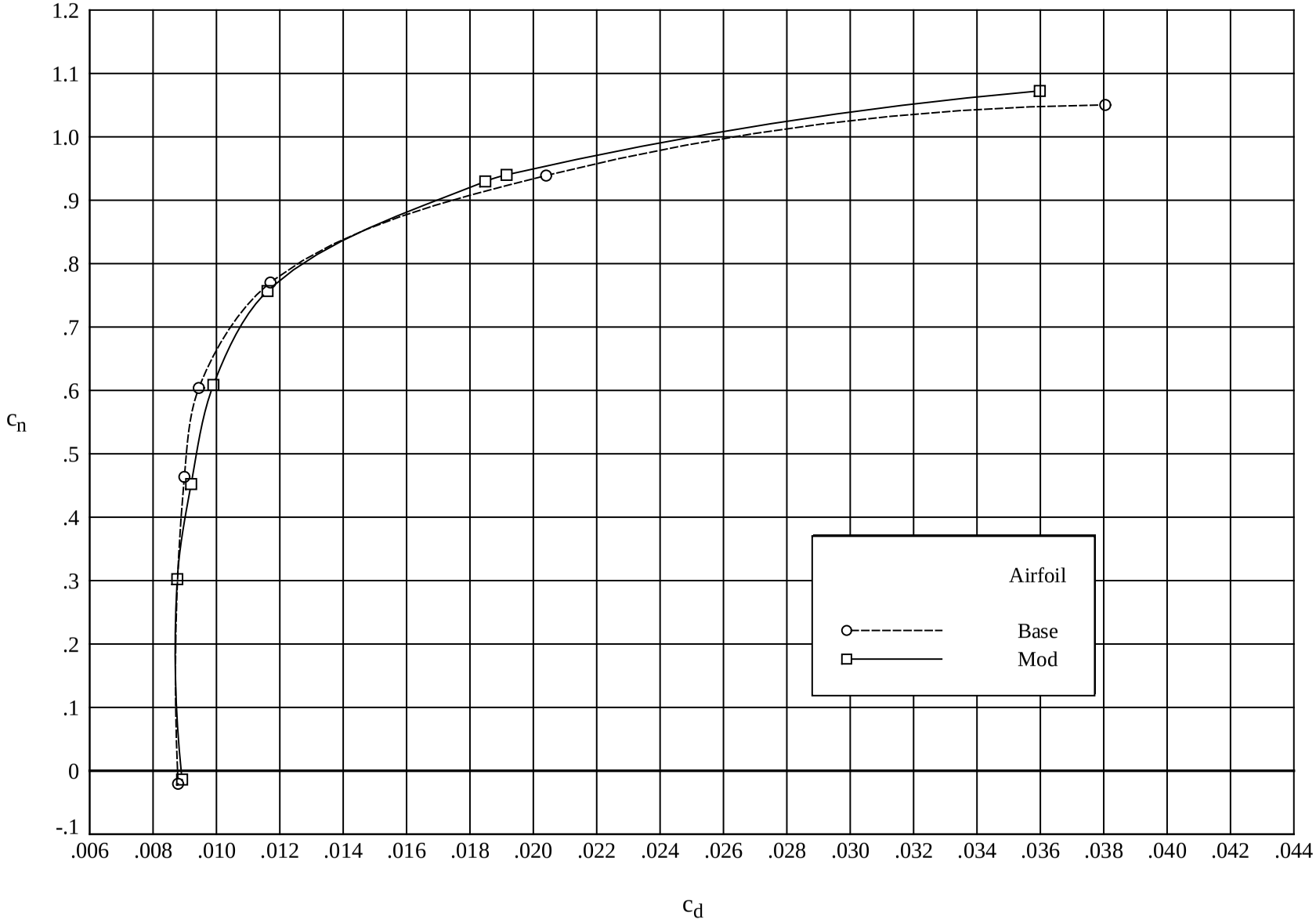

(b) Drag coefficient. $M_\infty = 0.655$, $R_c = 4.5 \times 10^6$.

Figure 28. Continued.

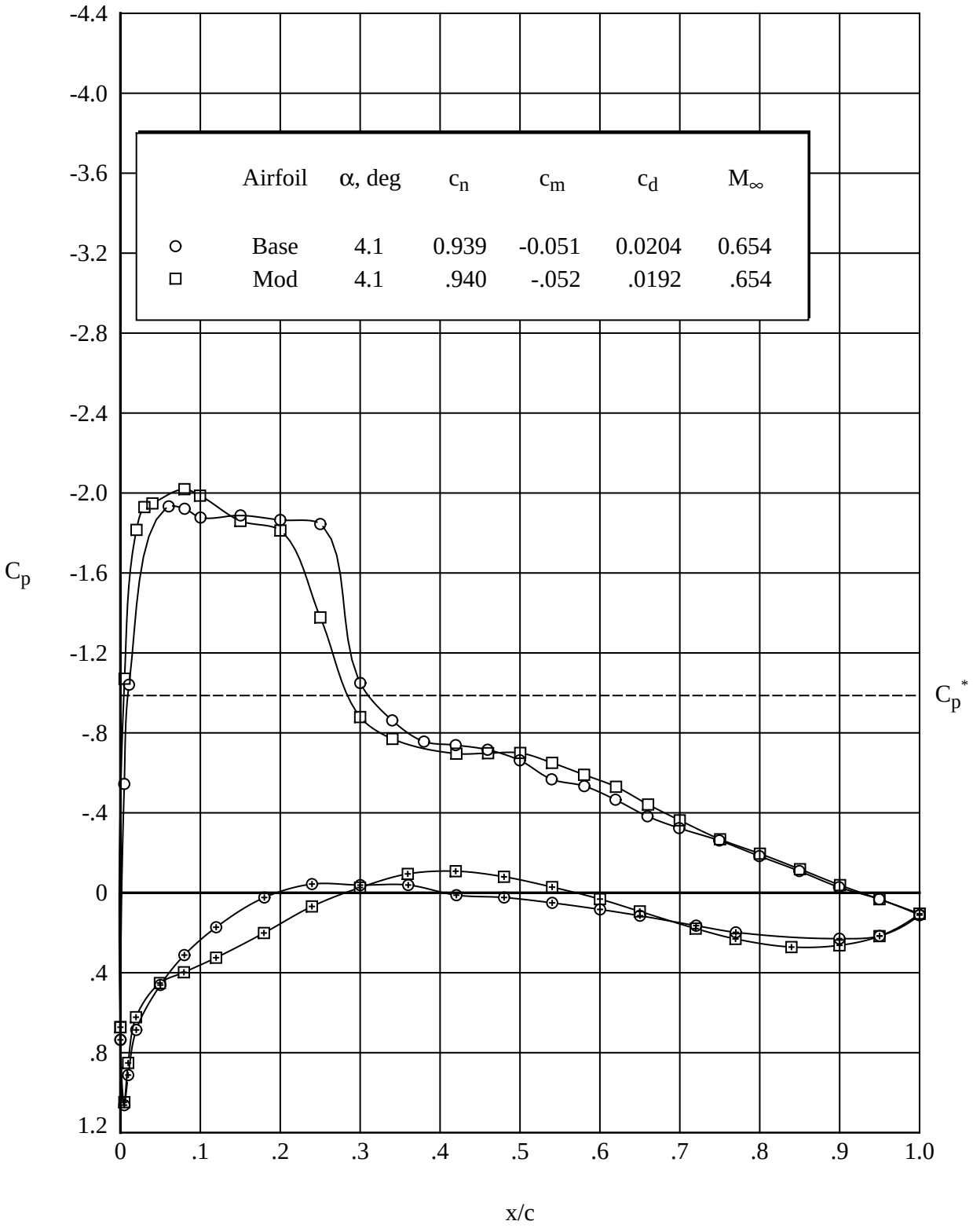

(c) Pressure distributions. Open symbols denote upper surface; "+" within symbol denotes lower surface. $R_c = 4.5 \times 10^6$.

Figure 28. Continued.

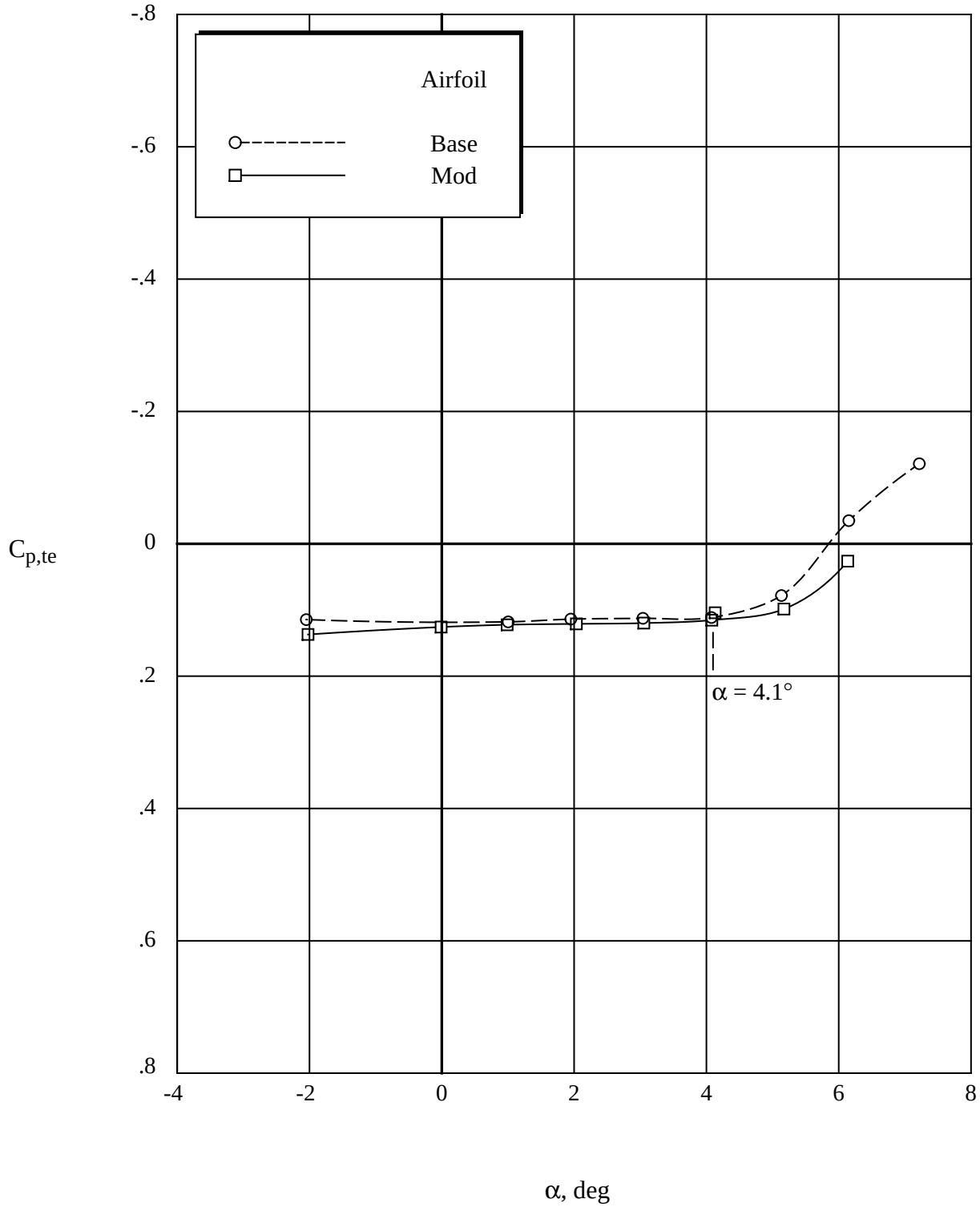

(d) Trailing-edge pressure coefficient. $M_\infty = 0.655$, $R_c = 4.5 \times 10^6$.

Figure 28. Concluded.

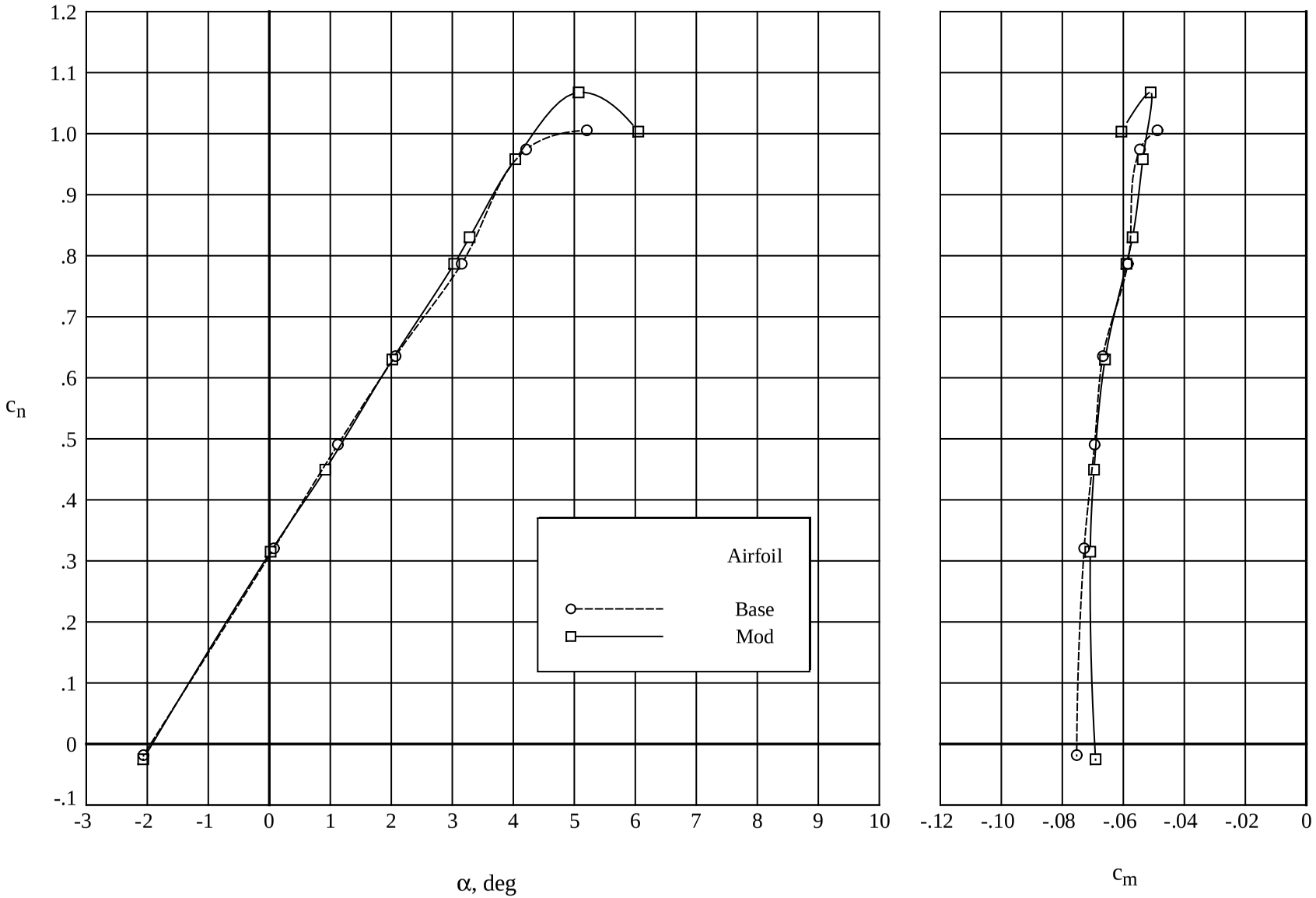

(a) Normal-force and pitching-moment coefficients.

Figure 29. Comparison of characteristics for baseline and modified airfoil. $M_\infty = 0.670$, $R_c = 5.0 \times 10^6$.

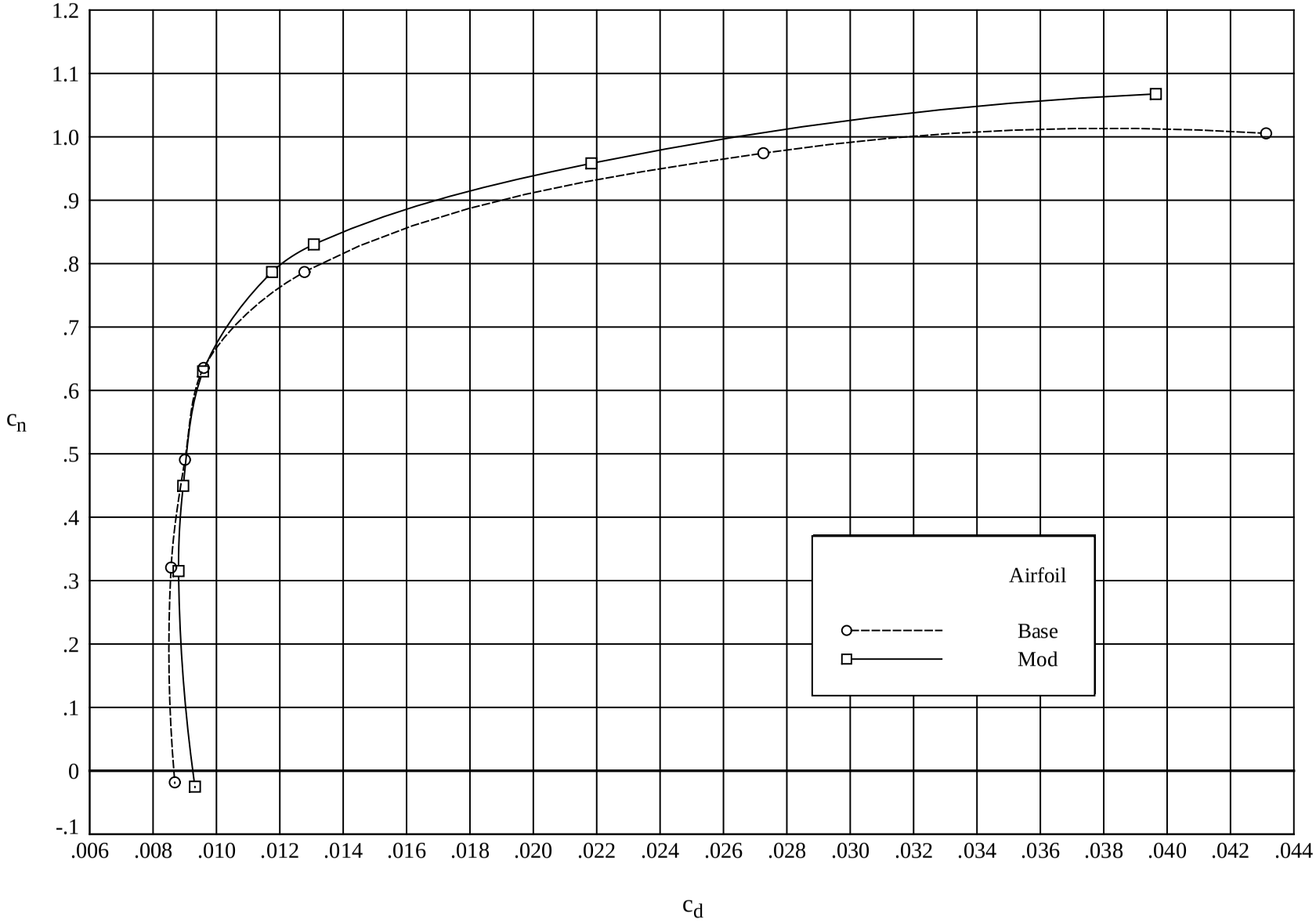

(b) Drag coefficient. $M_\infty = 0.670$, $R_c = 5.0 \times 10^6$.

Figure 29. Continued.

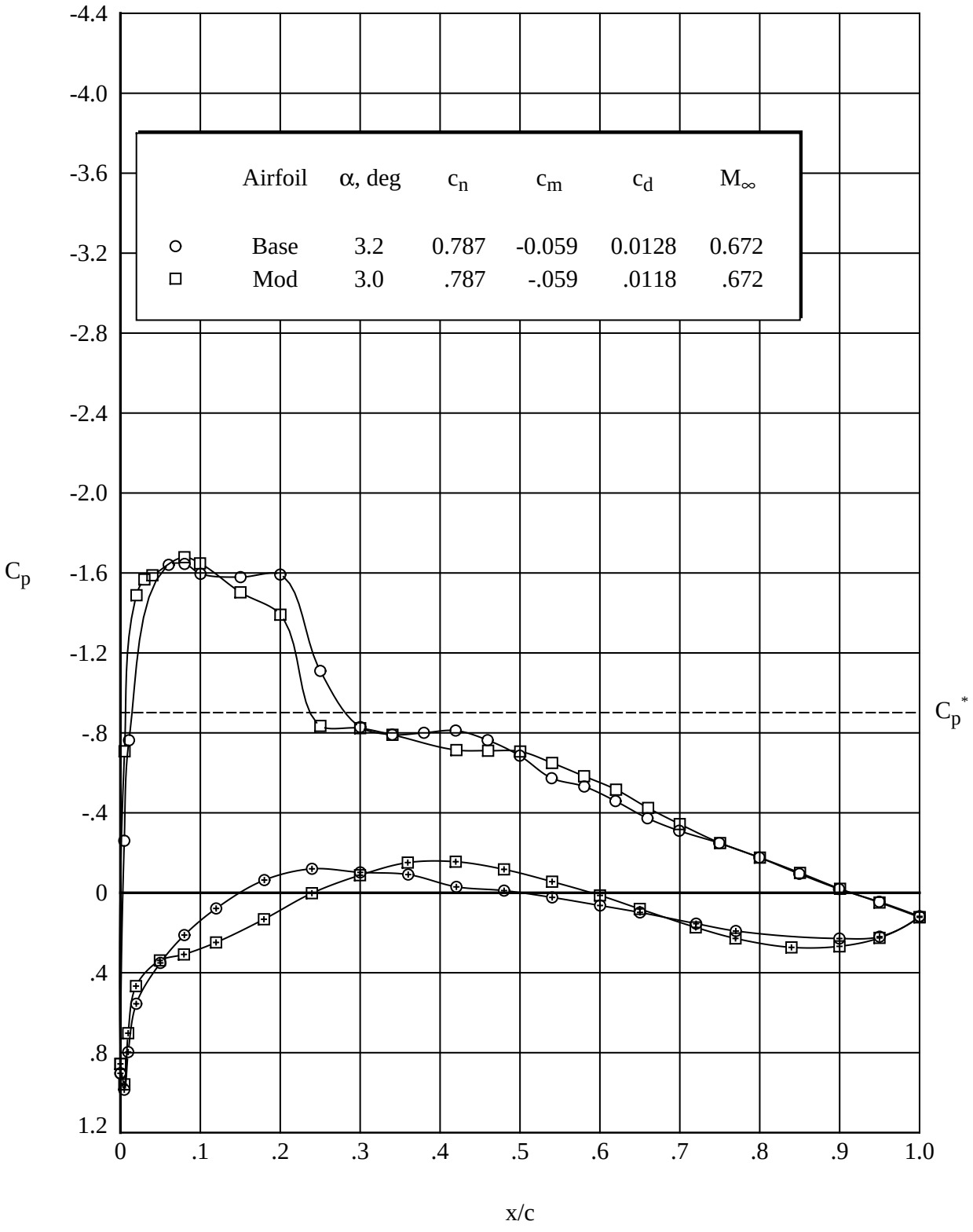

(c) Pressure distributions. Open symbols denote upper surface; "+" within symbol denotes lower surface. $R_c = 5.0 \times 10^6$.

Figure 29. Continued.

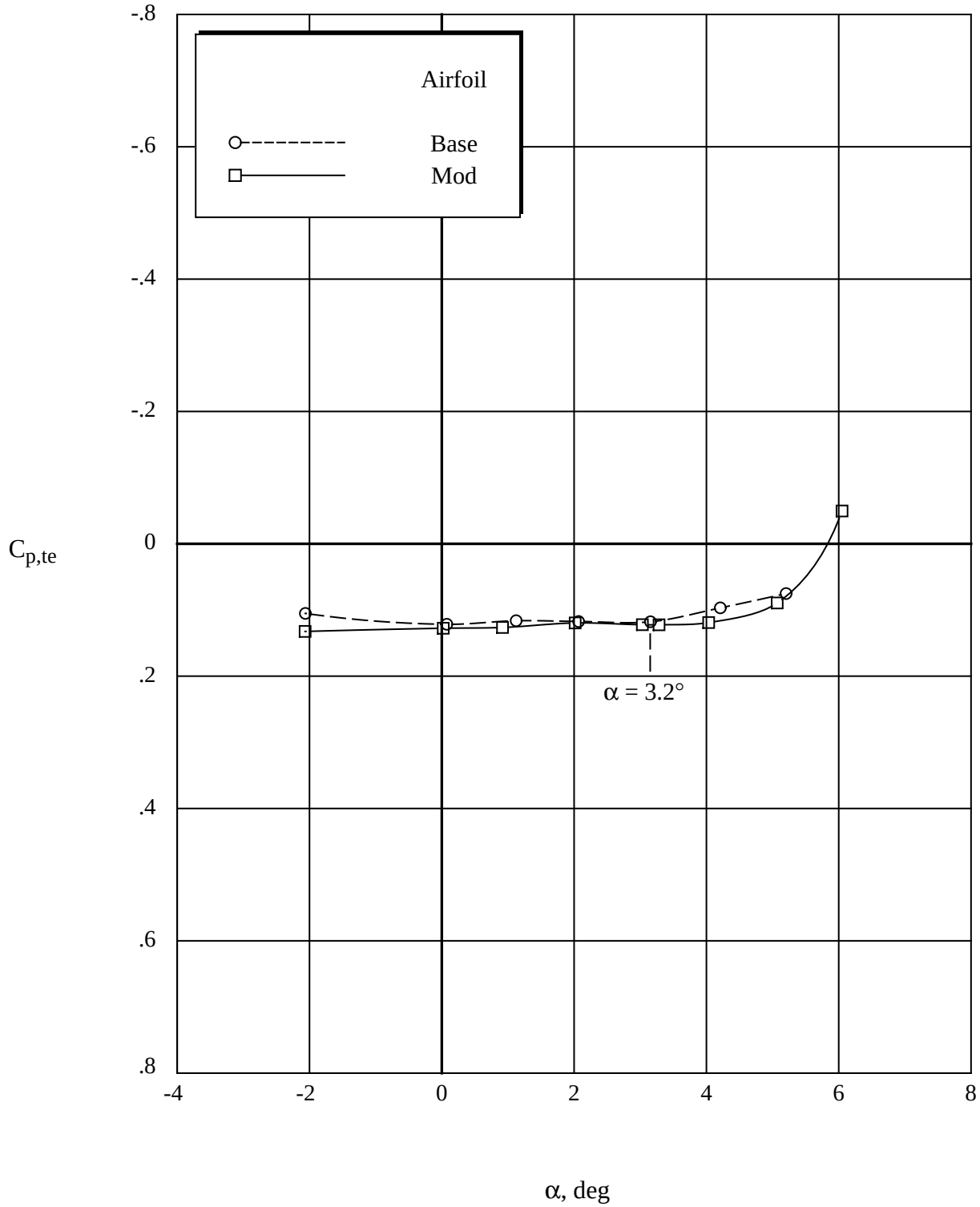

(d) Trailing-edge pressure coefficient. $M_\infty = 0.670$, $R_c = 5.0 \times 10^6$.

Figure 29. Concluded.

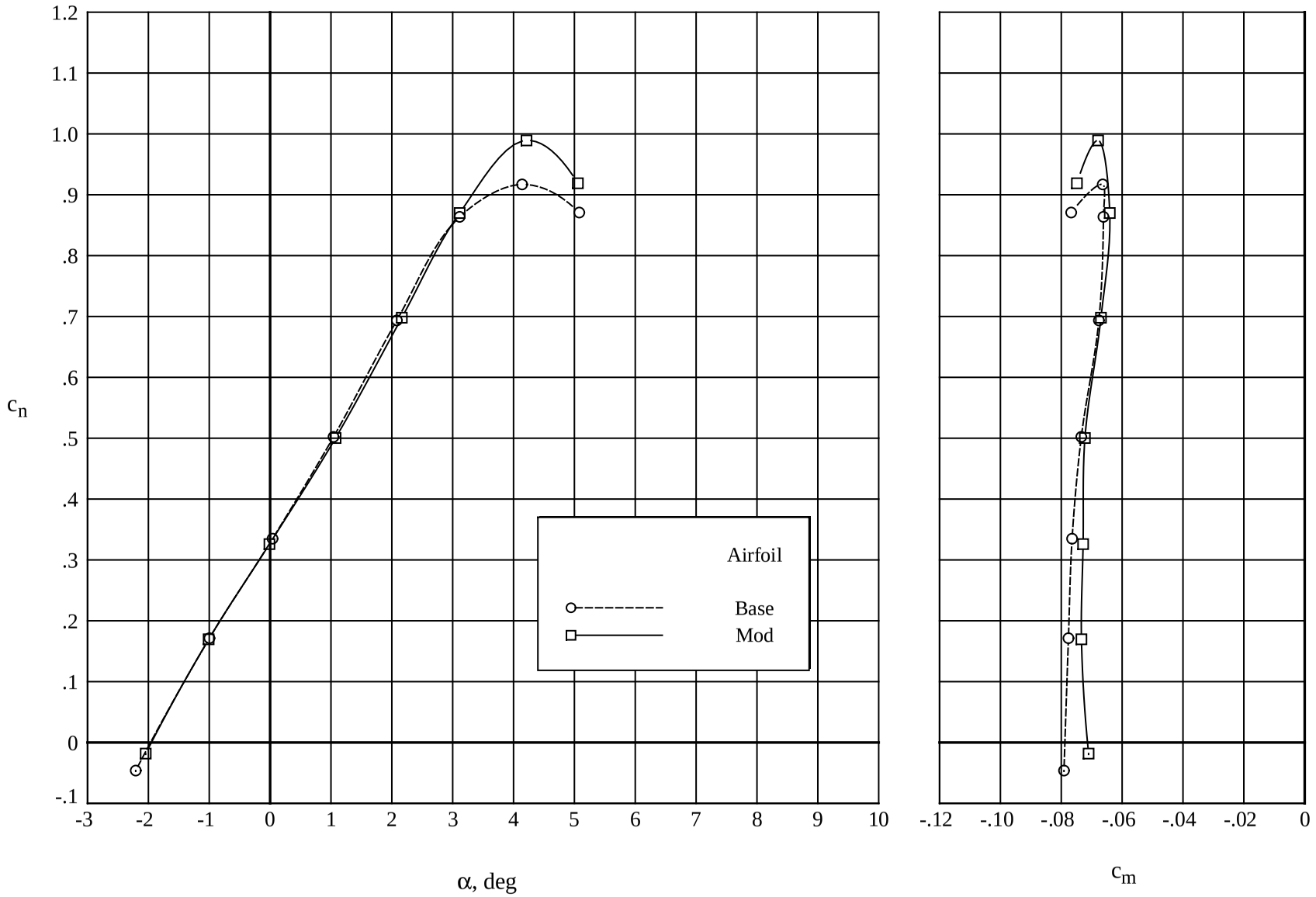

(a) Normal-force and pitching-moment coefficients.

Figure 30. Comparison of characteristics for baseline and modified airfoil. $M_\infty = 0.700$, $R_c = 6.5 \times 10^6$.

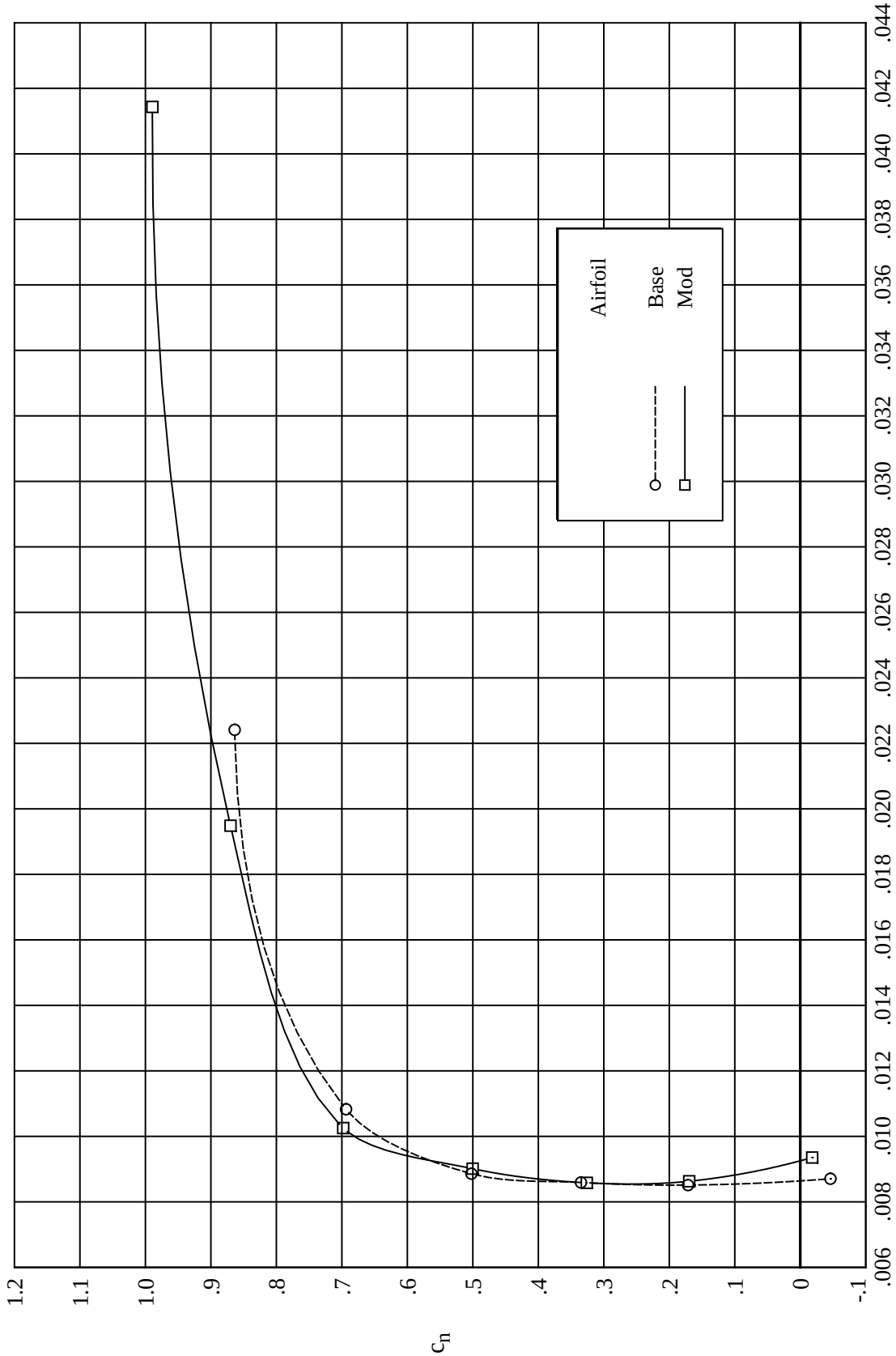

(b) Drag coefficient. $M_\infty = 0.700$, $R_c = 6.5 \times 10^6$.

Figure 30. Continued.

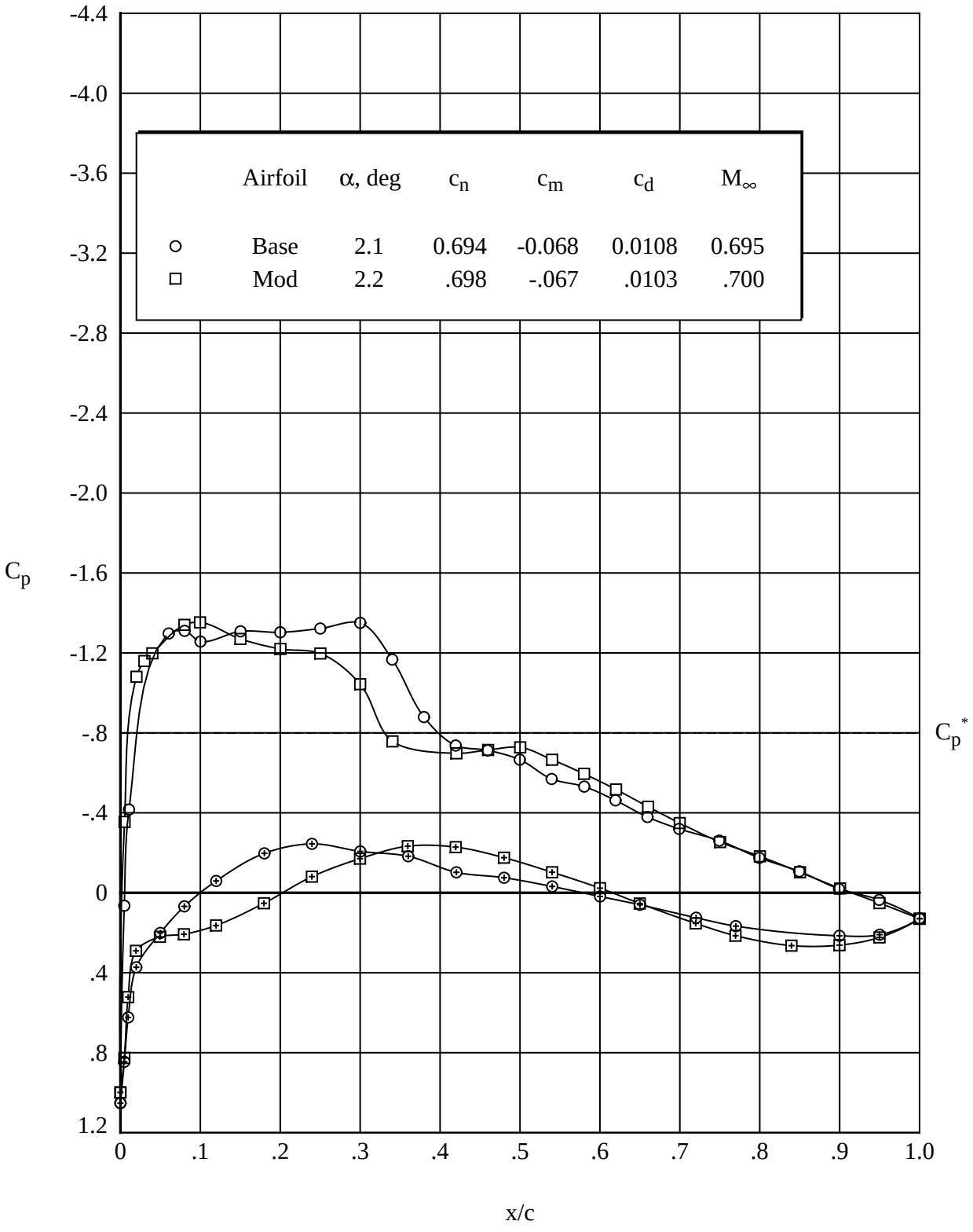

(c) Pressure distributions. Open symbols denote upper surface; "+" within symbol denotes lower surface. $R_c = 6.5 \times 10^6$.

Figure 30. Continued.

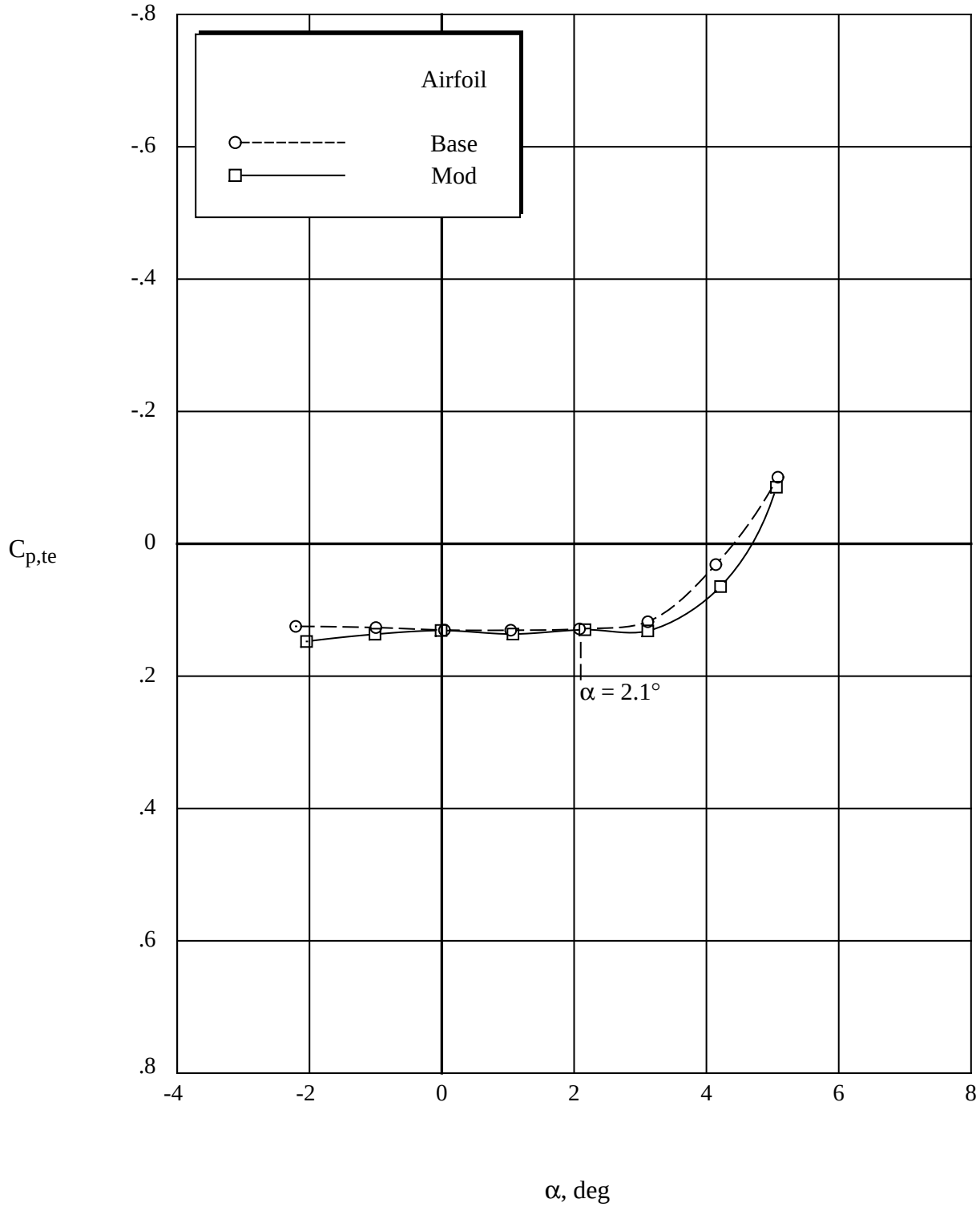

(d) Trailing-edge pressure coefficient. $M_\infty = 0.700$, $R_c = 6.5 \times 10^6$.

Figure 30. Concluded.

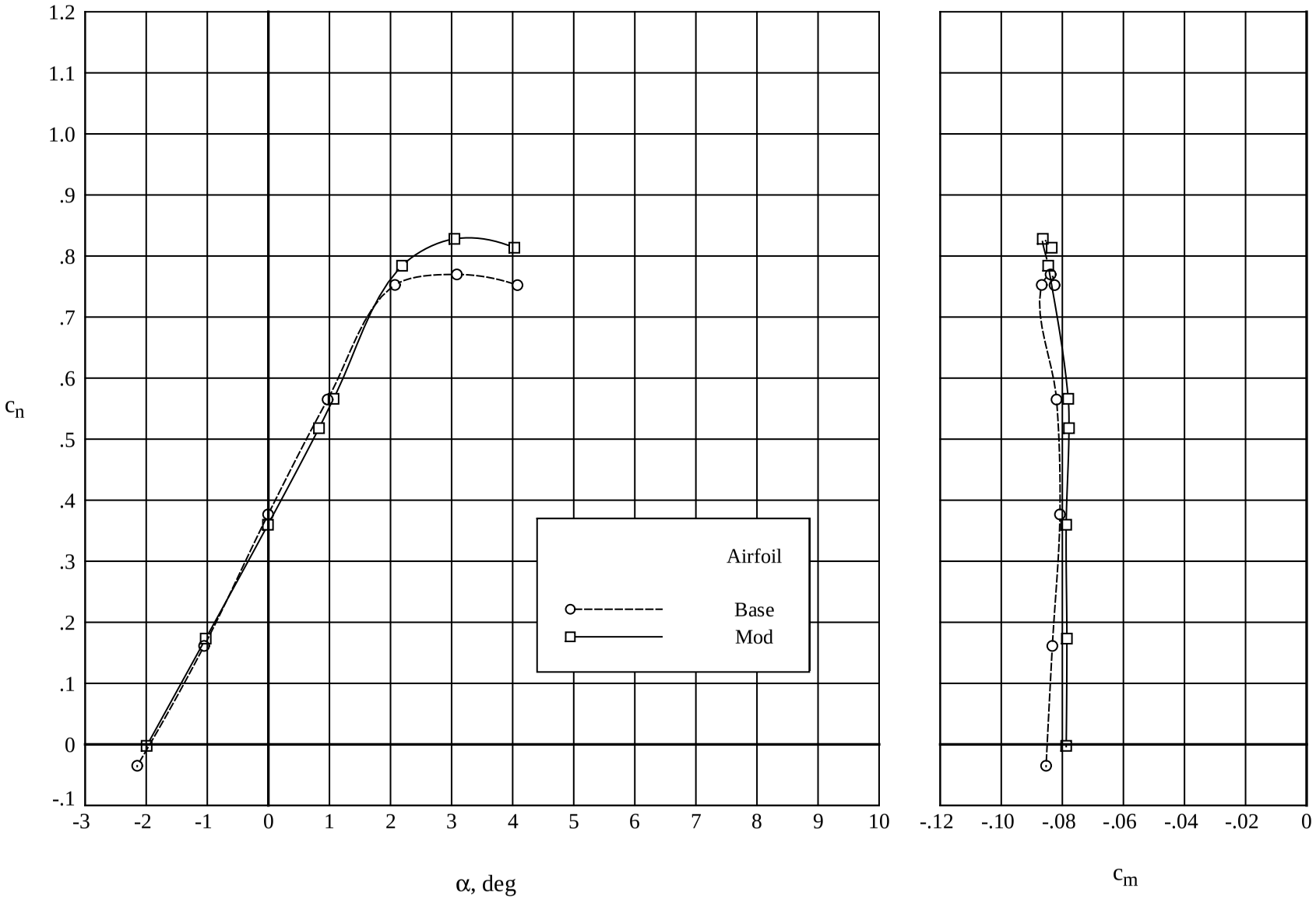

(a) Normal-force and pitching-moment coefficients.

Figure 31. Comparison of characteristics for baseline and modified airfoil. $M_\infty = 0.735$, $R_c = 9.0 \times 10^6$.

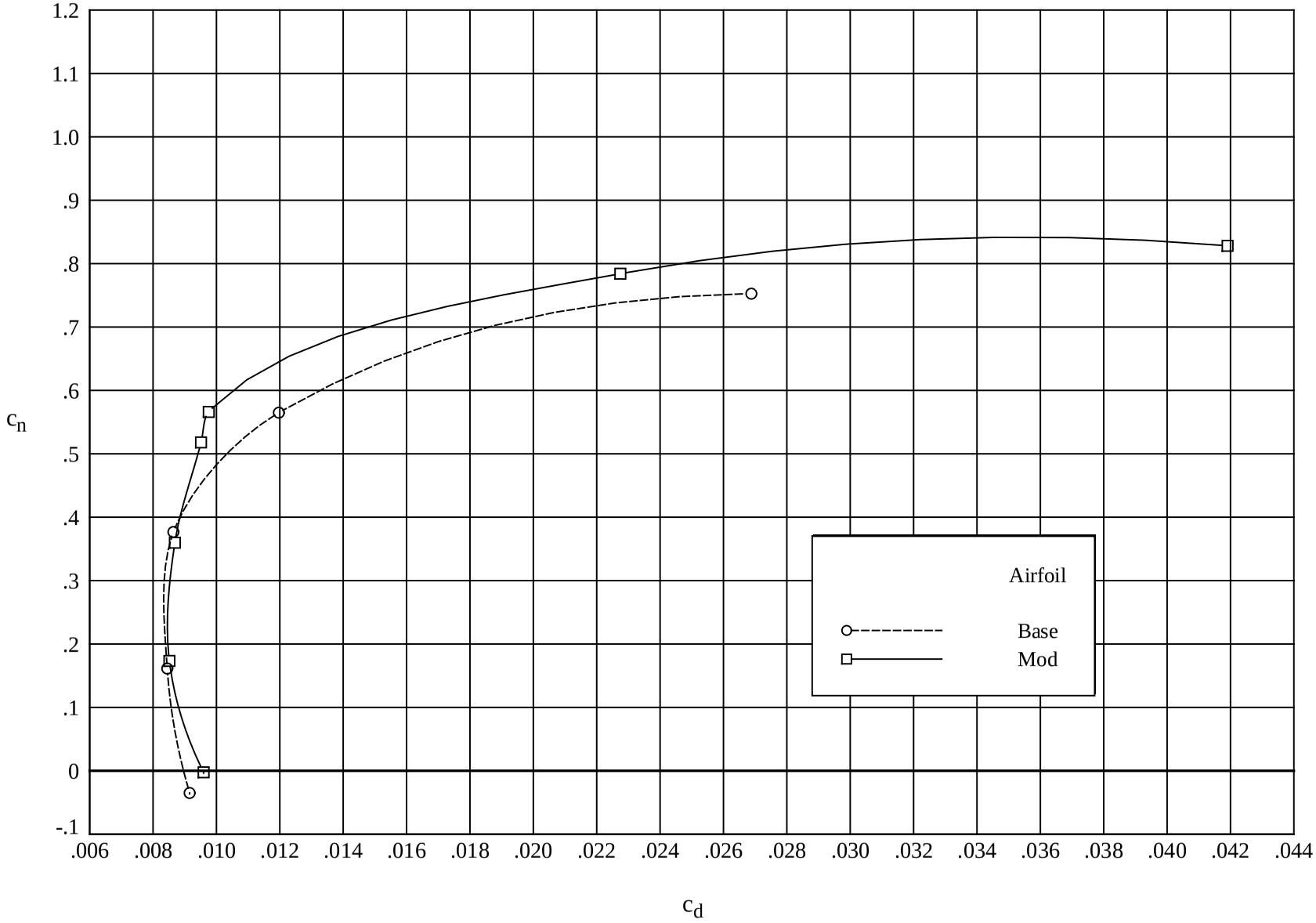

(b) Drag coefficient. $M_\infty = 0.735$, $R_c = 9.0 \times 10^6$.

Figure 31. Continued.

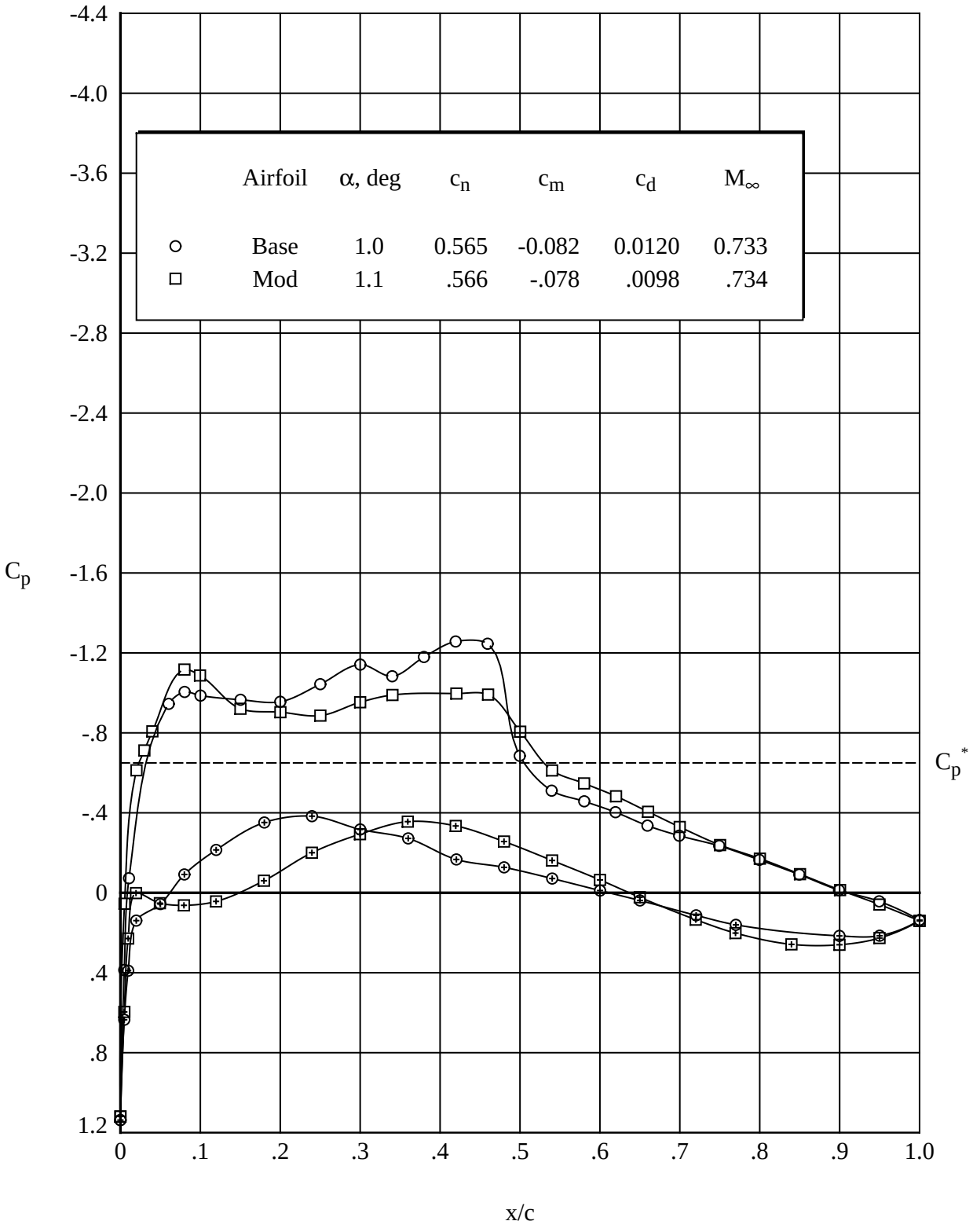

(c) Pressure distributions. Open symbols denote upper surface; "+" within symbol denotes lower surface. $R_c = 9.0 \times 10^6$.

Figure 31. Continued.

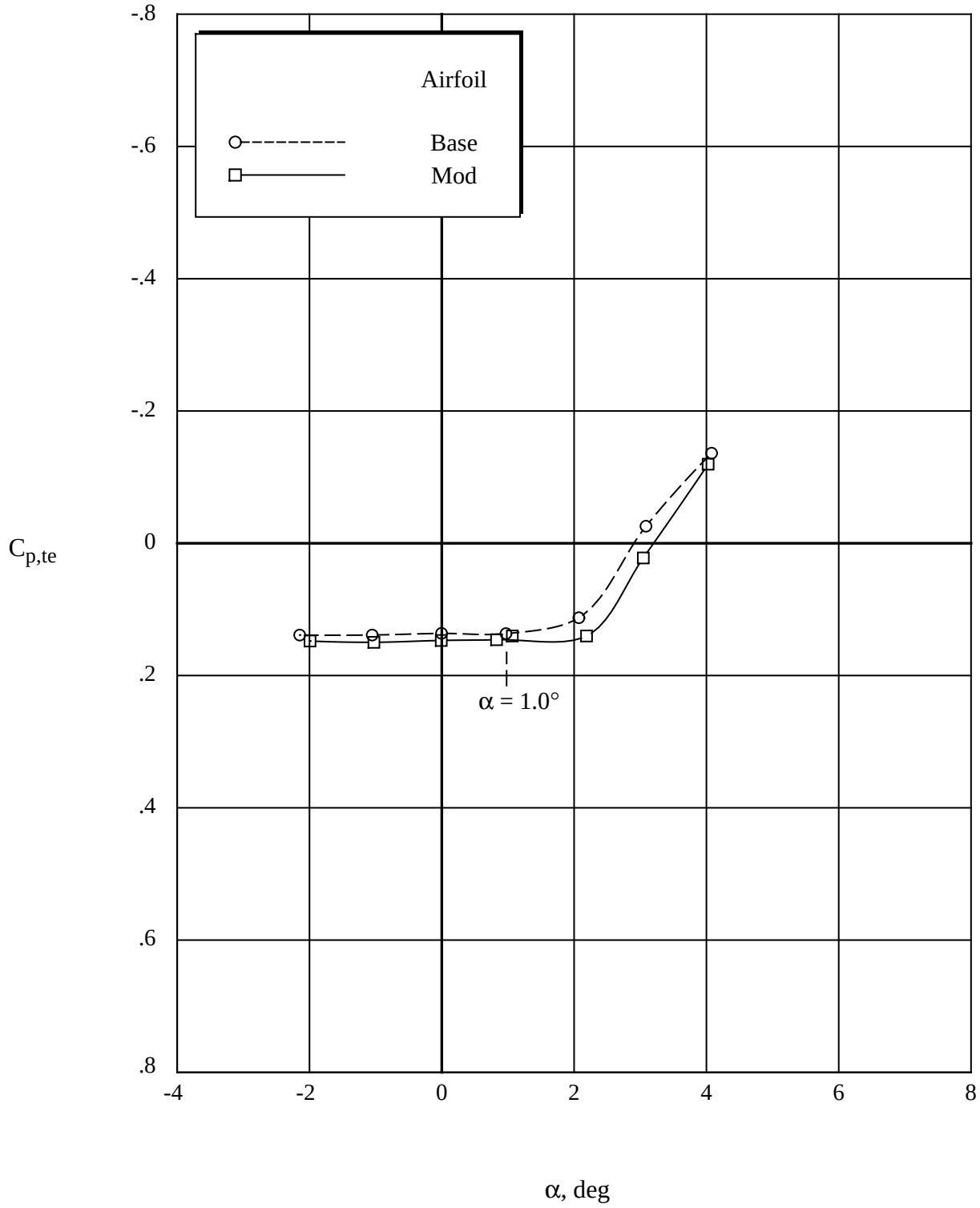

(d) Trailing-edge pressure coefficient. $M_\infty = 0.735$, $R_c = 9.0 \times 10^6$.

Figure 31. Concluded.

REPORT DOCUMENTATION PAGE

Form Approved
OMB No. 0704-0188

1. AGENCY USE ONLY *(Leave blank)*	2. REPORT DATE	3. REPORT TYPE AND DATES COVERED
	July 1996	Technical Paper

4. TITLE AND SUBTITLE
Assessment of Dual-Point Drag Reduction for an Executive-Jet Modified Airfoil Section

5. FUNDING NUMBERS
WU 505-59-10-30

6. AUTHOR(S)
Dennis O. Allison and Raymond E. Mineck

7. PERFORMING ORGANIZATION NAME(S) AND ADDRESS(ES)
NASA Langley Research Center
Hampton, VA 23681-0001

8. PERFORMING ORGANIZATION REPORT NUMBER
L-17500

9. SPONSORING/MONITORING AGENCY NAME(S) AND ADDRESS(ES)
National Aeronautics and Space Administration
Washington, DC 20546-0001

10. SPONSORING/MONITORING AGENCY REPORT NUMBER
NASA TP-3579

11. SUPPLEMENTARY NOTES

12a. DISTRIBUTION/AVAILABILITY STATEMENT
Unclassified–Unlimited
Subject Category 02
Availability: NASA CASI (301) 621-0390

12b. DISTRIBUTION CODE

13. ABSTRACT *(Maximum 200 words)*

This paper presents aerodynamic characteristics and pressure distributions for an executive-jet modified airfoil and discusses drag reduction relative to a baseline airfoil for two cruise design points. A modified airfoil was tested in the adaptive-wall test section of the NASA Langley 0.3-Meter Transonic Cryogenic Tunnel (0.3-m TCT) for Mach numbers from ranging 0.250 to 0.780 and chord Reynolds numbers ranging from 3.0×10^6 to 18.0×10^6. The angle of attack was varied from $-2°$ to almost $10°$. Boundary-layer transition was fixed at 5 percent of chord on both the upper and lower surfaces of the model for most of the test. The two design Mach numbers were 0.654 and 0.735, chord Reynolds numbers were 4.5×10^6 and 8.9×10^6, and normal-force coefficients were 0.98 and 0.51. Test data are presented graphically as integrated force and moment coefficients and chordwise pressure distributions. The maximum normal-force coefficient decreases with increasing Mach number. At a constant normal-force coefficient in the linear region, as Mach number increases an increase occurs in the slope of normal-force coefficient versus angle of attack, negative pitching-moment coefficient, and drag coefficient. With increasing Reynolds number at a constant normal-force coefficient, the pitching-moment coefficient becomes more negative and the drag coefficient decreases. The pressure distributions reveal that when present, separation begins at the trailing edge as angle of attack is increased. The modified airfoil, which is designed with pitching moment and geometric constraints relative to the baseline airfoil, achieved drag reductions for both design points (12 and 22 counts). The drag reductions are associated with stronger suction pressures in the first 10 percent of the upper surface and weakened shock waves.

14. SUBJECT TERMS
Airfoil section; Pressure distributions; Aerodynamic characteristics; Drag reduction; Transonic conditions; Executive jet; Business jet

15. NUMBER OF PAGES
117

16. PRICE CODE
A06

17. SECURITY CLASSIFICATION OF REPORT	18. SECURITY CLASSIFICATION OF THIS PAGE	19. SECURITY CLASSIFICATION OF ABSTRACT	20. LIMITATION OF ABSTRACT
Unclassified	Unclassified	Unclassified	